ALMA MATER STUDIORUM - UNIVERSITÀ DI BOLOGNA

Scuola di Dottorato in Ingegneria Civile ed Architettura

Dottorato in Ingegneria Strutturale ed Idraulica, XXV ciclo

08/A1 – ICAR/01

Model reduction of stochastic groundwater flow and transport processes

Valentina Ciriello

Supervisor:
Prof. Vittorio Di Federico

Coordinator:
Prof. Erasmo Viola

Co-supervisor:
Prof. Alberto Guadagnini

Ph.D. Dissertation, May 2013

Contents

Abstract

This work presents a comprehensive methodology for the reduction of analytical or numerical stochastic models characterized by uncertain input parameters or boundary conditions. The technique, based on the Polynomial Chaos Expansion (PCE) theory, represents a versatile solution to solve direct or inverse problems related to propagation of uncertainty. The potentiality of the methodology is assessed investigating different applicative contexts related to groundwater flow and transport scenarios, such as global sensitivity analysis, risk analysis and model calibration. This is achieved by implementing a numerical code, developed in the MATLAB environment, presented here in its main features and tested with literature examples. The procedure has been conceived under flexibility and efficiency criteria in order to ensure its adaptability to different fields of engineering; it has been applied to different case studies related to flow and transport in porous media. Each application is associated with innovative elements such as (i) new analytical formulations describing motion and displacement of non-Newtonian fluids in porous media, (ii) application of global sensitivity analysis to a high-complexity numerical model inspired by a real case of risk of radionuclide migration in the subsurface environment, and (iii) development of a novel sensitivity-based strategy for parameter calibration and experiment design in laboratory scale tracer transport.

Sommario

In questa tesi viene presentata una metodologia esaustiva per la riduzione di modelli stocastici, di natura analitica o numerica, affetti da incertezza relativamente ai parametri in ingresso o alle condizioni al contorno. Tale metodologia, basata sulla teoria dell'espansione in Caos Polinomiale, costituisce una soluzione versatile per la soluzione di problemi diretti o inversi legati alla propagazione dell'incertezza. Le potenzialità della tecnica sono verificate in questo lavoro investigando differenti contesti applicativi, come l'analisi di sensitività globale, l'analisi di rischio e la calibrazione dei modelli, inerenti a scenari di flusso e trasporto in ambiente sotterraneo. Ciò è realizzato per mezzo di un codice numerico, sviluppato in ambiente MATLAB, presentato in questa tesi nelle sue caratteristiche principali. Tale codice è stato concepito secondo criteri di flessibilità ed efficienza in modo da assicurarne l'adattabilità a differenti campi ingegneristici. Inoltre, ogni caso studio descritto, è associato ad elementi innovativi quali, in particolare, (i) le nuove formulazioni analitiche sviluppate per descrivere flusso e spiazzamento di fluidi non-Newtoniani in mezzi porosi, (ii) l'applicazione della tecnica dell'espansione in Caos Polinomiale ad un modello numerico di elevata complessità ispirato ad un caso reale di rischio di migrazione di radionuclidi nell'ambiente sub-superficiale, e (iii) lo sviluppo di una nuova strategia basata sulla sensitività per l'ottimizzazione della calibrazione dei parametri e per la progettazione degli esperimenti.

1. Introduction

SOMMARIO

In questo capitolo viene introdotto il problema della quantificazione dell'incertezza associata alle modellazioni matematiche di sistemi e processi fisici oggetto di studio. L'ingegneria civile ed ambientale ricorre frequentemente a schematizzazioni complesse per la caratterizzazione degli scenari di interesse al fine di ottenerne una rappresentazione realistica. Ciononostante, un'incertezza dalla duplice natura influenza la capacità di fornire rappresentazioni modellistiche appropriate: da un lato la conoscenza incompleta delle dinamiche dei sistemi reali (*incertezza epistemica*), dall'altro l'aleatorietà intrinseca associata a determinati fenomeni fisici (*incertezza aleatoria*). L'impossibilità di identificare a priori l'impatto di queste fonti di incertezza sulle risposte dei modelli è un punto cruciale di cui occorre tener conto per garantire la robustezza delle previsioni fornite. Conseguentemente, strumenti quali l'Analisi di Sensitività Globale e l'analisi di rischio giocano un ruolo fondamentale per la valutazione (*i*) del modo in cui l'incertezza si propaga, attraverso un modello, dalle fonti in ingresso alla risposta in uscita, (*ii*) delle fonti di incertezza maggiormente influenti rispetto alla variabilità della risposta, (*iii*) della funzione di densità di probabilità associata alla risposta del modello. La quantificazione e caratterizzazione dell'incertezza viene tradizionalmente svolta ricorrendo a metodi di simulazione alquanto onerosi dal punto di vista computazionale. Il metodo più comunemente

utilizzato è il metodo Monte Carlo, dal quale successivamente sono state derivate diverse tecniche di campionamento intelligenti, allo scopo di diminuire il numero di simulazioni necessarie per arrivare a convergenza. Una valida alternativa, capace di ridurre drasticamente il costo computazionale associato alle analisi descritte, è rappresentata dalle tecniche di riduzione dei modelli, che procedono attraverso la sostituzione del modello originale con un modello surrogato caratterizzato da un onere di calcolo trascurabile. Fra le possibili famiglie di modelli surrogati, quella dell'espansione in *Caos Polinomiale* è stata selezionata ed adottata in questo lavoro di ricerca per la sua versatilità e la sua efficienza dimostrate nei confronti di una considerevole molteplicità di casi studio. L'adozione della tecnica dell'espansione in *Caos Polinomiale* a problematiche ingegneristiche è relativamente recente e, di conseguenza, l'estensione dell'applicabilità di questa metodologia rappresenta un campo di ricerca in espansione. In questo capitolo, oltre ad introdurre tale tecnica, sono riassunte le fasi dell'attività di ricerca mirata ad approfondire tematiche ancora parzialmente inesplorate ed a proporre al contempo l'applicabilità degli strumenti sviluppati in differenti contesti.

1.1 UNCERTAINTY QUANTIFICATION IN MODELING

The need for complex numerical models to quantify uncertainty associated with environmental and civil engineering scenarios is strictly connected with the goal of providing a realistic representation of physical systems. Our capability of modelling is typically plagued by uncertainty linked to (*i*) our incomplete knowledge of system dynamics, which ultimately impacts our ability to provide a proper mathematical description (*epistemic uncertainty*), and (*ii*) the randomness which is inherent with natural phenomena (*aleatory uncertainty*) [e.g., *Tartakovsky*, 2007, and references therein]. This limits our ability to understand a priori the impact of these sources of uncertainty on model responses.

Proper identification of the way uncertainties propagate from model input to output is critical to provide effective predictions complying with guidelines provided by regulatory bodies and/or Institutions [US EPA, 2009; European Commission, 2009; *Castaings et al*., 2012].

For these purposes, Global Sensitivity Analysis (GSA) is identified as a suitable method to (*i*) improve the definition of the link between inputs and outputs upon providing quantitative information on the influence of the variability of input parameters on model responses, and (*ii*) address monitoring and data assimilation efforts towards the characterization of the most influential sources of input uncertainty [*Saltelli et al*., 2000; *Tarantola et al*., 2002; *Kiparissides et al*., 2009]. As such, GSA stands as a powerful tool and plays a key role in the attempt to reduce the *epistemic uncertainty* (both structural, i.e., referred to the validity of a mathematical model, and parametric, i.e., associated with model parameters) of a given analytical or numerical model [*Tartakovsky*, 2012].

Relating a probabilistic weight to model predictions has become a

crucial issue in modern environmental and engineering science. Even as epistemic uncertainty can be reduced by augmenting our knowledge, accurate uncertainty quantification (UQ) is required to render robust and functional predictions. In this context, it is also noted that the relevance of a proper quantification of the relationship between environmental phenomena and human health has become an issue which is central to society development [*Maxwell and Kastenberg*, 1999; *Aral*, 2010; *de Barros et al*., 2011; *Tartakovsky*, 2012], as it is strongly related to the assessment of risk for human beings and environmental systems caused by existing or expected hazardous scenarios [*Bedford and Cooke*, 2003].

Though risk analysis (RA) is a relatively recent tool in environmental problems, quite a lot of Institutions and Agencies promote the adoption of this methodology to assess several scenarios [e.g., US NRC, 1997; EC, 2003]. In this context, modelling is considered a key part of an overall process where planning and management are crucial issues involving different subjects (e.g. stakeholders, managers) [*Refsgaard et al*., 2007].

RA is practically developed through the computation of the cumulative distribution function associated with a target state variable to derive the probability of exceeding a threshold value beyond which the risk is not acceptable. A numerical Monte Carlo (MC) analysis is the most common framework adopted for RA because of its flexibility to deal with strongly nonlinear problems [*Vose*, 1996; *Zhang et al*., 2010; *Ballio and Guadagnini*, 2004]. However, the computational demand associated with MC analyses may be a limiting factor in case of complex numerical models and in the presence of a large number of uncertain parameters [*Sudret*, 2008]. As a consequence, it is common practice to compute only the first two (statistical) moments of the state variable of interest [*Zhang and Neuman*, 1996; *Fiori et al*., 2002] or to resort to reduced complexity

schematizations which are capable to encapsulate the major system dynamics involved [*Winter and Tartakovsky*, 2008].

When a refined level of detail is required, probabilistic risk analysis (PRA) may represent an useful comprehensive approach, though the associated computational cost is definitely higher [*Tartakovsky*, 2007; *Bolster et al*., 2009; *Tartakovsky*, 2012].

1.2 METHODOLOGY

Model reduction techniques provide an alternative to overcome the computational limitations in the development of GSA and RA for complex models. Also denoted as meta-modeling strategies, this kind of techniques represents an expanding research field of significant importance in the study of uncertainty related to mathematical formulations adopted to depict complex real systems. The need to reach important information, related to e.g. risk assessment or optimization designs, both in relatively short times and accurately, promotes the adoption of this kind of tools.

These approaches are basically aimed at defining surrogate models which are associated with negligible computational demands due to their simple form. At the same time this strategy avoid the introduction of any simplifying assumption that would change the main features of the original problem [*Sudret*, 2008; *Volkova et al*., 2008; *Ratto et al*., 2012; *Carnevale et al*. 2012; *Villa-Vialaneix et al*., 2012; *Borgonovo et al*., 2012].

Among the possible families of surrogate models, those based on the Polynomial Chaos Expansion (PCE) theory introduced by *Wiener* [1938] have received particular attention in the recent years. The introduction of PCE in engineering applications is due to *Ghanem and Spanos* [1991] within the stochastic finite element (SFE) context. The main idea of this

spectral approach relies on the projection of the model response (i.e., the state variable of interest) onto a probabilistic space (*Polynomial Chaos*) to derive a polynomial approximation which is capable to preserve the entire variability associated with the original formulation. This variability is imbibed into the expansion coefficients [*Ghanem and Spanos*, 1991] so that mean, variance and sensitivity measures can be computed through a simple analytical post-processing once the PCE is defined [*Sudret*, 2008].

Recent examples of the adoption of PCE for GSA and UQ, including comparisons against traditional sampling schemes (e.g., MCs) to verify the accuracy of the method, are presented by, e.g., *Cheng and Sandu* [2009], *Konda et al*. [2010], *Oladyshkin et al*. [2012], *Formaggia et al.* [2012], *Ciriello et al*. [2012], *Ciriello and Di Federico* [2013].

The uncertainty that affects parameters of a selected model is relevant also when optimization or calibration problems are considered. In engineering, inverse problems involve frequently complex systems for which several variables have to be defined contemporary, resulting in challenging and onerous analysis. In this context, the PCE theory represents an useful framework particularly suitable to perform GSA, and can return preliminary important information about the set of parameters that effectively control the system. Only the latter are conveniently included in the subsequent optimization or calibration process. In this sense this approach not only reduces the computational demand associated with onerous analysis, that would not be practically developable on original complex formulations, but also steers the analysis itself towards the key aspects of the problem [*Ciriello et al.*, 2013].

1.3 RESEARCH OUTLINE

A first version of a computational framework based on the PCE theory and constructed in the MATLAB environment is presented. Chapter 2 illustrates the details of the capability and structure of the numerical code together with some test examples to clarify and validate the approach. The key applications developed are then described in the subsequent chapters. These applications comprise problems related to the propagation of variance and GSA as well as parameter calibration, model selection criteria and experiment design. All these applications involve problems of flow and transport in porous materials. The methodologies and tools proposed are widely applicable to different environmental and civil engineering scenarios. The platform of the code has been conceived to be adaptable to different contexts and to be readily modifiable according to specific target case studies. Furthermore, the code has been designed to obtain consistent results in the context of GSA and RA at a reduced computational cost.

Chapter 3 presents an application of the GSA methodology to a novel analytical formulation describing flow and displacement of non-Newtonian fluids in porous media. The adoption of the PCE-based numerical code in this context has been aimed at mapping the influence in space-time of the parameters governing the physical processes involved to provide improved model predictions and support design of experimental campaigns. Comparison against a traditional Monte Carlo approach is also included in the analysis.

Chapter 4 illustrates the application of GSA and RA to scenarios involving complex numerical models. The migration of radionuclides from a radioactive waste repository is considered with reference to a real case study. In this context GSA and RA represent major steps to assess the

hazard related to contamination of water reservoirs and human health. The proposed approach has proved to be highly relevant at this level of modeling complexity allowing a critical reduction of the computational time associated with model runs. Furthermore, the PCE surrogate model, obtained with the implemented numerical code, has returned accurate results when compared against those obtained through the original model.

The last application described in Chapter 5 is related to a different class of problems involving parameter calibration and model selection in the presence of tracer migration in laboratory scale porous media.

2. Model reduction strategy

SOMMARIO

In questo capitolo viene presentata la tecnica di riduzione dei modelli basata sulla teoria dell'espansione in *Caos Polinomiale* introdotta da *Wiener* [1938] e sviluppata in campo ingegneristico da *Ghanem and Spanos* [1991] nel quadro degli elementi finiti stocastici. Tale tecnica vede applicazioni in campo civile ed ambientale relativamente recenti e tuttora rappresenta un campo di ricerca in evoluzione. Il metodo dell'espansione in Caos Polinomiale prevede la proiezione del modello originale in uno spazio di Hilbert generato da un'opportuna base di polinomi scelta in funzione della distribuzione di probabilità associata ai parametri incerti in ingresso. Questa operazione consente di disporre di un modello surrogato in forma polinomiale in grado di ridurre drasticamente i tempi di calcolo necessari per lo svolgimento di analisi complesse quali quelle descritte nel precedente capitolo. Una volta inquadrata la tecnica in modo esaustivo, la versione base di un codice di calcolo sviluppato in ambiente MATLAB, volto alla definizione di un modello surrogato generato secondo questa tecnica, viene presentata in questo capitolo. Il codice è concepito secondo criteri di flessibilità ed efficienza in modo che possa essere facilmente adattabile a diversi casi studio relativi a modelli stocastici di natura analitica o numerica caratterizzati da un insieme di parametri incerti in ingresso modellabili quali variabili random indipendenti. Se i parametri in ingresso mostrano un certo grado di dipendenza o piuttosto sono descritti attraverso processi stocastici, estensioni al codice base che prevedono

rispettivamente l'adozione della trasformata di Nataf e dell'espansione di Karhunen-Loeve, sono inclusi nella trattazione presentata in questo capitolo. Alcuni casi applicativi utili a chiarire i passaggi fondamentali per la definizione dell'espansione in Caos Polinomiale sono inclusi nella parte conclusiva del capitolo. Una di queste applicazioni fa riferimento al contributo "Analisi di sensitività globale ed espansione in Caos Polinomiale: un'applicazione a flussi di filtrazione satura" di V. Ciriello, V. Di Federico, e A. Guadagnini, presentato in occasione del XX Congresso dell'Associazione Italiana di Meccanica Teorica e Applicata (AIMETA, 2011).

2.1 THE POLYNOMIAL CHAOS EXPANSION (PCE) THEORY

2.1.1 Chaos representation of model response

The Polynomial Chaos Expansion (PCE) technique involves the projection of model equation into a probabilistic space, termed Polynomial Chaos, to construct an approximation of the model response surface.

Let $y = f(\mathbf{p},\mathbf{x},t)$ be a selected model that can be described as a relationship between M input parameters, collected in vector $\mathbf{p} = \{p_1, p_2,...,p_M\}$, and the model response, y, evaluated at spatial location $\mathbf{x}$ and time t. If values of input parameters are uncertain they can be modeled as random variables with assigned distributions. This renders the model response random in turn. Here, the latter is assumed to be scalar to exemplify the approach; anyhow this does not affect the generality of the technique. For what concerns the probabilistic representation of model inputs they are treated in the following as independent random variables.

Consider further the model response to be a second-order random variable, i.e. y belonging to the space of random variables with finite variance, $y \in L_2(\Omega,F,P)$, where Ω is the event space equipped with σ-algebra F and probability measure P. The probabilistic space defined above represents an Hilbert space with respect to the inner product $\langle y_1, y_2 \rangle_{L_2} = E[y_1 \cdot y_2]$ that induces the norm $\|y_1\|_{L_2} = \sqrt{E[y_1^2]}$ [*Blatman and Sudret*, 2010]. Under this assumption, y can be approximated through the Polynomial Chaos Expansion (PCE) technique [*Ghanem and Spanos*, 1991] and the approximation converges in the L_2-sense according to *Cameron and Martin* [1947]. The resulting formulation constitutes a meta- (or surrogate) model, $\tilde{y}$, of y. This meta-model is a simple polynomial

function which is expressed in terms of a set of independent random variables, collected in vector $\boldsymbol{\zeta}$, as

$$\tilde{y} = \tilde{f}(\mathbf{x}, t, \boldsymbol{\zeta}(\mathbf{p})) = \sum_{j=0}^{P-1} a_j(\mathbf{x}, t)\Psi_j(\boldsymbol{\zeta}(\mathbf{p})). \tag{2.1}$$

Here, $P = (M+q)!/(M!q!)$ is the number of terms employed in the polynomial representation of y, and q is the maximum degree considered in the expansion; a_j represent the unknown deterministic coefficients of the expansion while Ψ_j denote the suitable multivariate polynomial basis in the Hilbert space containing the response (i.e. the basis that generates the probabilistic space). In the following the dependence of a_j from spatial location **x** and time t will be omitted for the sake of brevity.

Wiener [1938] first introduced the PCE by adopting *Hermite Polynomials* as a basis for the approximation of Gaussian processes. Different types of orthogonal polynomials are required for optimum convergence rate in the case of non-Gaussian processes (Table 2.1), as the probability distribution of input parameters influences the choice of the polynomial basis in (2.1). In this regard, *Xiu and Karniadakis* [2002] introduced the Askey family of hypergeometric polynomials (*generalized* PCE), to extend the approach to other possible distributions.

Once the appropriate kind of polynomials is identified, the set of independent random variables $\boldsymbol{\zeta}$ automatically stems from orthogonality condition, as the multivariate polynomial basis has to be orthonormal with respect to the joint PDF of $\boldsymbol{\zeta}$. The variables collected in $\boldsymbol{\zeta}$ are then related to the input parameters in $\mathbf{p}$ via a simple isoprobabilistic transform [*Sudret*, 2008].

Distribution of random inputs		**Polynomial basis**	**Support**
Continuous	Gaussian	Hermite polynomials	$(-\infty,\infty)$
	Gamma	Laguerre polynomials	$[0,\infty)$
	Beta	Jacobi polynomials	$[a,b]$
	Uniform	Legendre polynomials	$[a,b]$
Discrete	Poisson	Charlier polynomials	$\{0,1,2...\}$
	Binomial	Krawtchouk	$\{0,1,...,N\}$
	Negative binomial	Meixner polynomials	$\{0,1,2...\}$
	Hypergeometric	Hahn polynomials	$\{0,1,...,N\}$

Table 2.1. Distributions of random input and respective polynomial basis in the Wiener-Askey scheme.

2.1.2 Computation of the expansion coefficients

The traditional approach for the computation of the expansion coefficients in stochastic finite element analysis consists in the minimization, in the Galerkin sense, of the residual present in the balance equation [*Sudret*, 2008; *Ghanem and Spanos*, 1991]. This solving method is identified as intrusive, requiring onerous and specific implementation in the finite element code [*Sudret*, 2008; *Webster et al*., 1996].

A non-intrusive regression-based approach, comparable with the response surface method widely used in science and engineering, can be employed to calculate the coefficients a_j appearing in (2.1) upon minimization of the variance of a suitable residual, ε, typically defined as the difference between the surrogate model response, $\tilde{y}$, and the solution given by the original model, y, with respect to the vector of the unknown coefficients $\mathbf{a}$ [*Sudret*, 2008]:

$$ArgMin\left\{E\left[\varepsilon^2\right],\mathbf{a}\right\}=ArgMin\left\{E\left[\left(f(\mathbf{p})-\tilde{f}(\zeta(\mathbf{p}))\right)^2\right],\mathbf{a}\right\}, \tag{2.2}$$

with E[·] denoting expected value.

The optimum set of regression points in the (random) parameter space is determined on the basis of the same arguments adopted for integral estimation through Gaussian quadrature; the method employs the roots of the polynomial of one order higher than *q*, to assure proper sampling of the region associated with largest probability in the distributions of the input parameters (Figure 2.1). The latter approach is denominated the probabilistic collocation method [*Huang et al*., 2007; *Webster et al*., 1996].

The vector $\mathbf{a}$ that optimizes the regression expressed in (2.2) can be determined in form of matrix calculation as

$$\mathbf{a}=\left(\mathbf{\Psi}^T\mathbf{\Psi}\right)^{-1}\mathbf{\Psi}^T\mathbf{y}', \tag{2.3}$$

where:

$$\mathbf{\Psi}_{ij}=\Psi_j\left(\zeta^i\right), \quad i=1,...N; j=0,...P-1. \tag{2.4}$$

Here N is the number of regression points, $\mathbf{y}'$ is the vector denoting the model response at these points, while the product $\mathbf{\Psi}^T\mathbf{\Psi}$ defines the so-called information matrix. Solving (2.3) requires a minimum of $N=P$ regression points. One typically selects $N>P$ to avoid singularity in the information matrix. Figure 2.2 depicts P, that is proportional to the dimension of the problem, against the number of random input parameters, *M*, for different degrees of the expansion, $\mathbf{q}$. It is possible to observe that even in case of complex models with several parameters, the number of model runs required to compute the PCE surrogate model remains definitely lower with respect to the number of simulations typically

required by Monte Carlo (MC) analysis.

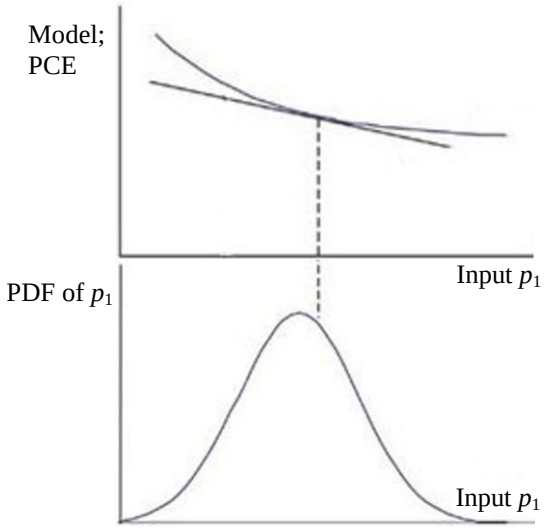

Figure 2.1. Example of sampling in the probability distributions of an input parameter to constitute the set of regression points.

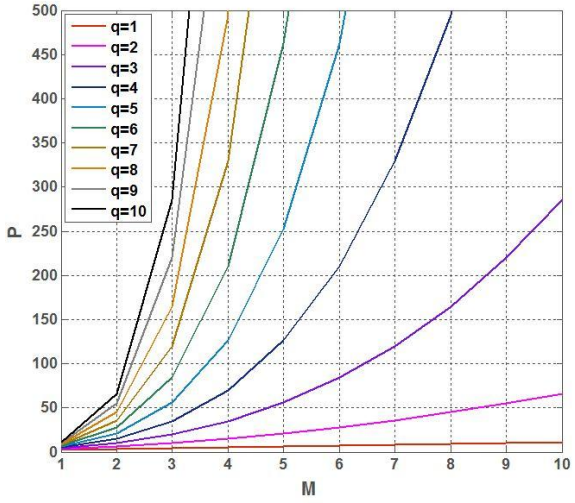

Figure 2.2. Number of unknown expansion coefficients, *P*, against *M* for different values of **q**.

2.1.3 The Nataf transform

Correlation amongst random parameters can be included in the methodology by applying the Nataf transform [*Nataf*, 1962].

Let $\mathbf{p} = \{p_1, p_2, ..., p_M\}$ be the vector of correlated random input parameters. When the marginal CDFs, $F_{\mathrm{p}_i}(p_i)$, $i = 1, ..., M$, and the correlation matrix, $\boldsymbol{\rho} = (\rho_{ij})_{M \times M}$, are known, an isoprobabilistic transform can be applied to transform $\mathbf{p}$ in a vector $\mathbf{z} = \{z_1, z_2, ..., z_M\}$ of standardized normal random variables:

$$\mathrm{z}_i = \Phi^{-1}\left(F_{\mathrm{p}_i}(p_i)\right), \quad i = 1, ..., M, \tag{2.5}$$

where $\Phi^{-1}(\,)$ is the inverse standard normal CDF.

The joint probability density function related to the variables collected in $\mathbf{z}$ is given by:

$$\phi_M(\mathbf{z}, \boldsymbol{\rho}_0) = \frac{1}{\sqrt{(2\pi)^M \det(\boldsymbol{\rho}_0)}} \exp\left(-\frac{1}{2}\mathbf{z}^{\mathrm{T}} \boldsymbol{\rho}_0^{-1} \mathbf{z}\right), \tag{2.6}$$

where $\boldsymbol{\rho}_0 = (\rho_{0ij})_{M \times M}$ represents the respective correlation matrix.

According to the Nataf transform theory, the approximate joint PDF $f_{\mathbf{p}}(\,)$ may be expressed as

$$f_{\mathbf{p}}(\mathbf{p}) = \frac{f_{\mathrm{p}_1}(p_1) \cdot f_{\mathrm{p}_2}(p_2) \cdot ... \cdot f_{\mathrm{p}_M}(p_M)}{\phi(z_1) \cdot \phi(z_2) \cdot ... \cdot \phi(z_M)} \phi_M(\mathbf{z}, \boldsymbol{\rho}_0). \tag{2.7}$$

To determine the correlation matrix $\boldsymbol{\rho}_0 = (\rho_{0ij})_{M \times M}$ in the previous equation, any two random variables (p_i, p_j) are considered and the linear

correlation between them results:

$$\rho_{ij} = \int_{-\infty}^{\infty}\int_{-\infty}^{\infty}\left(\frac{F_i^{-1}\left[\Phi\left(z_i\right)\right]-\mu_{p_i}}{\sigma_{p_i}}\right)\cdot\left(\frac{F_j^{-1}\left[\Phi\left(z_j\right)\right]-\mu_{p_j}}{\sigma_{p_j}}\right)\cdot\phi_2\left(z_i,z_j,\rho_{0ij}\right)\cdot dz_i dz_j \quad (2.8)$$

where μ_{p_i}, μ_{p_j}, σ_{p_i}, σ_{p_j} are the means and standard deviations of p_i and p_j respectively.

Once $\boldsymbol{\rho}_0$ is obtained, it can be decomposed following Cholesky as

$$\boldsymbol{\rho}_0 = \boldsymbol{\Gamma}_0 \cdot \boldsymbol{\Gamma}_0^T, \quad (2.9)$$

where $\boldsymbol{\Gamma}_0$ is the lower triangular matrix.

Finally the independent and dependent standard normal random vectors, $\boldsymbol{\zeta}$ and $\mathbf{z}$ respectively, are related as follows

$$\mathbf{z} = \boldsymbol{\Gamma}_0 \cdot \boldsymbol{\zeta}. \quad (2.10)$$

With the adoption of the Nataf transform the problem of correlation among input parameters is reduced to the set of assumptions required for the application of the PCE [see e.g. *Li et al*., 2011].

2.1.3 The Karhunen-Loeve Expansion (KLE)

The representation of random fields can be included in this framework based on the PCE theory through the adoption of the Karhunen-Loeve Expansion (KLE) [*Ghanem and Spanos*, 1991]. The latter characterizes stationary and non-stationary random process in terms of uncorrelated random variables $\zeta_k(\theta)$:

$$\omega(x,\theta) = \overline{\omega}(x) + \sum_{k=1}^{M}\sqrt{\lambda_k}\,\zeta_k(\theta)\,f_k(x), \quad (2.11)$$

$\overline{\omega}(x)$ being the mean of the process, λ_k and $f_k(x)$ the eigenvalues and eigenfunctions of the covariance function $C(x_1, x_2)$ respectively; *M* is the number of terms of the expansion.

The deterministic eigenfunctions and the eigenvalues derive from the solution of the homogeneous Fredholm integral equation of the second kind:

$$\int_D C(x_1, x_2) f_k(x_1) dx_1 = \lambda_k f_k(x_2). \tag{2.12}$$

For most of the covariance functions, numerical method are required to solve equation (2.12). In this context, the adoption of a traditional Galerkin approach results in dense matrices onerous to be computed and inverted. A more efficient method is adopted in this work, based on a Wavelet-Galerkin scheme proposed in *Phoon et al*. [2002]. According to this approach from the Haar mother wavelet function, $\psi(x)$, (Figure 2.3) a complete set of orthogonal functions is defined over the domain [0,1] in two steps:

$$\psi_{j,k}(x) = a_j \cdot \psi\left(2^j x - k\right), \tag{2.13}$$

$$\psi_0(x) = 1,\ \psi_i(x) = \psi_{j,k}(x),\ i = 2^j + k \quad . \tag{2.14}$$

Here, a_j represents the amplitude of the function (set to 1), $j = 0,1,...,m-1$ the dilatation constant and $k = 0,1,...,2^j - 1$ the translational constant respectively; m is the maximum wavelet level.

The orthogonality condition can be written as

$$\int_0^1 \psi_i(x) \cdot \psi_j(x) \cdot dx = h_j \cdot \delta_{ij}\,, \tag{2.15}$$

where h_i is a constant and δ_{ij} represents the Kronecker-delta function.

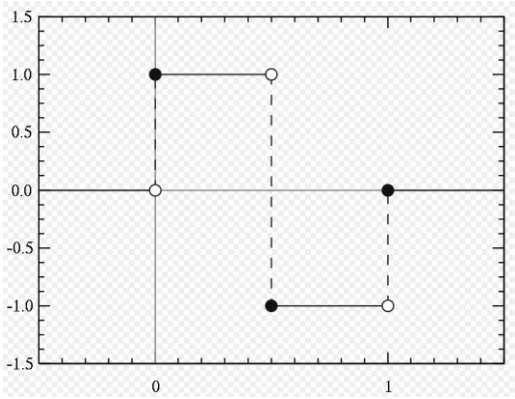

Figure 2.3. Number of unknown expansion coefficients, *P*, against *M* for different values of **q**.

In this framework the eigenfunction $f_k(x)$ can be properly approximated as a truncated series of Haar wavelets:

$$f_k(x) = \sum_{i=0}^{N-1} d_i^{(k)} \cdot \psi_i(x) = \Psi^T(x) \cdot D^{(k)}, \tag{2.16}$$

where $d_i^{(k)}$ are the wavelet coefficients and $N = 2^m$ [*Phoon et al*., 2002].

The expression of the covariance function can be obtained through the application of the 2D wavelet transform as follows:

$$C(x_1, x_2) = \Psi^T(x_1) \cdot A \cdot \Psi(x_2), \tag{2.17}$$

$$A_{ji} = \frac{1}{h_i h_j} \int_0^1 \int_0^1 C(x_1, x_2) \cdot \psi_i(x_2) \cdot \psi_j(x_1) \cdot dx_1 \cdot dx_2 . \tag{2.18}$$

The original problem expressed by equation (2.12) is reduced to the following eigenvalue problem:

$$\Psi^T(x)\cdot A\cdot H\cdot D^{(k)} = \lambda_k \cdot \Psi^T(x)\cdot D^{(k)}, \tag{2.19}$$

where H is a diagonal matrix constituted by the elements h_i defined in (2.15) [*Phoon et al*., 2002].

2.2 GLOBAL SENSITIVITY ANALYSIS (GSA)

2.2.1 The ANOVA decomposition and Sobol indices

Consider the model function $y = f(\mathbf{p})$, representing the relationship between the random output *y* and the vector $\mathbf{p}$ of *M* independent random model parameters. Suppose that the latter are defined in the *M*-dimensional unit hypercube, I^M. If $f(\mathbf{p})$ is integrable, the following representation holds:

$$f(\mathbf{p}) = f_0 + \sum_{i=1}^{M} f_i(p_i) + \sum_{1\le i<j\le M} f_{ij}(p_i, p_j) + \ldots + f_{1,2,\ldots M}(p_1, p_2, \ldots, p_M) \tag{2.20}$$

where $f_0 = \int_{I^M} f(\mathbf{p})d\mathbf{p}$ is the mean of the model output and, e.g., $f_i(p_i) = \int_{I^{M-1}} f(\mathbf{p})d\mathbf{p}_{\sim i} - f_0$, is the function obtained by integrating over all parameters except p_i.

Assuming the validity of the following condition:

$$\int_{I^s} f_{i_1,\ldots i_s}(p_{i_1},\ldots p_{i_s}) \prod_{k=i_1}^{i_s} dp_k = 0, \quad 1\le i_1 <\ldots< i_s \le M, s = 1,\ldots M \tag{2.21}$$

where indices $i_1,\ldots,i_s$, define the set $\{p_{i_1},\ldots,p_{i_s}\}$ of random model parameters, the 2^M summands in (2.20) are orthogonal functions and

condition (2.21) renders representation (2.20), which is typically termed ANOVA decomposition [*Archer et al*. 1997], unique.

The total variance, V, of the model due to the uncertainty of the M parameters is:

$$V = \int_{I^M} f^2(\mathbf{p}) d\mathbf{p} - f_0^2 = \sum_{1 \le i_1 < \ldots < i_s \le M} V_{i_1,\ldots i_s} , \tag{2.22}$$

where $V_{i_1,\ldots i_s} = \int_{I^s} f^2_{i_1,\ldots i_s}\left(p_{i_1},\ldots,p_{i_s}\right)\prod_{k=i_1}^{i_s} dp_k$ is the partial variance, expressing the contribution due to the interaction of parameters $\left\{p_{i_1},\ldots,p_{i_s}\right\}$. The generic *s*-order Sobol index $S_{i_1,\ldots i_s}$ is defined as [*Sobol*, 1993]:

$$S_{i_1,\ldots i_s} = V_{i_1,\ldots i_s} / V \tag{2.23}$$

The sum of these indices over all possible combinations of parameters is unity. The first-order or principal sensitivity index, S_i, describes the significance of the parameter p_i considered individually, in terms of the fraction of total output variance which is attributed to the variability of p_i by itself. Higher-order indices $S_{i_1,\ldots i_s}$ account for the variance attributable to the simultaneous variability of a group of parameters. The overall contribution of the variability of a given parameter p_i to the output variance is described by the total sensitivity index S_{T_i}:

$$S_{T_i} = \sum_{\eta_i} S_{i_1,\ldots i_s} , \quad \eta_i = \left\{\left(i_1,\ldots i_s\right) : \exists k, 1 \le k \le s, i_k = i\right\}. \tag{2.24}$$

The evaluation of the indices (2.23) requires multiple integrations of the model $f(\cdot)$ and its square, for various combinations of the parameters. This is traditionally achieved by MC simulation [*Sobol*, 2001] and the

associated computational cost can soon become prohibitive when the model is complex and/or the number of parameters is large [*Sudret*, 2008].

2.2.2 PCE and GSA

The entire variability of the original model is conserved in the set of expansion coefficients [*Ghanem and Spanos*, 1991], rendering PCE a powerful tool for GSA as the Sobol indices can be calculated analytically from these coefficients without additional computational cost [*Sudret*, 2008]. Manipulating $\tilde{y}$ by appropriate grouping of terms allows isolating the contributions of the different (random) parameters to the system response as:

$$\tilde{y}(\boldsymbol{\zeta}) = a_0 + \sum_{i=1}^{M} \sum_{\alpha \in \varphi_i} a_\alpha \Psi_\alpha(\zeta_i) + \sum_{1 \le i_1 < \ldots < i_s \le M}^{M} \sum_{\alpha \in \varphi_{i_1 \ldots i_s}} a_\alpha \Psi_\alpha(\zeta_{i_1}, \ldots, \zeta_{i_s}) + \ldots + \sum_{\alpha \in \varphi_{1,2,\ldots M}} a_\alpha \Psi_\alpha(\zeta_1, \ldots, \zeta_M) \tag{2.25}$$

φ denoting a general term depending only on the variables specified by the subscript.

The mean of the model response coincides with the coefficient of the zero-order term, a_0, in (2.25), while the total variance of the response and the generic Sobol index, calculated through the PCE, respectively result:

$$V^{(\tilde{y})} = Var\left[\sum_{j=0}^{P-1} a_j \Psi_j(\boldsymbol{\zeta})\right] = \sum_{j=1}^{P-1} a_j^2 E\left[\Psi_j^2(\boldsymbol{\zeta})\right], \tag{2.26}$$

$$S_{i_1,..i_s}^{(\tilde{y})} S = \frac{\sum a_\alpha^2 E\left[\Psi_\alpha^2\right]}{V^{(\tilde{y})}}. \tag{2.27}$$

Calculation of $E\left[\Psi_\alpha^2\right]$ can be performed following, e.g., *Abramowitz and Stegun* [1970].

2.3 THE MATLAB TOOLBOX

This chapter is devoted to the presentation of the developed MATLAB computational framework based on the PCE theory. The numerical tool is designed to be applicable to different environmental and civil engineering scenarios when parameters and boundary conditions are uncertain. In these cases, direct or inverse problems involving, e.g., risk analysis and optimizations under uncertainty need to be solved.

The first version of the code has been thought to be adaptable to different contexts and to be modifiable in straightforward manner. Figure 2.4 depicts the structure of the main program of the toolbox. Following the script, in the first function, *Setting* ( ), the user is required to set the number of uncertain parameters, M, and the maximum degree of the PCE approximation, q. The latter is typically selected to be equal to 2. If necessary, it is then subsequently increased to improve the accuracy of the approximation. The number of terms of the expansion, P, is then defined. The subsequent step is the definition of the set of regression points (see Section 2.1.2). From the knowledge of the distribution type associated with the uncertain input parameters, the user can choose the polynomial basis that optimizes the convergence rate (see Table 2.1). Figure 2.4 considers a case in which model parameters are uniform distributed and the Legendre Chaos is selected. The Legendre Chaos and the Hermite Chaos are implemented in this first version of the code as they are the most commonly used. In view of this, the function *LegendreRegP* ( ) returns automatically the set of regression points to optimize the computation of the expansion coefficients. Each regression point corresponds to a combination of values for the vector ζ (see Section 2.1.1).

```
% SFERA v1.0 - MAIN PROGRAM
% Version: 25/9/2012
clc
clear variables
% PROBLEM SETTING
Setting();
% REGRESSION POINTS DEFINITION
LegendreRegP();
% PCE GENERATION
LegendrePCE();
% REGRESSION-BASED APPROACH
TransfRegP();
PCECoef();
% GSA through PCE
LegendreGSA();
```

Figure 2.4. Basic main program of the MATLAB toolbox

The function *LegendrePCE* ( ) builds the multivariate polynomial expansion which is then computed at the standardized regression points previously identified. At this stage the coefficients, a_i, are still unknown. Note that, up to this point, the only information which is requested from the user are the values of q and M and the identification of the suitable basis of polynomials.

In the subsequent steps the PCE-based surrogate model is defined according to the specific of the particular target scenario, i.e. on the basis of (i) the original analytical or numerical model, and (ii) the uncertainty associated with model parameters. The function *TransfRegP* ( ) returns the combinations of model parameters collected in **p** and corresponding to the

standardized regression points ζ which were previously computed. As described in Section 2.1.1, **p** and ζ are related via a simple isoprobabilistic transform. This transform is performed by calling the function *LegendreIsopTr* ( ) as depicted in Figure 2.5 where *N* is the number of regression points that are collected in the rows of the matrix CSI. The user is required to modify this function by introducing the distributions of the model input parameters for the selected case study.

```
function  TransfRegP()
…
for i=1:N
    X(i,:)=LegendreIsopTr(CSI(i,:));
end
…
end
```

```
function  [X]=LegendreIsopTr(CSI1)
PCSI=unifcdf(CSI1,-1,1);
%Function test 1
%x1: uniformly distributed in [-0.5;0.5]
ax1   = -0.5;
bx1   = 0.5;
X(1)  = unifinv(PCSI(1),ax1,bx1);
%x2: uniformly distributed in [-0.5;0.5]
ax2   = -0.5;
bx2   = 0.5;
X(2)  = unifinv(PCSI(2),ax2,bx2);
end
```

Figure 2.5. Isoprobabilistic transform of the set of regression points.

Continuing with the Main program, the function *PCECoef* ( ), depicted in Figure 2.6, evaluates the original model at the combinations of model parameters corresponding to the standardized regression points and computes the expansion coefficients in vector **a** trough the regression-based approach described in Section 2.1.2. The function *ModelEval* ( ) is called in the script. This function is the only part that the user is required to change with the original model considered.

Finally, once the PCE surrogate model is built, the function *LegendreGSA* ( ) returns analytically the Sobol indices for the GSA, according to what is described in Section 2.2.2.

```
function PCECoef()
…
for ind=1:N
    fY(ind)=ModelEval(X(ind,:));
end
…
end
```

```
function [y]=ModelEval(I)
% Evaluation - regression points
% Function test 1
x1=I(1);
x2=I(2);
y=4*(x1^2)+3*x2;
end
```

Figure 2.6. Regression-based method for the definition of the PCE surrogate-model.

2.4 TEST CASES AND VALIDATION

In this section some application examples of the numerical code developed for PCE-based analysis are provided. A first simple mathematical function is adopted to clarify the key steps run by the code; then a case study in the context of groundwater flow is considered and a comparison against a traditional MC approach is presented. Finally, some examples related to the implementation of the Karhunen-Loeve expansion is provided.

2.4.1 PCE of a polynomial function

We start the illustration of our suite of examples by considering a simple polynomial format which enables one to illustrate the key steps embedded in the application of the numerical code based on the model reduction strategy presented in the first two sections of this chapter.

Consider the model function $y = f(p_1, p_2) = 4p_1^2 + 3p_2$, $(p_1, p_2) = \mathbf{p}$ being the vector of uncertain input parameters. Suppose that both p_1 and p_2 are uniformly distributed in the range $[-0.5;0.5]$. The (statistical) moments of y and the Sobol indices can be analytically determined upon calculation of integrals. These theoretical results are compared in the following with those returned by the numerical code. The latter proceeds according to these steps:

- *Step 1. Problem setting.*

In this test case the number of uncertain parameters is M = 2. The maximum degree selected for the expansion is conveniently set as q = 2. The associated PCE is then formed by $P = 6$ terms. The adopted

distributions for the parameters suggests to resort to the Legendre Chaos polynomial basis [*Xiu and Karniadakis*, 2002]. Therefore, the PCE is expressed in terms of the two random variables, ζ_1 and ζ_2, which are uniformly distributed within $[-1;1]$. Note that ζ_1 and ζ_2 represent standardized parameters which are related to p_1 and p_2 through an isoprobabilistic transform.

- *Step 2. Identification of the optimum set of regression points.*

The set of regression points is made by pairs (ζ_1,ζ_2) which are identified in the parameter space. Values for ζ_1 and ζ_2 are chosen amongst the roots of the Legendre polynomial of degree 3 (i.e., $q+1$) upon imposing the criterion of being closest to the origin and symmetric with respect to it [*Webster et al*., 1996; *Sudret*, 2008]. Table 2.2 collects the set of regression points returned by the numerical code for this test case.

ζ_1	0	-0.775	0	0.775	0	-0.775	0.775	-0.775	0.775
ζ_2	0	0	-0.775	0	0.775	-0.775	-0.775	0.775	0.775

Table 2.2. Regression points for the selected polynomial function test case.

- *Step 3. Definition of the Polynomial Chaos Expansion (PCE).*

The numerical code calculates the univariate Legendre polynomials of degree included in $[0,q]$ for each standardized parameter. The summands of the multivariate polynomial of order q are then obtained through all the possible multiplicative combinations (of degree not exceeding q) between

two univariate polynomials in ζ_1 and ζ_2, respectively. The Legendre Chaos expansion of the original model for this test case is:

$$\tilde{y} = \tilde{f}(\zeta_1, \zeta_2) = a_0 \cdot 0 + a_1 \cdot \zeta_1 + a_2 \cdot \zeta_2 + a_3 \cdot \frac{3}{2}\zeta_1^2 + a_4 \cdot \zeta_1\zeta_2 + a_5 \cdot \frac{3}{2}\zeta_2^2 . \quad (2.28)$$

- *Step 4. Computation of the expansion coefficients.*

The expansion coefficients in (2.28) are computed according to the regression based strategy discussed in Section 2.1.2. In this application the number of regression points, N, required to solve the problem is $N = P = 6$. The coefficient values returned by the code are:

$$a_0 = \frac{1}{3};\ a_2 = \frac{3}{2};\ a_3 = \frac{2}{3};\ a_1 = a_4 = a_5 = 0 . \quad (2.29)$$

The second order PCE of the original model is finally obtained by substituting (2.29) in (2.28), i.e.:

$$\tilde{y} = \tilde{f}(\zeta_1, \zeta_2) = \frac{3}{2} \cdot \zeta_2 + \zeta_1^2 . \quad (2.30)$$

- *Step 5. Uncertainty Quantification (UQ) and Global Sensitivity Analysis (GSA).*

The mean and variance of $\tilde{y}$ are $\langle \tilde{y} \rangle = a_0 = \frac{1}{3}$ and $V^{(\tilde{y})} = 0.83\overline{8}$, respectively. The calculated partial variances and Sobol indices are presented in Table 2.3. Note that these coincide with the analytical values which can be obtained through integral computation for this simple test case.

$V_1^{(\tilde{y})}$	$V_2^{(\tilde{y})}$	$S_1^{(\tilde{y})}$	$S_2^{(\tilde{y})}$	$S_{1,2}^{(\tilde{y})}$	$ST_1^{(\tilde{y})}$	$ST_2^{(\tilde{y})}$
$0.0\overline{8}$	0.75	0.106	0.894	0.000	0.106	0.894

Table 2.3. Variances and sensitivity indices for the polynomial function test case.

2.4.2 PCE for pumping tests in non-uniform aquifers

Let consider a fully penetrating well, deriving a constant flow, Q, from a non-uniform confined aquifer. In particular the configuration discussed in *Butler* [1988] is studied here. In the latter, depicted in Figure 2.7, the well is inserted at the center of a disk of radius R, embedded in an infinite matrix. The disk and the matrix are considered both uniform with respect to the flow properties.

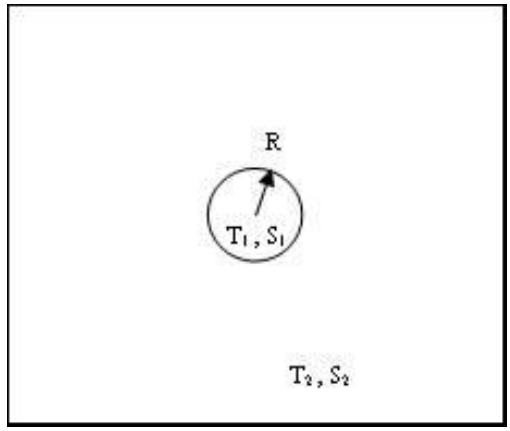

Figure 2.7. Domain schematic.

Flows in the disk and matrix are described by the following equation:

$$\frac{\partial^2 s_i}{\partial r^2}+\frac{1}{r}\cdot\frac{\partial s_i}{\partial r}=\frac{S_i}{T_i}\cdot\frac{\partial s_i}{\partial t}\,. \tag{2.31}$$

where s represents the drawdown in material i, r is the radial direction, S_i and T_i are the storage coefficient and the transmissivity of material i ($i=1$ denotes the disk while $i=2$ denotes the matrix).

To solve the problem the following initial and boundary conditions are set:

$$\lim_{r_w\to 0} 2\pi r_w T_1 \frac{\partial s_1}{\partial r}=-Q\,. \tag{2.32}$$

$$s_2(\infty,t)=0\,. \tag{2.33}$$

$$s_1(r,0)=s_2(r,0)=0,\ r_w<r<\infty,\,. \tag{2.34}$$

where r_w is the radius of the well. Finally conditions of continuity at the disk-matrix interface are included:

$$s_1(R,t)=s_2(R,t), \tag{2.35}$$

$$T_1\frac{\partial s_1(R,t)}{\partial r}=T_2\frac{\partial s_2(R,t)}{\partial r}. \tag{2.36}$$

An analytical solution of (2.31)-(2.36) is available in the Laplace space:

$$\bar{s}_1=\left(\frac{Q}{2\pi T_1}\right)\frac{K_0(Nr)}{p}+\left(\frac{Q}{2\pi T_1}\right)\frac{\left[K_1(NR)K_0(AR)-\frac{T_2}{T_1}\frac{A}{N}K_0(NR)K_1(AR)\right]I_0(Nr)}{p\left[\frac{T_2}{T_1}\frac{A}{N}I_0(NR)K_1(AR)+I_1(NR)K_0(AR)\right]}, \tag{2.37}$$

$$\bar{s}_2 = \left(\frac{Q}{2\pi T_1}\right)\frac{\left[K_0(NR)I_1(NR)+K_1(NR)I_0(NR)\right]K_0(Ar)}{p\left[\frac{T_2}{T_1}\frac{A}{N}I_0(NR)K_1(AR)+I_1(NR)K_0(AR)\right]}, \tag{2.38}$$

where $\bar{s}_1$, $\bar{s}_2$ represent the transformed drawdown in the Laplace space, p is the Laplace-transform variable, I_j is the modified Bessel function of the first kind and order j, K_j is the modified Bessel function of the second kind and order j, and $N=\sqrt{S_1 p/T_1}$ and $A=\sqrt{S_2 p/T_2}$. Equations (2.37)-(2.38) require a numerical inversion with e.g. the algorithm of *Stehfest* [1970].

Starting from this formulation [*Butler*, 1988] a specific case study is defined in which the uncertain model parameters are the transmissivities of the disk and the matrix and the storage coefficients, considered equal for the two materials. Each of these three variables is associated with a log-normal distribution and coefficient of variation equal to 0.5. The means of the distributions are $\mu_S = 5\cdot 10^{-6}$, $\mu_{T_1} = 8\cdot 10^{-3} m^2/s$, $\mu_{T_2} = 5\cdot 10^{-3} m^2/s$ (values typical of sand). The model responses of interest are the drawdowns in the two materials.

The PCE of second, third and fourth order are adopted as surrogate models on which GSA is performed.

Figure 2.8 depicts the total sensitivity indices related to the three uncertain parameters versus the radial distance from the well. It's observable that the influence of S increases far from the well while the reverse is true for T_1. The importance of the uncertainty in T_2 has a maximum value at the interface between the two materials. The

interactions among the parameters is negligible as total and principal sensitivity indices are significantly similar.

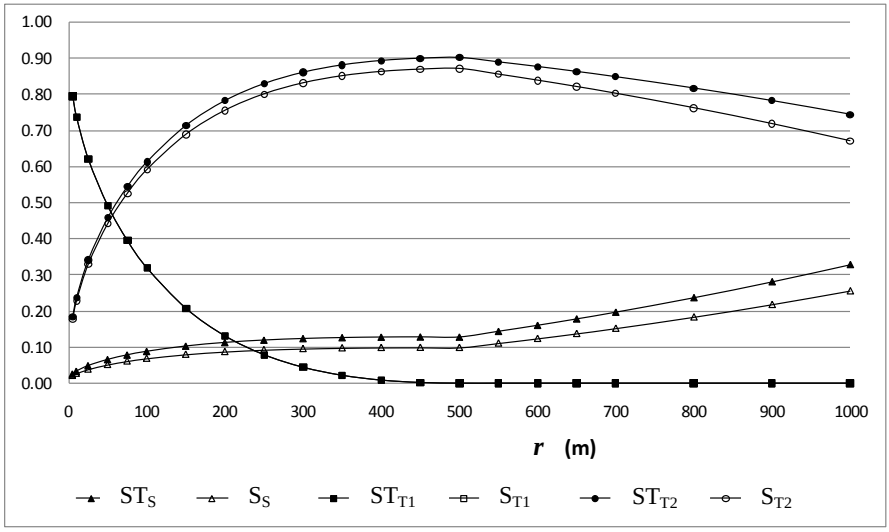

Figure 2.8. Total and principal sensitivity indices computed with the PCE of order 2 (R = 500 m ; t = 5000 s ; Q = 0.01 m3/s).

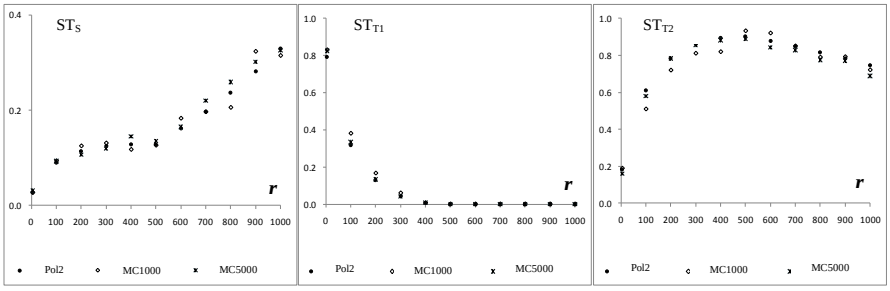

Figure 2.9. Comparison between the total sensitivity indices computed with the PCE of order 2 (Pol2) and through a traditional Monte Carlo framework (number of simulations = 1000, 5000).

As the sensitivity indices are almost constants with respect to the degree of the expansion (not shown), the results depicted are referred to the second order.

In Figure 2.9 a comparison between the sensitivity measure computed through PCE and a traditional MC framework is shown. The results of PCE appear substantially confirmed; furthermore, the latter tend to the MC-based values as the number of MC simulations increases. The advantage in terms of accuracy is added to the computational saving, equal to three orders of magnitude for the examined case.

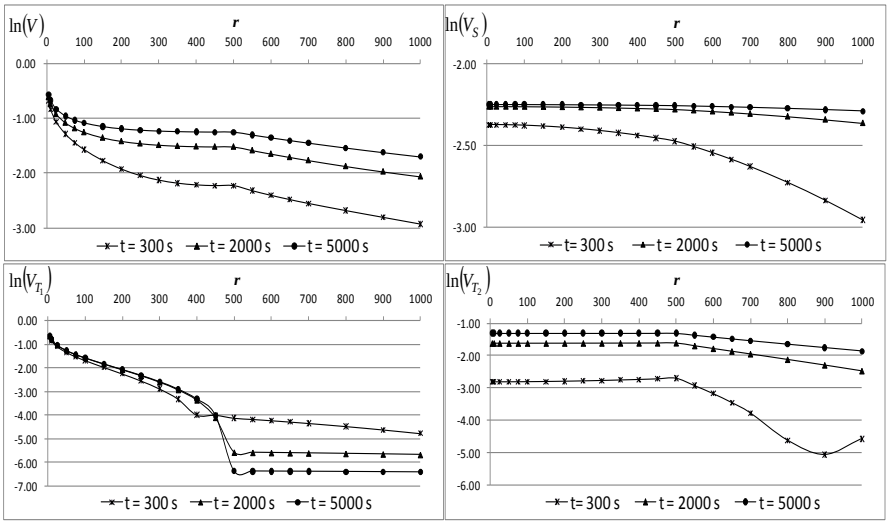

Figure 2.10. Variance maps for different times computed through the second-order PCE.

Figure 2.10 reports the maps of variances (total and partials) inside the domain for different times. For early times the drawdown in the disk is influenced only by the local properties of the system while the transmissivity of the matrix does not produce effects. This is physically consistent because the drawdown is initially confined in the material around the well. On the contrary, when tending to the stationary condition the process is dominated by the properties of the matrix even if around the well the transmissivity of the disk conserves a relevant effect. For what

concerns the drawdown in the matrix, the process is influenced only by the local properties, especially for late times.

2.4.3 KLE of some known covariance functions

In order to test the implementation of the Karhunen-Loeve Expansion according with the numerical method discussed in section 2.1.3, some well known covariance functions are here considered and the results obtained in *Phoon et al*. [2002] are adopted as a comparison.

1) *Test covariance function 1*: first-order Markov process defined in [-1;1]; exponential covariance function $C(x_1, x_2) = e^{-|x_1 - x_2|}$.

The eigenvalues obtained with the implemented code are reported in Table 2.4.

λ_k	*N*=8	*N*=16	*N*=32	*N*=64	*N*=128
1	1.1630	1.1527	1.1502	1.1495	1.1494
2	0.4042	0.3942	0.3918	0.3911	0.3910
3	0.1693	0.1600	0.1578	0.1572	0.1571
4	0.0916	0.0824	0.0803	0.0797	0.0796
5	0.0595	0.0499	0.0478	0.0473	0.0472
6	0.0441	0.0337	0.0316	0.0311	0.0310
7	0.0361	0.0246	0.0225	0.0220	0.0218
8	0.0323	0.0191	0.0168	0.0163	0.0162
9		0.0154	0.0131	0.0126	0.0125
10		0.0130	0.0105	0.0100	0.0099

Table 2.4. Eigenvalues of the first-order Markov process for different maximum Wavelet levels of the Wavelet-Galerkin approach.

For this test case, Figure 2.11 also depicts the 8th and 10th order eigenfunctions.

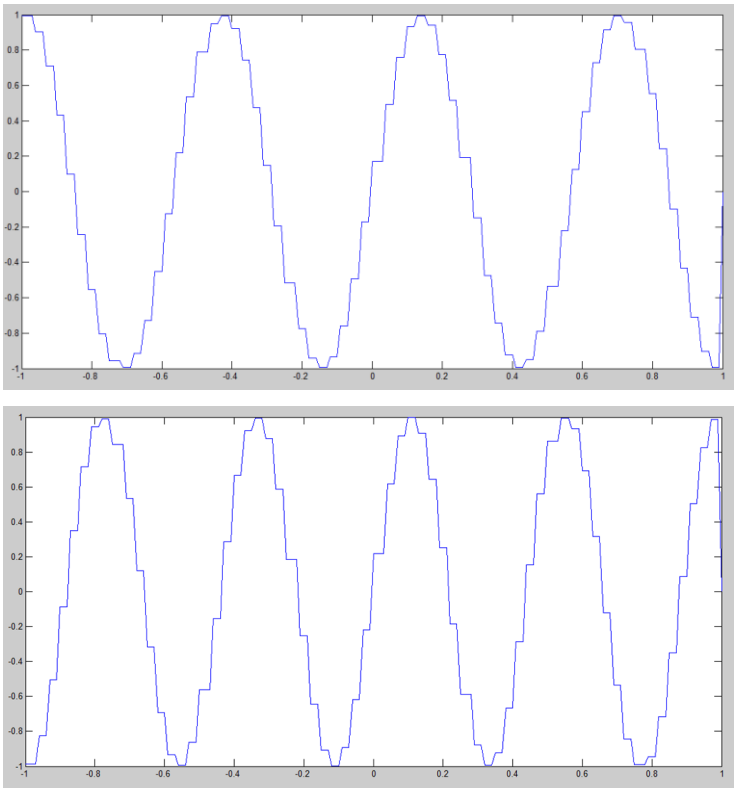

Figure 2.11. 8th and 10th order eigenfunctions for exponential covariance

2) *Test covariance function 2*: Random process defined in [-1;1]; squared exponential covariance function $C(x_1, x_2) = e^{-|x_1 - x_2|^2}$.

The eigenvalues obtained with the implemented code are reported in Table 2.5.

3) *Test covariance function 3*: Wiener–Levy process in [0,1]; covariance function $C(x_1, x_2) = \min(x_1, x_2)$.

The eigenvalues obtained with the implemented code are reported in Table 2.6.

λ_k	N=8	N=16	N=32	N=64	N=128
1	1.3078	1.3051	1.3044	1.3042	1.3042
2	0.5378	0.5364	0.5361	0.5360	0.5360
3	0.1315	0.1333	0.1338	0.1339	0.1339
4	0.0206	0.0222	0.0226	0.0227	0.0227
5	0.0022	0.0027	0.0028	0.0029	0.0029
6	0.0002	0.0003	0.0003	0.0003	0.0003
7	0.0000	0.0000	0.0000	0.0000	0.0000
8	0.0000	0.0000	0.0000	0.0000	0.0000
9		0.0000	0.0000	0.0000	0.0000
10		0.0000	0.0000	0.0000	0.0000

Table 2.5. Eigenvalues of the squared exponential covariance for different maximum Wavelet levels of the Wavelet-Galerkin approach.

λ_k	N=8	N=16	N=32	N=64	N=128
1	0.4066	0.4056	0.4054	0.4053	0.4053
2	0.0464	0.0454	0.0451	0.0451	0.0450
3	0.0176	0.0165	0.0163	0.0162	0.0162
4	0.0097	0.0086	0.0084	0.0083	0.0083
5	0.0065	0.0053	0.0051	0.0050	0.0050
6	0.0050	0.0037	0.0034	0.0034	0.0034
7	0.0043	0.0028	0.0025	0.0024	0.0024
8	0.0039	0.0022	0.0019	0.0018	0.0018
9		0.0018	0.0015	0.0014	0.0014
10		0.0015	0.0012	0.0011	0.0011

Table 2.6. Eigenvalues of the Wiener-Levy process for different maximum Wavelet levels of the Wavelet-Galerkin approach.

2.5 FINAL REMARKS

In this chapter the first version of a MATLAB-based comprehensive computational framework based on the PCE theory is described. The code has been designed to obtain consistent results in the context of GSA and RA at a reduced computational cost.

Once the basis of the PCE theory have been revised, the main features of the numerical code are provided also with the aid of some test examples. In particular it is shown that the proposed methodology (a) provides a surrogate model in a simple polynomial form on which is possible extending the number of runs for simulation purposes (b) allows identifying the different influence of the uncertain model parameters (c) leads to considerable saving of computational time while keeping acceptable accuracy.

3. Application to analytical formulations

SOMMARIO

In questo capitolo si presenta lo sviluppo di una nuova formulazione analitica utile ad interpretare i fenomeni chiave legati allo spiazzamento di fluidi non-Newtoniani nel sottosuolo. Tale formulazione è accompagnata da un'analisi approfondita del modello ottenuto, capace di tener conto dell'incertezza associata ai parametri rilevanti del problema. Le dinamiche di un'interfaccia stabile e mobile in geometria radiale sono considerate all'interno di un dominio poroso saturato da due fluidi, entrambi non-Newtoniani, assumendo che pressione e velocità siano continue all'interfaccia e che la pressione iniziale sia costante. La legge del moto considerata per entrambi i fluidi è una legge di Darcy modificata. Accoppiando le leggi del moto non lineari con l'equazione di continuità e tenendo conto degli effetti di compressibilità, si ottiene un sistema di equazioni alle derivate parziali del secondo ordine non lineari. Considerando che i due fluidi abbiano lo stesso indice reologico, n, è possibile trasformare le equazioni precedenti attraverso l'introduzione di una variabile auto-simile. Ulteriori trasformazioni delle equazioni che includono le condizioni all'interfaccia, mostrano per $n<1$ l'esistenza di un fronte di compressione dinnanzi all'interfaccia mobile. Risolvendo le equazioni ottenute si ottengono, in forma chiusa per qualsiasi valore di n, la posizione dell'interfaccia, del fronte di compressione e la distribuzione

della pressione. A partire dal modello precedentemente descritto, le analisi relative alla propagazione dell'incertezza e alla sensitività globale sono sviluppate con il codice di calcolo introdotto nel precedente capitolo. Queste analisi hanno permesso di verificare come l'incertezza legata ai parametri chiave del problema influenzi le variabili di stato di interesse. La bontà dei risultati ottenuti attraverso il codice basato sull'espansione in Caos Polinomiale è stata verificata attraverso un confronto con un approccio tradizionale di tipo Monte Carlo. Da tale confronto non è emersa soltanto l'accuratezza dei risultati ottenuti ma anche il sensibile risparmio in termini di onere computazionale pur trattandosi di un'applicazione che vede coinvolta una formulazione di tipo analitico. Il lavoro presentato in questo capitolo è incluso in *Ciriello and Di Federico* [2013], a valle di studi analoghi sul flusso di fluidi non-Newtoniani nel sottosuolo (*Di Federico and Ciriello* [2012], *Ciriello and Di Federico* [2012]).

3.1 NON-NEWTONIAN DISPLACEMENT IN POROUS MEDIA

Displacement phenomena in porous media involving non-Newtonian fluid behavior are of considerable interest in several areas of engineering and physics. In petroleum engineering, various substances injected into underground reservoirs to enhance oil recovery, by improving the overall sweeping efficiency and minimizing instability effects, reveal a nonlinear stress-shear rate relationship and other non-linear effects [*Wu and Pruess*, 1996]: these include dilute polymer solutions, emulsions of surfactants and foams. On the other hand, heavy and waxy oils are often found to exhibit non-Newtonian characteristics at reservoir conditions [*Pedersen and Ronningsen*, 2000]; therefore a situation may be envisaged in which a non-Newtonian fluid injected into a reservoir displaces another non-Newtonian fluid with different rheological characteristics. A similar situation may arise in environmental remediation efforts geared towards in situ treatment, where injection of substances having nonlinear rheological properties such as colloidal or biopolymer suspensions is employed to remove, or favor the removal of, liquid pollutants from contaminated soils; relevant examples include DNAPLs remediation by means of colloidal liquid aphrons [*Li Yan et al.*, 2011], and the use of xanthan gum to enhance mobility and stability of suspensions of nanoscale iron employed in reactive barriers [*Comba et al.*, 2011]. As in situ bioremediation may create polymers with non-Newtonian characteristics [*Hung et al.*, 2010], a subsequent injection may result in displacement of a non-Newtonian fluid by another. Similar situations may arise in industrial engineering, where non-Newtonian flows occur in filtration of polymer melts, food processing, and fermentation [*Chabra et al.*, 2001], and in orthopedic applications, where injectable

cements used in a variety of bone augmentation and bone reconstruction procedures also display a complex rheology [*Lewis*, 2011].

The displacement phenomenon of a fluid by another in a porous domain has been extensively investigated in the literature when either fluid, or both, exhibit non-Newtonian behavior. *Pascal* [1984a] adopted Muskat's frontal advance model to study steady-state immiscible displacement of a Bingham fluid by another in plane/radial geometry. Steady-state displacement, and its stability, were analyzed in *Pascal* [1984b] for power-law fluids with yield stress in plane geometry, and in *Pascal* [1986] for power-law fluids in radial geometry; capillarity was added to the model in *Pascal* [1988]. In *Pascal and Pascal* [1988], transient plane displacement of a power-law compressible fluid by another was considered. In *Pascal* [1990] and *Pascal* [1992], transient plane/radial displacement of a power-law fluid by another was considered, allowing for two-phase flow behind the displacement front but neglecting compressibility. An analytical solution for piston-like displacement of power-law dilatant fluids in plane and radial geometry was derived in *Chen and Liu* [1991]. In *Wu et al.* [1991] an analytical solution of Buckley–Leverett type to two-phase flow determined by the displacement of a Newtonian fluid by a non-Newtonian power-law one was obtained and validated by a numerical model. *Wu and Pruess* [1998] developed a numerical simulator for multiphase flow in porous media, including the power-law and Bingham models. A novel two-phase numerical simulator incorporating non-Newtonian behavior was proposed in *Zhu et al.* [2002]. *Tsakiroglou* [2004] generalized the macroscopic equations of the two-phase flow in porous media accounting for capillarity for the case of a shear-thinning displacing fluid, and developed a numerical scheme of inverse modeling to estimate model parameters from unsteady-state

experiments. Other researchers investigated the onset of instabilities in displacement of non-Newtonian fluids experimentally [*Al-Attar*, 2011] or theoretically [*Kim and Cho*, 2011].

If a fingering instability does not develop at the interface between displacing and displaced fluid, the frontal advance theory may be considered an approximate yet acceptable description of the displacement mechanism, with the advantage of providing analytical solutions, which in turn may prove useful as benchmarks against which numerical solvers are tested. An example of such solutions was provided by *Pascal and Pascal* [1988], who derived a similarity solution for planar transient immiscible displacement of a power-law compressible fluid by another with the same flow behavior index. The study of the radial case (e.g. flow away from a wellbore), which represents a plausible simplification of the geometry involved in several possible applications, is developed in this work. The assumption of identical flow behavior index for displacing and displaced fluid is retained to derive a closed-form solution in the format of a system of algebraic nonlinear equations. As values on flow behavior index in real applications, especially connected to reservoir engineering, tend to cluster around 0.6-0.8 [*Di Federico et al.*, 2010], the proposed solution may provide a qualitative insight on relevant physical phenomena also for fluids whose flow behavior index differ to some extent. The problem is formulated in dimensionless form for different types of boundary conditions in the origin of the flow domain (assigned pressure or flow rate), and novel closed-form expressions of the pressure field in the displacing and displaced fluids for a generic value of the flow law exponent are derived generalizing to two fluids the results of *Ciriello and Di Federico* [2012]; a discussion of deterministic results is then provided.

Uncertainty plagues virtually every effort to predict the behaviour of complex physical systems; in the problem under investigation, it affects to various degrees: a) the properties of the porous medium, due to its inherent spatial heterogeneity and lack of complete characterization; b) the descriptive parameters of the fluids involved, having a complex rheological behavior. In the first case, a random field description [e.g., *Dagan*, 1989] represents the most complete methodology. In the sequel, to exemplify the approach and achieve easily interpretable indications, the key problem parameters are modeled as independent random variables having an assigned probability distribution.

In this work, the adoption of GSA conducted by means of PCE allows to study how uncertainty affecting selected parameters propagates to state variables adopting the benchmark analytical model of non-Newtonian radial displacement derived earlier. The goodness of the results obtained by the PCE is then assessed by comparison against a traditional Monte Carlo (MC) approach.

3.2 ANALYTICAL MODEL AND SIMILARITY SOLUTION

3.2.1 Flow law for power-law fluid in a porous media

Flow of Newtonian fluids in porous media is governed by Darcy's law. Its extension to non-Newtonian fluids is complex, due to interactions between the microstructure of porous media and the rheology of the fluid, even in the creeping flow regime. The scientific literature of the past decades includes numerous works dedicated to this problem: for exhaustive reviews see [*Chabra et al.*, 2001]. A sizable part of them deals with power-law fluids, described by the rheological Ostwald-DeWaele model, given for simple shear flow by

$$\tau = m\dot{\gamma}\left|\dot{\gamma}\right|^{n-1}, \tag{3.1}$$

in which τ is the shear stress, $\dot{\gamma}$ the shear rate, m [$ML^{-1}T^{n-2}$] and n indices of fluid consistency and flow behavior respectively, with $n<1$, $=1$ or >1 describing respectively pseudoplastic, Newtonian, or dilatant behavior. The power-law model, itself a simplification of more complex, and realistic, rheological behavior, is nevertheless often adopted in both porous media and free-surface flow modeling for its simplicity [*Ruyer-Quil et al.*, 2012]. The corresponding modified version of Darcy's law takes in the literature the two equivalent forms [*Cristopher and Middleman*, 1965; *Pascal*, 1983; *Nield and Bejan*, 2006]

$$\nabla P = -\frac{\mu_{ef}}{k}\left|\mathbf{v}\right|^{n-1}\mathbf{v} = -\frac{m}{k^{*}}\left|\mathbf{v}\right|^{n-1}\mathbf{v}, \tag{3.2}$$

where $P = p + \rho g z$ is the generalized pressure, p the pressure, z the vertical coordinate, ρ the fluid density, g the specific gravity, $\mathbf{v}$ the Darcy flux, k the intrinsic permeability coefficient [L^2], μ_{ef} the effective viscosity [$ML^{-n}T^{n-2}$], k^* the generalized permeability [L^{n+1}]; the ratio k/μ_{ef}, termed mobility, is given by [Pascal and Pascal, 1985]

$$\frac{k}{\mu_{ef}} = \frac{1}{2m}\left(\frac{n\phi}{3n+1}\right)^{n}\left(\frac{8k}{\phi}\right)^{(1+n)/2}. \tag{3.3}$$

where ϕ denotes the porosity. For $n=1$, the effective viscosity μ_{ef} reduces to conventional viscosity μ, and Eq. (3.2) reduces to Darcy's law $\nabla P = -(\mu/k)\mathbf{v}$. Earlier literature reviews [e.g. *Di Federico et al.*, 2010] demonstrate that the bulk of applications to non-Newtonian flows in porous

media involve pseudoplastic fluids with n mainly in the range 0.5÷1, yet dilatant behavior is sometimes encountered.

3.2.2 Problem formulation

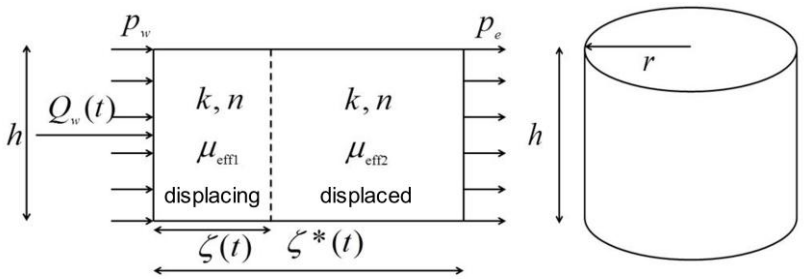

Figure 3.1. Domain schematic (either p_w or Q_w is assigned).

A well of radius r_w located in the center of a porous domain of infinite horizontal extent is considered. Constant thickness h, and uniform properties, are assumed to analyze the dynamics of a moving interface due to injection at the well of a non-Newtonian fluid into the domain, initially saturated by another non-Newtonian fluid (Figure 3.1); both fluids, displacing and displaced, are of power-law pseudo-plastic behavior with the same consistency index n. The interface between the fluids is considered to be stable and sharply defined, so that a piston-like displacement exists. The pressure and velocity fields are assumed to be continuous at the interface; the pressure is taken to be constant and equal to p_e in the domain occupied by the displaced fluid at time $t = 0$; the displacing fluid is injected at a constant pressure p_w greater than the ambient pressure p_e, or at a given injection rate $Q_w(t)$.

The flow and continuity equation for both fluids ($i=1$ for the displacing, $i=2$ for the displaced) are:

$$v_i = \left(-\frac{k}{\mu_{efi}} \frac{\partial p_i}{\partial r} \right)^{1/n}, \tag{3.4}$$

$$\frac{\partial v_i}{\partial r} + \frac{v_i}{r} = -c_{0i}\phi \frac{\partial p_i}{\partial t}, \tag{3.5}$$

where the Darcy velocities v_i are the one-dimensional counterparts of (3.2). In (3.4)-(3.5) r denotes the radial spatial coordinate, t time, ϕ and k the domain porosity and permeability, p_i and $c_{0i} = c_{fi} + c_p$ the pressures and total compressibility coefficients in the two flow regions, with c_{fi} being the fluid compressibility coefficient and c_p the porous medium compressibility coefficient. The relative influence of fluid and medium behavior on the total compressibility coefficient may vary widely, depending on their nature, and ranges from cases where one is negligible compared to the other to instances where the two effects are of the same order. In the CO_2 storage application presented by *Zhou et al.* [2008], brine and formation take the respective compressibilities $c_f = 3.5 \cdot 10^{-10}$ Pa^{-1} and $c_p = 4.5 \cdot 10^{-10}$ Pa^{-1}. In enhanced oil recovery applications, the fluid compressibility coefficient typically lies in the range $1 \div 5 \cdot 10^{-9}$ Pa^{-1} [*Pascal*, 1991], while according to *Pascal and Pascal* [1988], the total compressibility coefficient c_0 may vary between $1 \cdot 10^{-8}$ and $5 \cdot 10^{-8}$ Pa^{-1}, implying a larger influence of medium compressibility. An example illustrating the differences between compressibilities for different fluids is the water–oil displacement case study presented by *Fokker and Verga*

[2011], where water, oil and rock compressibility are taken equal respectively to $4.5\cdot10^{-10}$, $1.3\cdot10^{-9}$ and $5\cdot10^{-10}$ Pa^{-1}. In general, oscillations between typical fluid compressibility values seem to be of one order of magnitude, while formation compressibility varies in a larger interval [*Di Federico and Ciriello*, 2012].

Substituting (3.4) in (3.5) one obtains for the two fluids ($i=1,2$):

$$\frac{\partial^2 p_i}{\partial r^2}+\frac{n}{r}\frac{\partial p_i}{\partial r}=nc_{0i}\phi\left(\frac{\mu_{efi}}{k}\right)^{1/n}\left(-\frac{\partial p_i}{\partial r}\right)^{(n-1)/n}\frac{\partial p_i}{\partial t}, \tag{3.6}$$

where $p_i(r,t)=p_1(r,t)$ for $0\le r\le\zeta(t)$ and $p_i(r,t)=p_2(r,t)$ for $\zeta(t)\le r<\infty$, with $\zeta(t)$ being the interface position; since the injection starts at $t=0$, $\zeta(0)=0$.

The initial condition for the displaced fluid is

$$p_2(r,0)=p_e. \tag{3.7}$$

Designated boundary conditions at the well $r=r_w$ are either constant pressure p_w or flow rate $Q_w(t)$, indicated in the sequel as b.c. 1) and 2)),:

$$p_1(r_w,t)=p_w, \tag{3.8}$$

$$v_1(r_w,t)=\left(-\frac{k}{\mu_{ef1}}\frac{\partial p_1}{\partial r}\right)^{1/n}_{r=r_w}=\frac{Q_w(t)}{2\pi hr_w}, \tag{3.9}$$

The expression of the injected flow rate for the second-type boundary condition is taken to be

$$Q_w(t)=Q_0t^c, \tag{3.10}$$

where $Q_0(>0)$ is the injection intensity and c a real number. Lastly, the pressure within the displaced fluid at infinity equals the ambient pressure, i.e.

$$\lim_{r\to\infty} p_2(r,t) = p_e\,. \tag{3.11}$$

At the moving interface, the pressure and velocity fields are continuous; thus

$$p_1[\zeta(t),t] = p_2[\zeta(t),t], \tag{3.12}$$

$$\left(-\frac{k}{\mu_{ef1}}\frac{\partial p_1}{\partial r}\right)^{1/n}_{r=\zeta(t)} = \left(-\frac{k}{\mu_{ef2}}\frac{\partial p_2}{\partial r}\right)^{1/n}_{r=\zeta(t)} = V = \phi\frac{d\zeta}{dt}\,, \tag{3.13}$$

in which V is the common value of the Darcy velocity at the interface.

The following dimensionless variables are then defined ($i=1,2$):

$$\begin{aligned}&(r', r_w', \zeta', h', t', p_i', v_i', V', Q_w', Q_0') = \\ &\left(\frac{r}{L}, \frac{r_w}{L}, \frac{\zeta}{L}, \frac{h}{L}, \frac{t}{T}, c_{01}p_i, \frac{v_i T}{L}, \frac{VT}{L}, \frac{QT}{L^3}, \frac{Q_0 T^{1-c}}{L^3}\right)\end{aligned} \tag{3.14}$$

where L is an arbitrary length scale of the order of the domain's thickness h,

$$T = m_1^{1/n} c_{01}^{1/n} L^{(n+1)/n} \big/ k_0^{(1+n)/2n} \tag{3.15}$$

is a timescale, and k_0 a reference permeability. With $L \approx h \approx 10\,\mathrm{m}$, $c_{01} \approx 10^{-8}\,\mathrm{Pa}^{-1}$, $m_1 \approx 1\,\mathrm{Pa}\cdot\mathrm{s}^{\mathrm{n}}$, $k_0 \approx 10^{-12}\,\mathrm{m}^2$, one has $T \approx 10^5\,\mathrm{s} \approx 1$ day for $n = 0.5$. The dimensionless form of (3.4) and (3.5) is therefore (primes are dropped for convenience)

$$v_1 = \frac{\phi}{A}\left(-\frac{\partial p_1}{\partial r}\right)^{1/n}, \tag{3.16}$$

$$v_2 = \frac{\phi M^{1/n}}{A}\left(-\frac{\partial p_2}{\partial r}\right)^{1/n}, \tag{3.17}$$

$$\frac{\partial^2 p_1}{\partial r^2} + \frac{n}{r}\frac{\partial p_1}{\partial r} = nA\left(-\frac{\partial p_1}{\partial r}\right)^{(n-1)/n}\frac{\partial p_1}{\partial t}, \tag{3.18}$$

$$\frac{\partial^2 p_2}{\partial r^2} + \frac{n}{r}\frac{\partial p_2}{\partial r} = n\frac{\alpha A}{M^{1/n}}\left(-\frac{\partial p_2}{\partial r}\right)^{(n-1)/n}\frac{\partial p_2}{\partial t}, \tag{3.19}$$

where the quantities

$$A = A(n,\phi,K) = \frac{\phi^{(1+n)/2n}}{\chi_n^{1/n} K^{(1+n)/2n}},\ \chi_n = 8^{(1+n)/2}\left(n/(3n+1)\right)^n/2, \tag{3.20a,b}$$

reduce for $n=1$ to $A=\phi/K$ and $\chi_n = 1$, and

$$M = (k/\mu_{ef2})/(k/\mu_{ef1}) = m_1/m_2,\ \alpha = c_{02}/c_{01}, K = k/k_0, \tag{3.21a,b,c}$$

are respectively the mobility ratio, the compressibility ratio, and the dimensionless permeability.

Initial and boundary conditions (3.7), (3.8) and (3.11), and condition at the interface (3.12) remain unchanged in dimensionless form. Boundary condition (3.9) becomes

$$v_1(r_w,t) = \frac{\phi}{A}\left(-\frac{\partial p_1}{\partial r}\right)_{r=r_w}^{1/n} = \frac{Q_w(t)}{2\pi h r_w}. \tag{3.22}$$

Interface condition (3.13) reads in dimensionless form (primes omitted)

$$\frac{\phi}{A}\left(-\frac{\partial p_1}{\partial r}\right)^{1/n}_{r=\varsigma(t)} = \frac{\phi M^{1/n}}{A}\left(-\frac{\partial p_2}{\partial r}\right)^{1/n}_{r=\varsigma(t)} = V = \phi\frac{d\zeta}{dt}. \tag{3.23}$$

3.2.3 Similarity solution

Adopting the similarity variable

$$\eta = \frac{r}{t^{n/(n+1)}}, \tag{3.24}$$

equations (3.16)-(3.17) and (3.18)-(3.19) take the form

$$v_1 = \frac{\phi}{A}t^{-1/(n+1)}\left(-\frac{dp_1}{d\eta}\right)^{1/n}, \tag{3.25}$$

$$v_2 = \frac{\phi M^{1/n}}{A}t^{-1/(n+1)}\left(-\frac{dp_2}{d\eta}\right)^{1/n}, \tag{3.26}$$

$$\frac{d^2p_1}{d\eta^2} + \frac{n}{\eta}\frac{dp_1}{d\eta} = \frac{n^2}{n+1}A\eta\left(-\frac{dp_1}{d\eta}\right)^{(2n-1)/n} \quad (0 \le \eta \le \eta_1), \tag{3.27}$$

$$\frac{d^2p_2}{d\eta^2} + \frac{n}{\eta}\frac{dp_2}{d\eta} = \frac{n^2}{n+1}\frac{\alpha A}{M^{1/n}}\eta\left(-\frac{dp_2}{d\eta}\right)^{(2n-1)/n} \quad (\eta_1 \le \eta < \infty), \tag{3.28}$$

where η_1 is linked to the position of the moving interface by

$$\zeta(t) = \eta_1 t^{n/(1+n)}. \tag{3.29}$$

The first-kind and second-kind boundary conditions at the well (3.8) and (3.22) become respectively

$$p_1(\eta_w) = p_w, \tag{3.30}$$

$$\left(-\frac{dp_1}{d\eta}\right)^{1/n}_{\eta=\eta_w} = \frac{A}{\phi}\frac{Q_w(t)}{2\pi h r_w}t^{1/(1+n)}, \tag{3.31}$$

where $\eta_w = \eta(r_w, t)$. Initial and boundary conditions (3.7) and (3.11) expressed in terms of η transform into

$$\lim_{\eta\to\infty} p_2(\eta) = p_e. \tag{3.32}$$

The conditions at the interface (3.12) and (3.23) become

$$p_1(\eta_1) = p_2(\eta_1), \tag{3.33}$$

$$\left(\frac{dp_1}{d\eta}\right)_{\eta=\eta_1} = M\left(\frac{dp_2}{d\eta}\right)_{\eta=\eta_1}. \tag{3.34}$$

The interface velocity takes the form

$$V = \phi\frac{d\zeta}{dt} = \frac{\phi}{A}\left(-\frac{dp_1}{d\eta}\right)^{1/n}_{\eta=\eta_1} t^{-1/(1+n)}. \tag{3.35}$$

Integrating (3.35) with the initial condition $\zeta(0) = 0$ yields

$$\zeta(t) = \frac{1+n}{nA}\left(-\frac{dp_1}{d\eta}\right)^{1/n}_{\eta=\eta_1} t^{n/(1+n)}. \tag{3.36}$$

Coupling (3.29) and (3.36) leads to the following expression for η_1

$$\eta_1 = \zeta(t)t^{-n/(1+n)} = \frac{1+n}{nA}\left(-\frac{dp_1}{d\eta}\right)^{1/n}_{\eta=\eta_1}, \tag{3.37}$$

and taking (3.34) and (3.37) into account yields

$$\left(-\frac{dp_2}{d\eta}\right)_{\eta=\eta_1} = \frac{1}{M}\left(-\frac{dp_1}{d\eta}\right)_{\eta=\eta_1} = \frac{1}{M}\left(\frac{nA}{1+n}\eta_1\right)^n . \tag{3.38}$$

Equations (3.27)-(3.28) are Bernoulli differential equations; their integration with (3.38) yields respectively

$$\frac{dp_1}{d\eta} = -\eta^{-n}\left(a_1 - b_1\eta^{3-n}\right)^{n/(1-n)} \left(\eta_w \le \eta \le \eta_1\right), \tag{3.39}$$

$$\frac{dp_2}{d\eta} = -\eta^{-n}\left(a_2 - b_2\eta^{3-n}\right)^{n/(1-n)} \left(\eta_1 \le \eta < \infty\right), \tag{3.40}$$

in which

$$a_1 = a_1(\eta_1, n, \phi, K) = \left(\frac{nA}{1+n}\right)^{1-n} \eta_1^{2(1-n)} + \frac{n(1-n)A}{(1+n)(3-n)}\eta_1^{3-n}, \tag{3.41}$$

$$b_1 = b_1(n, \phi, K) = \frac{n(1-n)A}{(1+n)(3-n)}, \tag{3.42}$$

$$a_2 = a_2(\eta_1, n, \phi, K, M, \alpha) = \left(\frac{n}{1+n}\frac{A}{M^{1/n}}\right)^{1-n} \eta_1^{2(1-n)} + \frac{n(1-n)}{(1+n)(3-n)}\frac{\alpha A}{M^{1/n}}\eta_1^{3-n}, \tag{3.43}$$

$$b_2 = b_2(n, \phi, K, M, \alpha) = \frac{n(1-n)}{(1+n)(3-n)}\frac{\alpha A}{M^{1/n}} . \tag{3.44}$$

From (39) it is evident that when $n<1$, $dp_2/d\eta = 0$ for

$$\eta^* = c_1\eta_1;$$

$$c_1 = c_1(\eta_1, n, \phi, K, M, \alpha) = \left[1 + \frac{(1+n)^n(3-n)M}{n^n(1-n)\alpha A^n \eta_1^{1+n}}\right]^{1/(3-n)} > 1 \tag{3.45}$$

Equations (3.40) and (3.45) show for a pseudoplastic fluid ($n<1$) the existence of a compression front ahead of the moving interface, whose

dimensionless position and velocity ζ^* and V^* (defined in analogy to ζ and V) are given by

$$\zeta^*(t) = \eta^* t^{n/(1+n)};\ V^* = \phi \frac{d\zeta^*}{dt} = \frac{n\phi}{n+1} \eta^* t^{-1/(1+n)}. \tag{3.46}$$

At and beyond the compression front, the displaced fluid Darcy velocity v_2 is null; hence, the fluid remains at the constant ambient pressure p_e for $\eta \geq \eta^*$. Therefore, (3.40) holds in the interval $\eta_1 \leq \eta < \eta^*$, and the boundary condition (3.32) is replaced for $n < 1$ by

$$p_2(\eta^*) = p_e. \tag{3.47}$$

The velocities of displacing and displaced fluid can then be derived as

$$v_1(t,\eta) = \frac{\phi}{A} \frac{t^{-1/(1+n)}}{\eta} \left(a_1 - b_1 \eta^{3-n}\right)^{1/(1-n)} \quad (\eta_w \leq \eta \leq \eta_1), \tag{3.48}$$

$$v_2(t,\eta) = \frac{\phi M^{1/n}}{A} \frac{t^{-1/(1+n)}}{\eta} \left(a_2 - b_2 \eta^{3-n}\right)^{1/(1-n)} \quad (\eta_1 \leq \eta < \eta^*). \tag{3.49}$$

The actual value of the front position η_1 in (3.41)-(3.49) may be derived by means of the boundary condition at the well (either (3.30) or (3.31)), the interface condition (3.33), and (3.47).

For b.c. 1) (assigned constant pressure at the well), taking (3.30) and (3.47) into account, the integration of (3.39)-(3.40) yields respectively

$$p_1(\eta) = p_w - \left[I(a_1, b_1, n, \eta) - I(a_1, b_1, n, \eta_w)\right], \tag{3.50}$$

$$p_2(\eta) = p_e + \left[I(a_2, b_2, n, \eta^*) - I(a_2, b_2, n, \eta)\right], \tag{3.51}$$

where ($i = 1,2$)

$$I(a_i,b_i,n,\tau)=\int \tau^{-n}\left(a_i-b_i\tau^{3-n}\right)^{n/(1-n)}d\tau= \\ \frac{a_i^{n/(1-n)}\tau^{1-n}}{1-n}\cdot {}_2F_1\left(\frac{1-n}{3-n},-\frac{n}{1-n},\frac{2(2-n)}{3-n},\frac{b_i\tau^{3-n}}{a_i}\right) \tag{3.52}$$

with ${}_2F_1$ being the hypergeometric function. Appendix A reports simpler expressions of (3.52), valid for certain special values of flow behavior index n.

On the other hand, (3.50)-(3.51) and the interface condition (33) give

$$\Delta p = p_w - p_e = \\ \left[I(a_1,b_1,n,\eta_1)-I(a_1,b_1,n,\eta_w)\right]+\left[I(a_2,b_2,n,\eta^*)-I(a_2,b_2,n,\eta_1)\right] \tag{3.53}$$

Note that in (3.50) and (3.53), $I(a_1,b_1,n,\eta_w)$ may be set to zero given that $\eta_w \cong 0$ since $\eta_w << \eta$. As the total pressure drop Δp between well and reservoir is known, the only unknown in the implicit algebraic equation (3.53) is η_1; once η_1 is determined, η^* is then calculated through (3.45), and the pressure distributions behind and ahead the moving interface are evaluated via (3.50)-(3.51).

Finally, the injection flow necessary to maintain p_w at the well under the approximation $\eta_w \cong 0$ is given by

$$Q_w(t)=2\pi h r_w v_1(\eta_w,t)=\frac{2\pi h\phi}{A}\left(a_1-b_1\eta_w^{3-n}\right)^{1/(1-n)}t^{-(1-n)/(1+n)}\cong \\ \frac{2\pi h\phi a_1^{1/(1-n)}}{A}t^{-(1-n)/(1+n)} \tag{3.54}$$

that is a decreasing function of time for a pseudoplastic fluid.

For b.c. 2) (assigned time-variable flow rate at the well), using (3.31) and (3.38) with $\eta_w \cong 0$ yields again (3.54). A self-similar solution is possible in this case only when

$$Q_w(t) = Q_0 t^{-(1-n)/(1+n)}, \tag{3.55}$$

with Q_0 being the injection intensity defined in (3.10) and non-dimensionalized via (3.14). Taking (3.54) and (3.55) into account, the value of η_1 is determined solving the implicit algebraic equation

$$a_1(\eta_1, n, \phi, K) = \left(\frac{Q_0 A}{2\pi h \phi}\right)^{1-n}. \tag{3.56}$$

Once η_1 is known, the position of the compression front η^* is derived via (3.45), while the pressure in the displaced fluid $p_2(\eta)$ is given again by (3.51), albeit with a different value of η^*. To derive the pressure in the displacing fluid $p_1(\eta)$, (3.39) is integrated between η and η_1, yielding with the help of (3.34)

$$\begin{aligned} p_1(\eta) = p_e + \left[I(a_1, b_1, n, \eta_1) - I(a_1, b_1, n, \eta)\right] + \\ \left[I(a_2, b_2, n, \eta^*) - I(a_2, b_2, n, \eta_1)\right] \end{aligned}. \tag{3.57}$$

For $\eta = \eta_w$, (3.57) gives the pressure $p_w(\eta)$ at the injection well when the time variable injection rate is given by (3.55).

When $n > 1$, no pressure front is present and boundary condition (3.32) holds; integrating (3.39)-(3.40) yields for assigned constant pressure at the well (b.c. 1) an integral which is divergent in the origin $\eta_w = 0$; therefore no similarity solution exists in this case. For assigned flow rate at the well (b.c. 2), a self-similar solution is possible only for $1 < n < 3$ and

when the injection rate is given by (3.55), which for dilatant fluids is an increasing function of time. Hence integrating (3.39)-(3.40) with (3.31), (3.32), (3.33) and (3.55) gives (note that in this case $b_i < 0$)

$$p_1(\eta) = p_e + \left[I(a_1, b_1, n, \eta_1) - I(a_1, b_1, n, \eta)\right] + \left[I(a_2, b_2, n, \infty) - I(a_2, b_2, n, \eta_1)\right], \tag{3.58}$$

$$p_2(\eta) = p_e + \left[I(a_2, b_2, n, \infty) - I(a_2, b_2, n, \eta)\right], \tag{3.59}$$

where $I(a_1, b_1, n, \eta)$, $I(a_1, b_1, n, \eta_1)$ are given by (3.52), and for $\xi = \eta, \eta_1$ [*Gradshteyn and Ryzhik*, 2000]

$$I(a_2, b_2, n, \infty) - I(a_2, b_2, n, \xi) = \int_{\xi}^{\infty} \tau^{-n} \left(a_2 - b_2 \tau^{3-n}\right)^{-n/(n-1)} d\tau = \\ = \frac{(n-1)}{(n+1)(-b_2)^{n/(n-1)}} \xi^{(n+1)/(n-1)} \cdot \\ {}_2F_1\left(\frac{n}{n-1}, \frac{n+1}{(n-1)(3-n)}, \frac{n+1}{(n-1)(3-n)} + 1, \frac{a_2}{b_2 \xi^{3-n}}\right) \tag{3.60}$$

Again in (3.58)-(3.59) the displacement front position η_1 is derived solving (3.56).

When $n = 1$ (a Newtonian fluid displacing another one), the situation is qualitatively analogous to the dilatant case, and a similarity solution exists only for assigned constant injection rate Q_0 at the well. The position of the interface η_1 can be derived, under the assumption $\eta_w \cong 0$, solving the implicit equation

$$\eta_1^2 \exp\left(A\eta_1^2 / 4\right) = \left(Q_0 / (\pi \phi h)\right), \tag{3.61}$$

and the pressure field is given by

$$p_1(\eta) = p_e - \frac{A}{4M}\eta_1^2 \exp\left(\frac{\alpha A \eta_1^2}{4M}\right)\mathrm{Ei}\left(-\frac{\alpha A \eta^2}{4M}\right) + \\ -\frac{A}{4}\eta_1^2\left[\mathrm{Ei}\left(-\frac{A\eta^2}{4}\right) - \mathrm{Ei}\left(-\frac{A\eta_1^2}{4}\right)\right] \tag{3.62}$$

$$p_2(\eta) = p_e - \frac{A}{4M}\eta_1^2 \exp\left(\frac{\alpha A \eta_1^2}{4M}\right)\mathrm{Ei}\left(-\frac{\alpha A \eta^2}{4M}\right), \tag{3.63}$$

where $-\mathrm{Ei}(-\cdot)$ is the exponential integral.

3.3 UNCERTAINTY PROPAGATION AND SENSITIVITY ANALYSIS

In this section the behavior of the responses of interest (i.e. $\zeta(t)$, $\zeta^*(t)$ and the pressure increment in the domain with respect to the ambient value $\Delta p(\eta)$) is discussed as functions of the dimensionless model parameters n, M, α, ϕ and K, (a) by means of a deterministic analysis, and (b) modeling them as stochastic variables and considering the overall effect of their uncertainty.

As far as the deterministic analysis is concerned, $\phi = 0.2$ and $K = 1$ is selected as a reference case; to grasp the influence of relative fluid mobility and compressibility, the following combinations for the mobility and compressibility ratios M and α are considered: I) $M = 0.2$, $\alpha = 0.2$; II) $M = 0.2$, $\alpha = 5$; III) $M = 5$, $\alpha = 0.2$; IV) $M = 5$, $\alpha = 5$.

In Figures 3.2a-c, the interface location ζ is depicted as a function of time for the above combinations and b.c. 1) with $p_w = 1, p_e = 0.1$ ($\Delta p = 0.9$) and $n = 0.50, 0.67, 0.75$ respectively; these values cover quite

well the range of variation of n for pseudoplastic fluids in field cases [*Di Federico et al.*, 2010 and references therein]. Inspection of Figures 3.2a-c reveals that, for given value of flow behavior index n, the interface advances slowly when the displaced fluid is less compressible and less mobile than the displacing one (case I), while it is fastest when the displaced fluid is more compressible and more mobile than the displacing one (case IV). Upon comparing results for different values of n, it is seen that the interface position is an increasing function of flow behavior index. Differences between results at late limes for different values of *n* are more pronounced for case I. This indicates, at least for the range of values of parameters examined here, that the maximum displacement for assigned well pressure is achieved with large values of the power law model exponent *n*, and of the compressibility and mobility ratios α and M.

Figures 3.2d-f show the compression front location ζ^* as a function of time for the same boundary conditions and cases I-IV listed above, respectively for $n = 0.50, 0.67, 0.75$. As expected, the compression front advances fastest when the displaced fluid is more mobile, but less compressible than the displacing one (case III); the compression front is slowest for case II, when the displaced fluid is less mobile and more compressible than the displacing one. The compression front location is an increasing function of flow behavior index; in relative terms, this effect is compounded for cases I and III, when the displaced fluid is less compressible than the displacing one. Upon comparing Figures 3.2d-f with Figures 3.2a-c, it is noted that the compression front location is farther from the interface location when the displaced fluid is less compressible than the displacing one (cases I and III). The above conclusions hold true for all values of flow behavior index, with differences between the two fronts increasing with n.

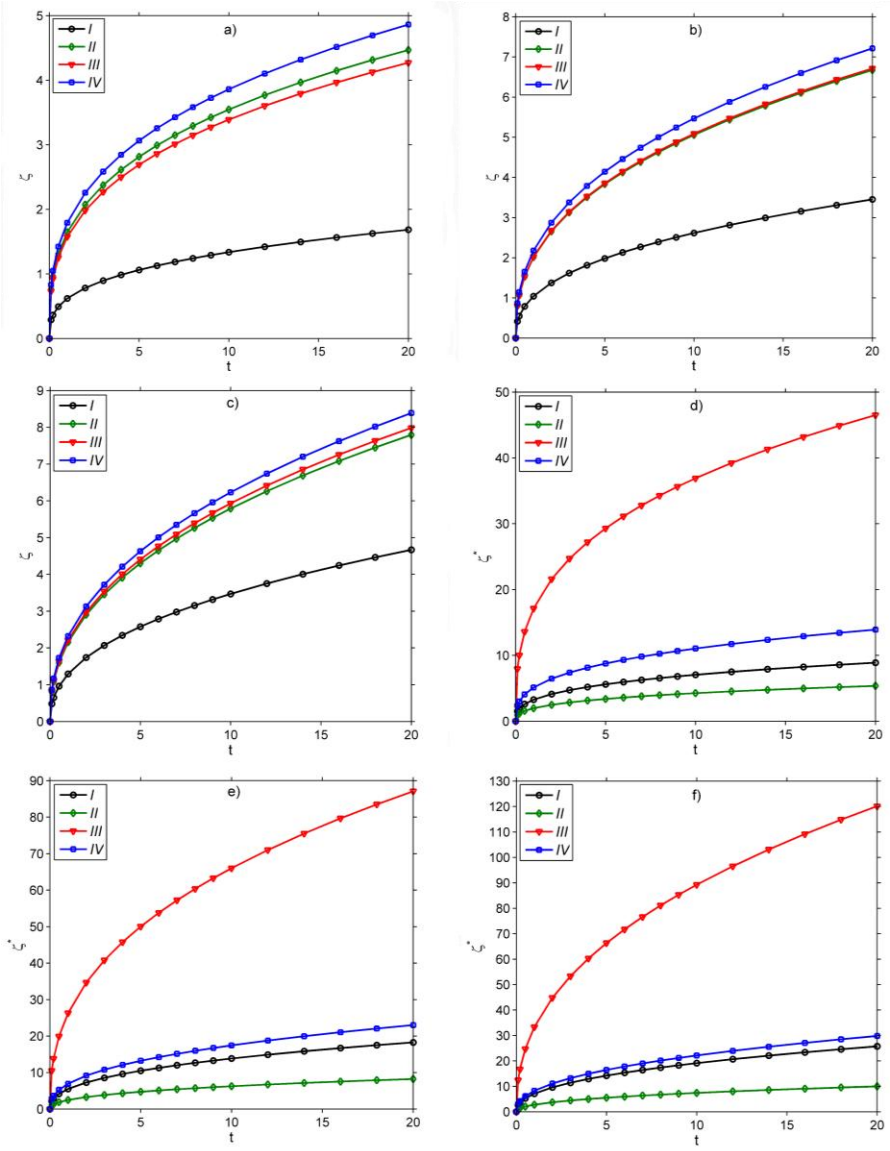

Figure 3.2. a) Front position $\zeta(t)$ for injection at prescribed pressure versus time for $\Delta p = 0.9$, $\phi = 0.2$, $K = 1$, cases I-IV, $n = 0.50$; b) as a) but $n = 0.67$; c) as a) but $n = 0.75$; d) as a) but compression front position $\zeta^*(t)$; e) as d) but $n = 0.67$; f) as d) but $n = 0.75$.

When assigned flux in the origin is considered (i.e. b.c. 2)), the front position at a given time is not a function of mobility and compressibility ratio, but only of flow behavior index; thus Figure 3.3a represents the front advancement over time for b.c. 2) with $h=1$, $Q_0=0.2$ and $n=0.50,0.67,0.75$; note that these values of flow behavior index correspond to injection rates in the origin decreasing with time respectively as $t^{-0.33}, t^{-0.20}, t^{-0.14}$; corresponding results are thus not strictly comparable; the front advances further for larger values of n at late times, while at small times the reverse is true.

Figures 3.3b-d show the compression front location $\zeta^*(t)$ as a function of time for b.c.2) with the same values of Q_0 in the cases I-IV listed above, respectively for $n=0.50,0.67,0.75$. As for b.c. 1), the compression front advances fastest in case III and slowest in case II; cases I and IV yield the same results since the location of the compression front is a function of the ratio between mobility and compressibility ratios. As for b.c. 1), the relative distance between the compression front and the interface location is greatest for case III and smallest for case II. In turn, the distance between the two fronts increases with the value of flow behavior index.

Figures 3.4a-b show for b.c. 1) with $\Delta p=0.9$, $n=0.50$ and case II, the effect of a variation of K and ϕ respectively on the position of the interface; Figures 3.4c-d do the same for the location of the compression front. It is seen that a permeability increase by a factor of ten has a significant effect on the interface and compression front position; less so a variation of porosity in the range 0.15÷0.30.

Finally, Figures 3.5a-b show the behavior of pressure in the displacing and displaced fluids, $p_1(\eta)$ and $p_2(\eta)$, as a function of η for selected cases with $n=0.50$, $M=\alpha=5$ (case IV), $K=1$, $\phi=0.20$; Figure 3.5a does so for b.c. 1) with $p_w=1$ and $p_e=0.1$; Figure 3.5b for b.c. 2) with $h=1$, $p_e=0.1$ and $Q_0=0.2$. In both cases, note the discontinuity in the pressure derivative at the interface location η_1 and the pressure asymptote at the compression front location η^*.

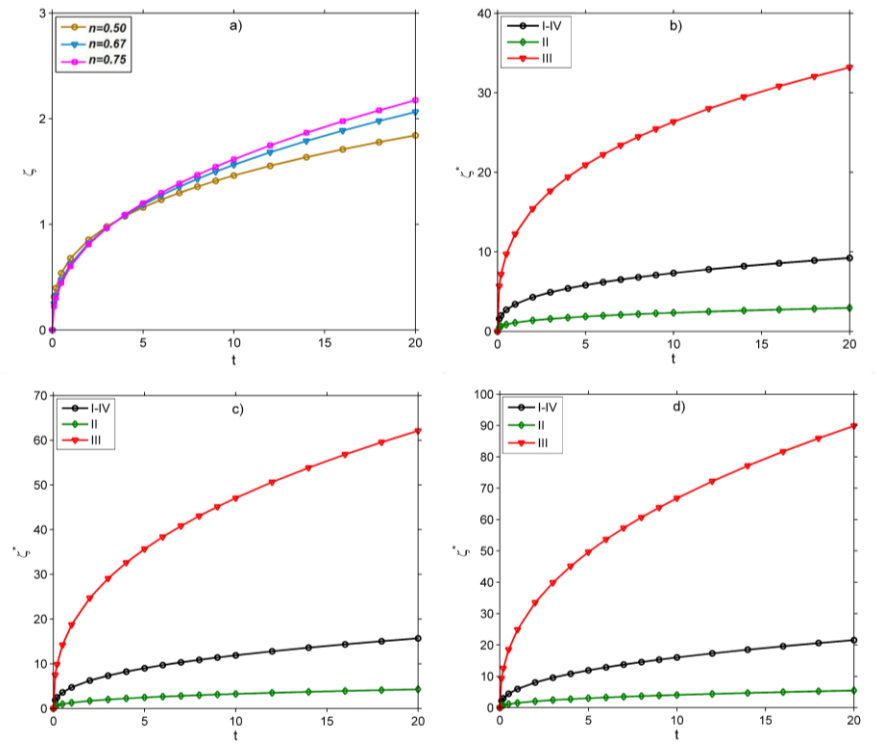

Figure 3.3. a) Front position $\zeta(t)$ for injection at prescribed rate versus time for $Q_0=0.2$, $\phi=0.2$, $K=1$, cases I-IV, and $n=0.50,0.67,0.75$; b) as a) but compression front position $\zeta^*(t)$ and $n=0.50$; c) as b) but $n=0.67$; d) as b) but $n=0.75$.

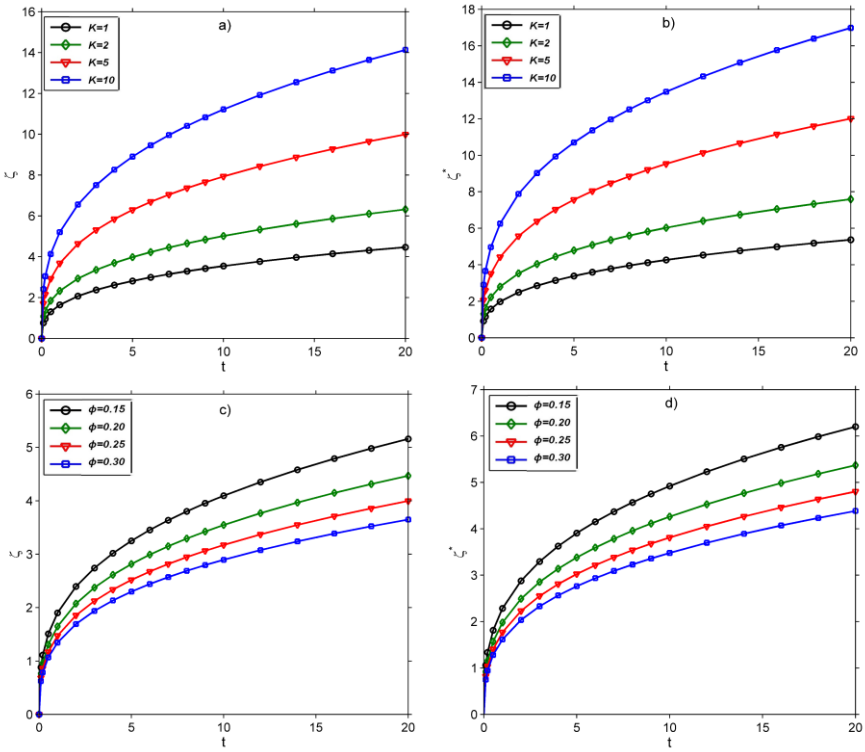

Figure 3.4. a) Front position $\zeta(t)$ for injection at prescribed pressure versus time for $\Delta p = 0.9$, case II, $n = 0.50$, $\phi = 0.2$ and $K = 1,2,5,10$; b) as a) but compression front position $\zeta^*(t)$; c) as a) but $K = 1$ and $\phi = 0.15,0.20,0.25,0.30$; d) as c) but compression front position $\zeta^*(t)$.

In the following the stochastic nature of the parameters involved in the proposed model is considered, representing them as independent random variables to exemplify the approach. This assumption makes the analysis consistent with the previous deterministic one and enables to investigate the salient features of the proposed solution, not affecting the generality of the approach. Furthermore, if the spatial variability of some of the parameters involved has to be investigated for specific characterization purposes, the PCE-based approach can be combined with the Karhunen-

Loeve expansion to represent the stochastic processes in terms of uncorrelated random variables [*Spanos and Ghanem*, 1989; *Ghanem*, 1998].

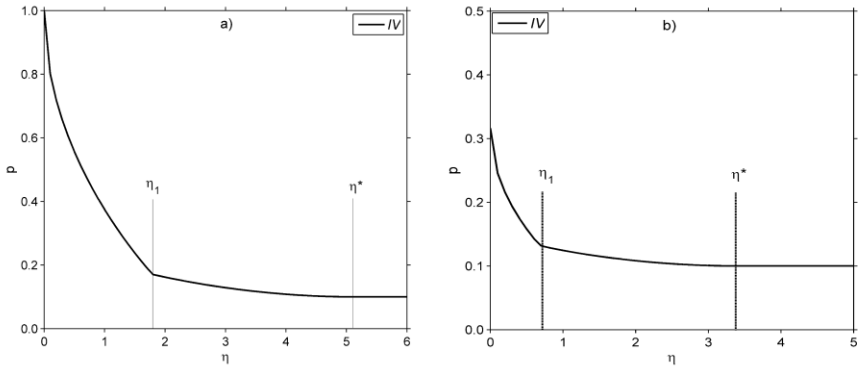

Figure 3.5. Pressure in the domain for injection at prescribed pressure versus similarity variable for $n = 0.50$, $M = \alpha = 5$ (case IV), $K = 1$, $\phi = 0.2$ and a) $p_w = 1$, $p_e = 0.1$; b) $h = 1$, $p_e = 0.1$, $Q_0 = 0.2$.

Random variable	Distribution
n	U(0.40-0.60)
α	U(4-6)
M	U(4-6)
K	U(0.80-1.20)
ϕ	U(0.16-0.24)

Table 3.1. Intervals of variability of the selected uniformly distributed random model parameters

An hypothetical case study (i.e. two specific fluids and a porous domain) is simulated and the way in which the uncertainties associated with the values of the same five parameters influence the model responses is analyzed by means of Global Sensitivity Analysis (GSA) performed

through the Polynomial Chaos Expansion (PCE) technique. Uniform distributions reported in Table 3.1 are considered under a boundary condition of assigned pressure at the well with $p_w = 1$ and $p_e = 0.1$ ($\Delta p = 0.9$).

Figures 3.6a-b depict the mean and associated standard deviation (6a) and the total sensitivity indices (6b) of displacement front position $\zeta(t)$ as a function of time. The uncertainty in the front position is found to increase, as expected, with time, doing so linearly except for very early times; the largest contribution to the total variance at any time is due to medium permeability and porosity in almost equal fashion, while the flow behavior index contributes very little; the variance of flow behavior index, initially the highest, exhibits a non-monotonic behavior; compressibility and mobility ratios do not play a role. The total sensitivity index of permeability and porosity are almost equal and increase from zero to 50% for dimensionless time around 5 and then slightly decreases with increasing time. Correspondingly, the sensitivity to flow behavior index is initially close to 100%, then decreases to almost zero, and again increases with time reaching 10%.

Figure 3.6c-6d do the same as Figures 3.6a-6b for the pressure front position $\zeta^*(t)$. While the variance of pressure front again increases linearly with time, its value is much larger than that associated with the displacement front. The largest contribution to variance is here due by far to flow behavior index, then to porosity and permeability, and lastly to compressibility and mobility ratios. The total sensitivity index of flow behavior index, initially largest, decreases to almost zero for very early times, then increases again reaching 60% at late times. The influence of permeability and porosity is almost equal and increases sharply for very

early times, reaches a peak, then slowly decreases to 10% for late times; the indices of the compressibility and mobility ratios, almost identical between them, exhibit a similar behavior but lower values.

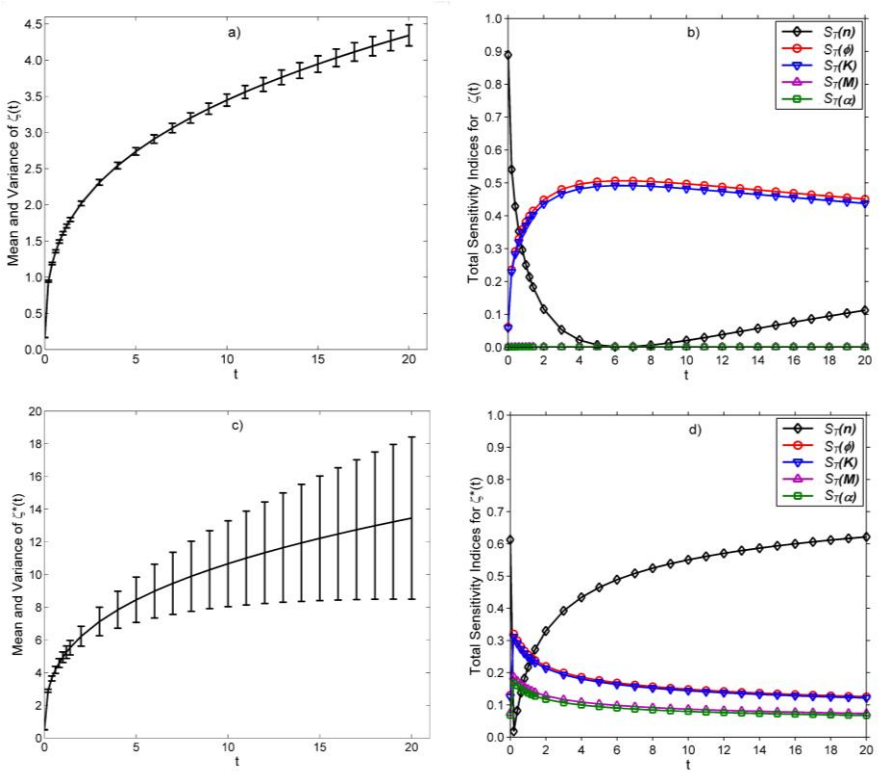

Figure 3.6. a) Front position $\zeta(t)$ versus time and associated uncertainty calculated with the PCE of order p = 2; b) as a) but total sensitivity indices ($S_T(\Omega), \Omega = n, \alpha, M, K, \phi$); c) as a) but calculated for compression front position $\zeta^*(t)$; d) as b) but calculated for compression front position $\zeta^*(t)$.

An analogous analysis (not shown) for intervals of variability of random model parameters smaller (10%) and larger (30%) than those reported in Table 3.1 (20%) reveals a behavior over time of total and partial variances of the two fronts qualitatively similar to that shown in

Figure 3.6, with variance values increasing with increasing variability. Consequently, the behavior of sensitivity indices is remarkably similar to that shown in Figure 3.6.

When the sensitivity to uncertainty of the pressure increment in the domain $\Delta p(\eta) = p(\eta) - p_e$ is examined (not shown), the sensitivity indices exhibit a very irregular behavior, especially near the position of the displacement and pressure fronts; for small values of similarity variables (small radius/large times), the impact of flow behavior index is the largest, while approaching the displacement front the influence of porosity and permeability prevails; between the displacement and pressure fronts, the indices of porosity and permeability remain the highest, while sensitivity to flow behavior index drops to almost zero; the influence of compressibility ratio, and, to a lesser extent, mobility ratio increases approaching the compression front.

Throughout all calculations first order sensitivity indices exhibited insignificant differences from total ones, indicating negligible interaction among different inputs.

3.4 ACCURACY AND EFFICIENCY OF THE APPROACH

The PCE-based approach allows to obtain, through a simple analytical post-processing, all the results presented in the previous section, i.e. when the PCE-surrogate model is available all the information about the variability of the model response is conserved in the set of expansion coefficients, resulting in considerable savings in computational time.

In the selected case study, for each model response of interest, surrogate models are calibrated with the PCE at different orders, resorting to the Legendre Chaos space because the uncertain input parameters are

associated with uniform distributions [*Xiu and Karniadakis*, 2002; *Sudret*, 2008]. Results obtained through the second-order PCE exhibited negligible (or very minor) differences with higher order ones (generally 1-10%); thus only results for order 2 are reported.

The reliability of the results obtained through the PCE-based surrogate model is here analyzed by comparison against a traditional approach in which the sensitivity indices are estimated in a Monte Carlo (MC) framework; this validation step, not shown in previous work on non-Newtonian flows [*Di Federico and Ciriello*, 2012; *Ciriello and Di Federico*, 2012], can be performed examining a considerable number of realizations, since a benchmark analytical solution is available; when a complex numerical model is investigated [*Ciriello et al.*, 2012], the excessive computational cost entails a limited amount of MC simulations. Validation is useful to assess: (a) the quality of the algorithm adopted to obtain the PCE approximation, (b) the applicability of the technique to this specific model, (c) the extent of computational saving. In particular is shown the comparison between the total and partial variances related to the front position $\zeta(t)$ in the selected case $\Delta p = 0.9$. Due to the non-negligible computational cost associated with Monte Carlo simulations (about 7 seconds for each model run, i.e. about 2 hours for 1000 iterations for each time instant, on a standard computer with a 2 GHz processor), the approach is exemplified by considering only four time instants (t = 1, 5, 10, 15) and a fixed value of flow behavior index, $n = 0.50$; this allows using the simpler expressions (A.1) of Appendix A for calculations. Note that this simplification does not affect the following validation approach. The distributions of other random parameters are again uniform with the same mean values of those reported in Table 3.1 and with a selected variability of $\pm 10\%$ around the mean value for each one.

	t	1	5	10	15
MC N_{sim} **= 1000**	V	4.32E-03	1.26E-02	2.05E-02	2.73E-02
	V(ϕ)	2.33E-03	5.52E-03	8.85E-03	1.25E-02
	V(K)	2.14E-03	6.03E-03	8.98E-03	1.43E-02
	V(M)	4.00E-05	3.00E-04	1.18E-03	3.90E-04
	V(α)	4.00E-05	2.80E-04	1.22E-03	4.00E-04
MC N_{sim} **= 5000**	V	4.32E-03	1.29E-02	2.00E-02	2.63E-02
	V(ϕ)	2.04E-03	6.29E-03	1.03E-02	1.33E-02
	V(K)	2.11E-03	6.29E-03	1.04E-02	1.22E-02
	V(M)	5.00E-05	2.60E-04	5.80E-04	3.40E-04
	V(α)	4.00E-05	2.80E-04	5.80E-04	3.70E-04
PCE p **= 2**	V	4.31E-03	1.26E-02	2.00E-02	2.62E-02
	V(ϕ)	2.16E-03	6.31E-03	1.00E-02	1.31E-02
	V(K)	2.14E-03	6.26E-03	9.94E-03	1.30E-02
	V(M)	1.00E-05	2.00E-05	2.00E-05	3.00E-05
	V(α)	1.00E-05	2.00E-05	3.00E-05	4.00E-05

Table 3.2. Comparison between the total variance (V) and partial variances ($V(\Omega), \Omega = \alpha, M, K, \phi$) calculated for the front position $\zeta(t)$ at selected time instants, with the PCE of order p = 2 and with a different number of Monte Carlo iterations (N_{sim} = 1000, 5000).

Table 3.2 reports, for the considered time instants, the total variance of the model response, i.e. $\zeta(t)$, and the partial variances due to the uncertainty on ϕ, K, M and α, calculated with the PCE of order 2 and with a different number of Monte Carlo iterations (N_{sim} = 1000, 5000). It is observed that there is a fine agreement between the variances evaluated via Monte Carlo simulations and those predicted by the PCE, especially when considering the total variance and the partial variances associated with ϕ and K; furthermore the difference between the results of the two methods generally decreases as the number of Monte Carlo iterations increases, even though convergence of Monte Carlo results is not attained. The saving in computational time is crucial as the calibration of the coefficients of the

surrogate model requires only 15 sampling points in the space of the four selected uncertain parameters for each time instant. This advantage is even more important in the complete GSA discussed in the previous section, in which also *n* is considered uncertain. In that case the number of model runs necessary for the calibration are 21 and 116 (respectively for second and third order PCE) and only the PCE method allows to investigate the sensitivity of the presented similarity solution quite continuously in time.

3.5 FINAL REMARKS

A novel analytical solution to non-Newtonian radial displacement of a power-law fluid by another in porous media has been derived in self-similar format under the assumptions of the frontal advance theory. The analysis:

(i) extends to motion of two fluids the analytical approach and results of [*Ciriello and Di Federico*, 2012] on flow of a single power-law fluid, taking compressibility effects into account;

(ii) may be used as a benchmark for complex numerical models;

(iii) allows to investigate the key processes and dimensionless parameters involved in non-Newtonian displacement in porous media.

The PCE-based approach adopted allows to:

(iv) perform a complete Global Sensitivity Analysis of the benchmark solution by considering the uncertainty associated with key dimensionless parameters involved;

(v) derive the variance associated with model outputs with no additional computational cost;

(vi) obtain accurate results when compared with traditional simulations conducted in a MC framework.

Appendix 3A. Closed-form results

The hypergeometric function ${}_2F_1$ in (3.57) reduces to simpler analytical functions if $n = l/(1+l)$ where l is a positive integer. For $l = 1,2,3$, corresponding to $n = 1/2, 2/3, 3/4$, these are respectively [*Gradshteyn and Ryzhik*, 2000]:

$$I(a_i, b_i, 1/2, \tau) = 2a_i \tau^{1/2} - b_i \tau^3 / 3, \tag{A.3.1}$$

$$I(a_i, b_i, 2/3, \tau) = 3a_i^2 \tau^{1/3} - 3a_i b_i \tau^{8/3} / 4 + b_i \tau^5 / 5, \tag{A.3.2}$$

$$I(a_i, b_i, 3/4, \tau) = 4a_i^3 \tau^{1/4} - 6a_i^2 b_i \tau^{5/2} / 5 + 12 a_i b_i^2 \tau^{19/4} / 19 - b_i^3 \tau^7 / 7 . \tag{A.3.3}$$

4. Application to a high-complexity numerical model

SOMMARIO

In questo capitolo, il codice numerico sviluppato e presentato nelle precedenti sezioni viene applicato ad un modello numerico di elevata complessità rendendo possibile lo sviluppo di indagini approfondite ed accurate, non perseguibili attraverso metodi di simulazione tradizionali a causa dell'elevato onere computazionale. In particolare, l'utilizzo combinato delle tecniche di Analisi di Sensitività Globale e di espansione in Caos Polinomiale è adottato in riferimento ad un modello di trasporto di contaminanti per la valutazione del livello raggiunto dalla concentrazione di radionuclidi in corrispondenza di un assegnato punto di controllo in un acquifero eterogeneo. La migrazione di radionuclidi nel mezzo poroso è conseguente al rilascio degli stessi da un deposito sub-superficiale di scorie radioattive. La conduttività idraulica dell'acquifero è modellata come un processo stocastico stazionario nello spazio. L'incertezza caratterizzante i primi due momenti statistici della concentrazione di picco dei radionuclidi al punto di controllo è esaminata come conseguenza di una parziale conoscenza (a) dei parametri del variogramma della conduttività idraulica, (b) del coefficiente di ripartizione associato al radionuclide, e (c) della dispersività idrodinamica alla scala di interesse. Queste quantità sono trattate come variabili stocastiche. Un'Analisi di Sensitività Globale della risposta del sistema è quindi svolta in un contesto numerico di tipo Monte

Carlo, basato su di un processo di campionamento nello spazio dei parametri ritenuti incerti. Gli indici di Sobol sono adottati come misura di sensitività allo scopo di fornire una stima dell'influenza dei parametri incerti sui momenti statistici della concentrazione di picco di contaminante. Il calcolo degli indici è sviluppato impiegando la tecnica dell'espansione in Caos Polinomiale. Si dimostra che la metodologia proposta consente di estendere il numero di simulazioni Monte Carlo fino ad ottenere la convergenza dei momenti della concentrazione di picco, a fronte di un notevole risparmio computazionale e mantenendo un'accuratezza apprezzabile. L'applicazione della tecnica dell'espansione in Caos Polinomiale ad un modello di complessità pari a quello esaminato rappresenta un possibile nuovo approccio per la caratterizzazione dell'incertezza legata alle previsioni modellistiche e la conseguente gestione ottimale di sistemi articolati. Lo studio presentato in questo capitolo è incluso in *Ciriello et al.* [2012].

4.1 RADIONUCLIDE MIGRATION IN THE GROUNDWATER ENVIRONMENT

Performance assessment of radioactive waste repositories aims at evaluating the risk of groundwater contamination due to potential release of radionuclides. Modeling the whole chain of processes involved in this analysis is extremely challenging and requires complex theoretical and numerical models to couple radionuclide migration within the repository and in the groundwater environment. Uncertainty associated with, e.g., incomplete knowledge of initial and boundary conditions, nature and structure of the groundwater system and related key parameters is to be added to the list of difficulties [e.g., *Tartakovsky*, 2007; *Winter*, 2010; *Volkova et al*., 2008 and references therein].

The analysis of the uncertainty associated with the first two (statistical) moments of the peak solute concentration, detected at a given location, is considered in this Chapter. The source of uncertainty is the incomplete/imprecise knowledge of the values of a set of hydrogeological parameters characterizing the system [*Rubin*, 2003; *Zhang*, 2002].

The Polynomial Chaos Expansion (PCE) technique is adopted to analyze the uncertainty affecting the outputs of a numerical model of radionuclide migration in an aquifer, following a release from a near surface repository. The outflow from the repository is modeled within the Monte Carlo (MC) framework proposed by *Cadini et al*. [2012]. Radionuclide migration in the aquifer is modeled through an Advection-Dispersion-Reaction-Equation (ADRE). The aquifer hydraulic conductivity constitutes a (second-order stationary) randomly heterogeneous field. The model outputs of interest are the first two (statistical) moments (i.e., mean and variance) of the peak concentration at a given control location in the

aquifer. The focus of the study is the investigation of the way incomplete/imprecise knowledge of (a) the correlation scale, λ, of the variogram of the log-conductivity field, (b) the partition coefficient associated with the migrating radionuclide, k_d, and (c) the longitudinal dispersivity at the scale of interest, α_L, propagates to the selected (ensemble) moments of the output distribution.

Global Sensitivity Analysis (GSA) is performed jointly with PCE to compute the Sobol indices associated with the three selected uncertain parameters (λ, k_d, α_L). The latter are treated as independent random variables. The PCE-based surrogate model which is derived is then employed to perform an exhaustive set of MC simulations to analyze the target moments of interest.

4.2 NUMERICAL MODEL OF MIGRATION IN A RANDOMLY HETEROGENEOUS AQUIFER

The approach is exemplified by considering an environmental problem related to the performance assessment of a radioactive waste repository. A MC-based simulation technique is employed to describe radionuclide release at the repository scale. This model of release of radionuclides, i.e., ^{239}Pu, from the repository is linked to a groundwater flow and transport numerical model to simulate radionuclide migration within a heterogeneous aquifer.

The aquifer hydraulic conductivity is modeled as a second-order stationary stochastic process in space. The first two (statistical) moments (i.e., mean and variance) of the peak concentration, detected at a given control location in the aquifer, are considered as the target model responses. As mentioned in Section 4.1, uncertainty associated with these

quantities is considered to be a consequence of incomplete knowledge of (a) the correlation scale of the variogram of the log-conductivity field (b) the partition coefficient associated with the migrating radionuclide, and (c) the dispersivity associated with the spreading of the reactive solute plume at the scale of observation.

4.2.1 Repository representation and modeling of release history

The conceptual repository design considered in the performance assessment illustrated in this study has been proposed by ENEA [*Marseguerra et al*., 2001a, b] and has similarities with the currently operative disposal facility of El Cabril in Spain [*Zuolaga*, 2006].

Following *Cadini et al*. [2012], the repository is modelled as a one-dimensional (along the vertical direction) system. The major containment structures of the disposal facility are the waste packages, the modules or containers, the cells and the disposal units. A typical waste package consists in a steel drum containing the radioactive waste and immobilized in a concrete matrix. The geometrical setting of the waste packages, modules and disposal units is taken from *Cadini et al*. [2012].

In agreement with typical engineering scenarios, it is considered that [*Marseguerra et al*. 2001a, b]: (i) the modules are identical; (ii) the mass transport occurs chiefly along the vertical direction; and (iii) lateral diffusive spreading is symmetric. Radionuclides transition across the compartments is described stochastically. Under the assumption that solute displacement can be modeled as a Markovian process, the transition rates can be identified from the classical advection/dispersion equation. Non-Fickian transport could also be included according to existing conceptual schemes [*Berkowitz et al*. 2006 and references therein] where the relevant

transport parameters can be estimated by detailed data analysis at the temporal and spatial scales at which the processes of interest occur.

For the purpose of this example, the numerical code MASCOT [*Marseguerra and Zio*, 2001; *Marseguerra et al*., 2003; *Cadini et al*., 2012] is adopted to compute the probability density function of the release of ^{239}Pu from the modules. Details of the initial and boundary conditions, computations and the resulting temporal dynamics of the radionuclide release history are illustrated in *Cadini et al*. [2012].

4.2.2 Radionuclide migration in the groundwater system

For simplicity and for the purpose of illustrating the methodology, radionuclide transfer time within the partially saturated zone is disregarded and only contaminant residence time within the fully saturated medium is analyzed. This assumption may be regarded as conservative because it tends to overestimate the radionuclide concentration detected downstream of the repository. This can also be considered as a viable working assumption in the presence of shallow reservoirs. The effect of processes occurring within the partially saturated region may require an additional ad-hoc analysis, which is outside the scope of this work and does not alter the methodological framework of the work.

Groundwater flow and contaminant transport are modeled within a two-dimensional system. As mentioned earlier, the (natural) log-transformed hydraulic conductivity, $Y(\mathbf{x})$ ($\mathbf{x}$ denoting the space coordinate vector), is modeled as a second-order stationary spatial random function. For this example, the parameters of the variogram of Y have been selected as representative of a field case study. The latter is not specifically reported for confidentiality reasons. However, note that the particular choice of

these values does not affect the generality of the methodology. Log-conductivity is characterized by an isotropic variogram of the exponential type, with sill $\sigma^2 = 1.21$. For the purpose of this illustrative example, the variogram sill is fixed and its correlation scale is considered as an uncertain parameter because of its poor identifiability due to typical horizontal spacing of available field-scale measuring locations. MC realizations of $Y(\mathbf{x})$ have been generated by employing the sequential Gaussian scheme implemented in the code GCOSIM3D [*Gómez-Hernández and Journel*, 1993].

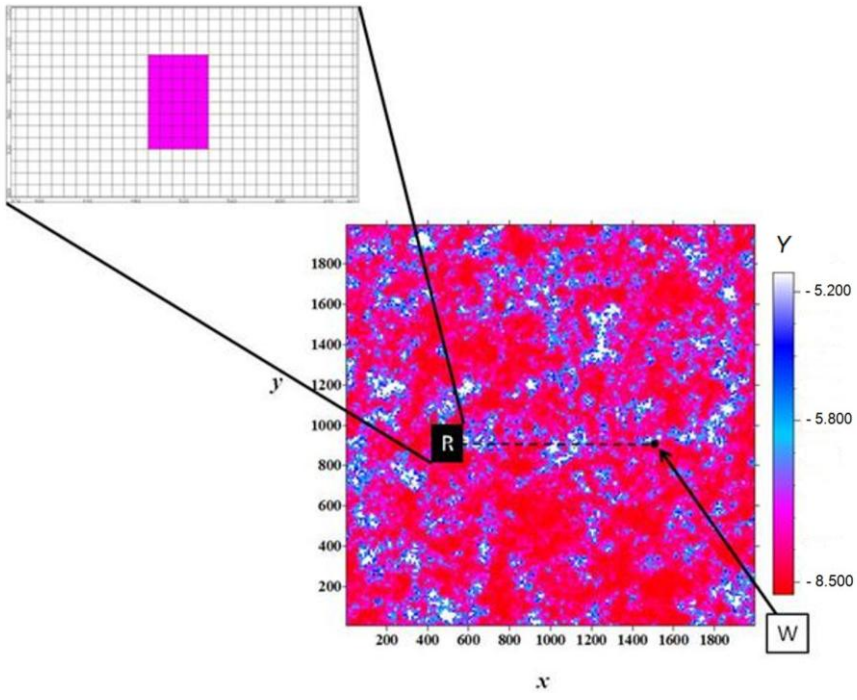

Figure 4.1. Sketch of the adopted two-dimensional groundwater flow domain, including the repository projection (R) and the selected control point (W), for a selected realization of the log-conductivity field.

A two-dimensional domain of uniform lateral side equal to 2000 m is considered. As an example, a selected realization of the log-conductivity distribution is depicted in Figure 4.1 together with the repository projection (R), with sides equal to 50 m and 80 m, and the target control point (W), located 960 m downstream of the repository fence line.

The domain is discretized into square cells with uniform side of 10 m, ensuring that there are at least four log-conductivity generation points per correlation scale. Each of the 8 × 5 cells located under the repository projection area receives the release of a cluster of 4 × 3 columns of 5 modules [see also *Cadini et al.* 2012]. These cells are modeled through a recharge boundary condition so that a time-dependent influx solute mass is injected in the porous medium according to a suitable discretization in time of the calculated outflow from the repository. As in *Cadini et al.* [2012], the incoming water flow [m^3/y] from the repository is set at a constant value equal to $\Phi_{in} = q_d S,\ \ q_d = 21.2$ [m/y] being the water Darcy flux at the bottom of the 5 modules column and S [m^2] being the area of the source cells. The associated radionuclide concentration [Bq/m^3] released to the aquifer is then:

$$C_{in}(t) = A_0\ pdf_{out}(t)/\Phi_{in} \tag{4.1}$$

where A_0 = 1.6 × 106 [Bq] is the total activity of ^{239}Pu (which is assumed to be uniformly distributed) in the repository at a reference time t = 0 and $pdf_{out}(t)$ [y^{-1}] is the release probability density function from the repository. The adopted ^{239}Pu activity level corresponds to the Italian inventory [Enea, 2000] and justifies the assumption of disregarding solubility-limited release.

In the example presented, the concentration of $^{239}\mathrm{Pu}$ within the repository is $C_{rep}^{Pu239} \cong \lambda_r A_0 / N_A V_{rep} = 2.96 \cdot 10^{-14} < C_{sl}^{Pu239} = 2.30 \cdot 10^{-4}$ [mol/m^3], $\lambda_r = 0.28761 \times 10^{-4}$ [y^{-1}] being the $^{239}\mathrm{Pu}$ constant decay, N_A the Avogadro constant, while V_{rep} is the total volume of the repository and C_{sl}^{Pu239} is the solubility limit of $^{239}\mathrm{Pu}$. Additional details are presented in *Cadini et al*. [2012].

Base groundwater flow in the aquifer is driven by a constant hydraulic head drop between the East and West boundaries, resulting in a unit average head gradient. No-flow conditions are assigned to the North and South boundaries.

Simulations of the steady state flow problem for each log-conductivity realization are performed with the widely used and tested finite difference code MODFLOW2000 [*McDonald and Harbaugh*, 1988]. Radionuclide migration in the groundwater system is then modeled through the classical Advection-Dispersion-Reaction Equation (ADRE), where the partition coefficient, k_d, governing sorption of the contaminant onto the host solid matrix and the longitudinal dispersivity, α_L (for simplicity, transverse dispersivity is assumed to be equal to 0.1 α_L), are considered to be random variables. A uniform effective porosity of 0.15 is considered.

4.3 GSA AND VALIDATION

The three random parameters selected are assumed to be uniformly distributed within the intervals reported in Table 4.1. The degree of variability of k_d has been selected according to ENEA [1997] and *Nair and Krishnamoorthy* [1999]. The range of variability of λ is compatible

with the selected domain dimension and grid size Δ, and consistent with the typical scarcity of a sufficiently large number of closely spaced *Y* measuring points. It is also consistent with the adopted two-dimensional setting which relies on local scale transmissivities deriving from vertical integration of conductivity values [see, e.g., *Neuman et al*., 2007 and references therein for a distinction between local and regional transmissivities].

With reference to the dispersivity parameter, the recent theoretical analysis of *Porta et al*. [2012] shows that modeling transport problems associated with fast, homogeneous chemical reactions via a continuum-scale model with the same format of an ADRE should entail considering a dispersion coefficient which depends on reactive rather than conservative transport features. In this context, it is observed that there are still no conclusive and unifying theoretical findings relating dispersivities to different heterogeneity (and numerical resolution) scales to capture the peak concentration behavior within a reactive flow system at the field scale. For the purpose of this illustrative example, a simplified approach is followed and the simulations are confined within the sampling space α_L = 5-7 Δ. Note that the dispersivity values adopted are larger than those stemming from first-order theories based on non-reactive transport [*Rubin et al*., 1999]. They allow considering enhanced dispersion values which are comprised within the range of variability of apparent longitudinal dispersitivities that have been estimated from a set of field tracer studies worldwide, including estimates obtained from the calibration of numerical models against hydraulic and concentration data for large-scale plumes in heterogeneous media [see, e.g., *Neuman*, 1990, and *Neuman and Di Federico*, 2003 and references therein].

Random Variable	Distribution
Partition Coefficient, k_d	$U\left(1\frac{l}{g};3\frac{l}{g}\right)$
Longitudinal Dispersivity, α_L	$U(50m;70m)$
Correlation length of log-conductivity, λ	$U(40m;100m)$

Table 4.1. Intervals of variability of the selected uniformly distributed random model parameters.

The model response, i.e., the radionuclide peak concentration, c_p, at the control point and its statistical moments are then, in turn, random. As introduced before, we perform the analysis in a numerical MC framework according to the following steps: (a) a set of $N_f = 100$ fields of Y are generated by GCOSIM for given values of the random parameters sampled within the intervals presented in Table 4.1; (b) groundwater flow and transport are solved and (sample) mean, $\langle c_p \rangle$, and standard deviation, σ_{c_p}, of the peak concentration are computed; (c) steps (a) and (b) are repeated for different sampling points in the random parameters space; and (d) GSA is performed to discriminate the relative contribution of the random parameters to uncertainty of $\langle c_p \rangle$ and σ_{c_p}. Note that due to the random nature of $Y(\mathbf{x})$, GSA is performed on the (sample) moments of c_p rather than on its actual value calculated at the selected control location for each random realization. Conceptually, this is equivalent to performing a GSA of the results stemming from the solution of transport equations satisfied by the (ensemble) moments of the evolving concentrations [e.g., *Guadagnini and Neuman*, 2001 and *Morales-Casique et al*., 2006 a,b for conservative solutes].

The procedure illustrated is rather cumbersome when considering the solution of the full system model, because of the large number of simulations required, so that a GSA might become impractical. Therefore, the PCE technique is adopted and expansions of order p = 2, 3 and 4 are derived for both $\langle c_p \rangle$ and σ_{c_p}. The Legendre Chaos space is considered, because the uncertain input parameters are associated with uniform distributions.

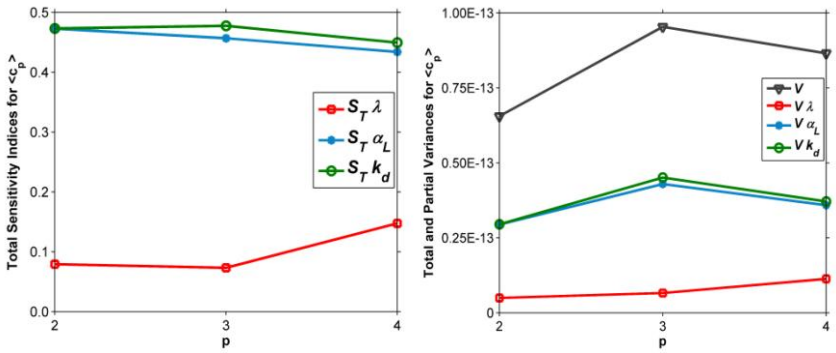

Figure 4.2. Total Sensitivity Indices, S_T (Ω); $\Omega = \lambda$, α_L , k_d , Total Variance, V , and Partial Variances, V (Ω); $\Omega = \lambda$, α_L , k_d , calculated for $\langle c_p \rangle$ and p = 2, 3, 4.

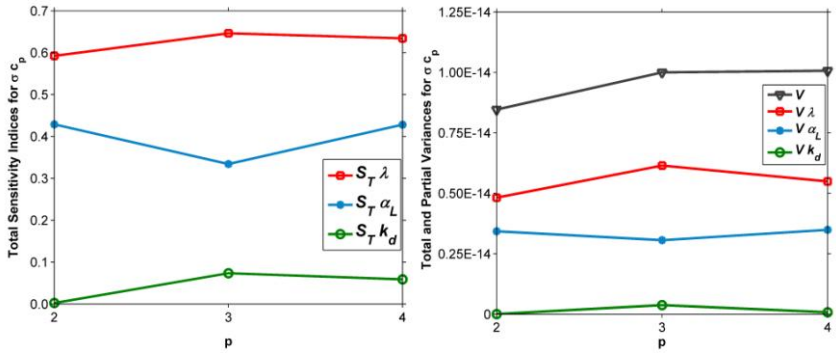

Figure 4.3. Total Sensitivity Indices, S_T (Ω); $\Omega = \lambda$, α_L , k_d , Total Variance, V , and Partial Variances, V (Ω); $\Omega = \lambda$, α_L , k_d , calculated for σ_{c_p} and p = 2, 3, 4.

The calibration of the coefficients of the surrogate models requires $N_R = 10$, 38 and 78 (respectively for p = 2, 3, 4) sampling points in the space of the three selected uncertain parameters. In this example, this corresponds to $N_{MC} = 1000$, 3800, 7800 runs of the full model of groundwater flow and transport. Calculation of the Sobol indices is then performed with negligible additional computational requirements.

Figure 4.2 reports the dependence of the Total Sensitivity Indices, S_T (left), and variances, V (right), of $\langle c_p \rangle$ on the degree of polynomial expansion, p. Figure 4.3 reports the corresponding results for σ_{c_p}. Note that S_T and V are not dramatically influenced by the degree of polynomial expansion selected for both moments. The good agreement obtained between Total and Principal Sensitivity Indices (not shown) implies that the effects of parameter interactions can be neglected in this example. Figure 4.2 reveals that k_d and α_L are the parameters which are most influential to $\langle c_p \rangle$, regardless of the degree of expansion adopted and for the selected uncertainty intervals in the parameter space. On the other hand, the log-conductivity correlation scale, λ, and (to a lesser degree) the dispersivity, α_L, strongly influence σ_{c_p}, while k_d does not have a significant impact for the specific values adopted in the case study. The uncertainty associated with the mean peak concentration is thus related mostly to the spatial structure of heterogeneity and to the strength of the dispersion phenomena, and less to the considered geochemical scenario.

A corresponding investigation performed on the travel time of c_p yields a sensitivity index close to one (not shown) for k_d, revealing that

the partition coefficient governs the time of arrival of the peak concentration to the control point in the selected case study.

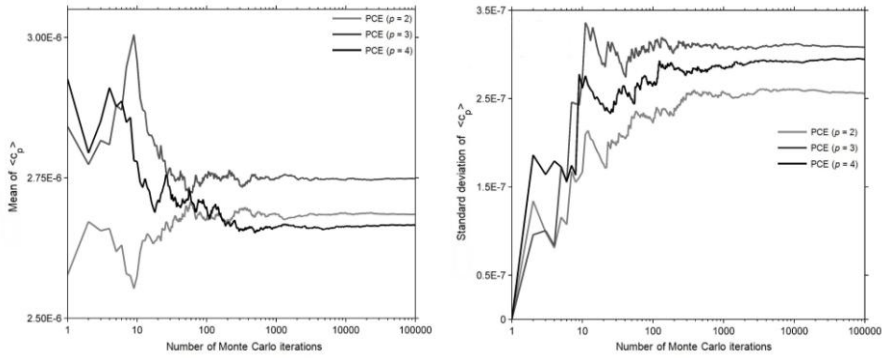

Figure 4.4. Dependence of the (a) mean and (b) standard deviation of $\langle c_p \rangle$ on the number of Monte Carlo iterations performed with the calibrated surrogate models.

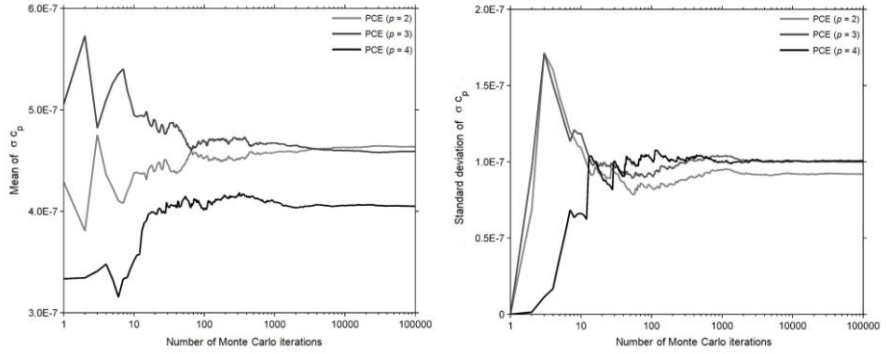

Figure 4.5. Dependence of the (a) mean and (b) standard deviation of σ_{c_p} on the number of Monte Carlo iterations performed with the calibrated surrogate models.

The calibrated surrogate models allow extending with negligible computational cost the number of MC simulation runs which can then be considered to compute the mean and standard deviation of $\langle c_p \rangle$ and σ_{c_p}. Figures 4.4 and 4.5 respectively depict the dependence of these quantities

on the number of MC runs performed with the calibrated surrogate models. Even as the values of mean and standard deviation of $\langle c_p \rangle$ and σ_{c_p} are analytical counterparts of the corresponding surrogate models, this kind of analysis enables one to identify the number of simulations required to attain convergence of the sample moments for the selected case study ($\approx 10^4$). Therefore, this procedure is useful to address the complexity of the case study and supports the adoption of a surrogate model to assess the uncertainty associated with the model response at reasonable computational costs. It also allows to develop the subsequent risk analysis through the computation of the complete *CDFs* associated with the statistical target moments in a MC framework with the calibrated surrogate models.

The reliability of the results obtained through the PCE-based surrogate model has been analyzed by comparison against a number of full model runs performed by uniform sampling of N_s = 100 points in the random parameters space, corresponding to a total of 10^4 random realizations of $Y(\mathbf{x})$. The limited amount of sampling points selected is due to the excessive computational cost associated with the full model run (about 4 min for each simulation on a standard computer with a 3.16 GHz processor).

Figure 4.6 reports the relative fraction, $\mathcal{F}$ (%), of the mean concentration values, $\langle c_p \rangle_l^{SM}$ (l = 1, 2, …, N_s), calculated with the PCE at different orders (p = 2, 3, 4) and comprised within intervals of width $w = \pm \left(\sigma_{c_p}^{FM}\right)_l$, $\pm 2\left(\sigma_{c_p}^{FM}\right)_l$, and $\pm 3 \left(\sigma_{c_p}^{FM}\right)_l$ centered around $\langle c_p \rangle_l^{FM}$, $\langle c_p \rangle_l^{FM}$ and $\left(\sigma_{c_p}^{FM}\right)_l$ respectively being the mean and standard deviation of the peak

concentration computed by means of the full system model. As previously indicated, the latter is based on a standard MC solution of radionuclide migration within *NMC* = 100 log-conductivity realizations for each $1 \le l \le N_s$.

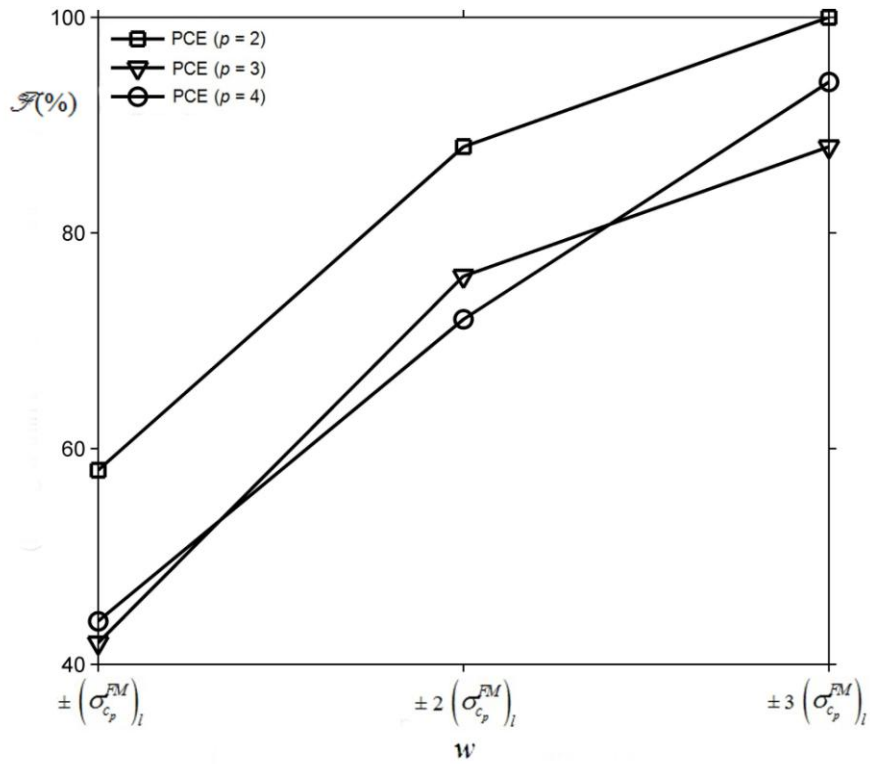

Figure 4.6. Relative fraction, F (%), of the mean concentration values, $\left\langle c_p \right\rangle_l^{SM}$ (l = 1, 2, …, N_s) calculated with the PCE at different orders (p = 2, 3, 4) which are comprised within intervals of width $w = \pm \left(\sigma_{c_p}^{FM}\right)_l$, $\pm 2 \left(\sigma_{c_p}^{FM}\right)_l$, and $\pm 3 \left(\sigma_{c_p}^{FM}\right)_l$ centered around $\left\langle c_p \right\rangle_l^{FM}$; $\left\langle c_p \right\rangle_l^{FM}$ and $\left(\sigma_{c_p}^{FM}\right)_l$ respectively are the mean and standard deviation of the peak concentration computed through the full system model on the basis of a standard Monte Carlo analysis of radionuclide migration within *NMC* = 100 log-conductivity realizations for each l.

It can be seen that at least 40% of the values calculated with the surrogate models of different order are comprised within the intervals of width $\pm \sigma_{c_p}^{FM}$, while about 75% of the results are included within intervals not exceeding $\pm 2\sigma_{c_p}^{FM}$. According to this criterion, Figure 4.6 suggests that in our example the best results appear to be provided by the PCE of order $p = 2$.

Model	**Mean of $\langle c_p \rangle$**	**Standard Deviation of $\langle c_p \rangle$**
Full system model	2.738E-06	3.241E-07
Surrogate model $p = 2$	2.407E-06	7.175E-08
Surrogate model $p = 3$	3.190E-06	1.887E-07
Surrogate model $p = 4$	2.538E-06	3.462E-07

Table 4.2. Values of the mean and standard deviation of $\langle c_p \rangle$ calculated with the full model and the surrogate models on the basis of 100 sampling points in the random parameter space.

Model	**Mean of σ_{c_p}**	**Standard Deviation of σ_{c_p}**
Full system model	4.061E-07	8.169E-08
Surrogate model $p = 2$	4.708E-07	3.310E-08
Surrogate model $p = 3$	4.278E-07	5.719E-08
Surrogate model $p = 4$	4.530E-07	1.321E-07

Table 4.3. Values of the mean and standard deviation of σ_{c_p} calculated with the full system model and the surrogate models on the basis of 100 sampling points in the random parameter space.

To complement these results, Table 4.2 reports the mean and standard deviation of $\langle c_p \rangle$ calculated on the basis of the N_s =100 sampling points in

the random parameter space for each model (standard MC and surrogate models of different order). Table 4.3 reports the corresponding results for σ_{c_p}. The limited number of simulations does not allow to attain complete convergence of the target moments. However, it is possible to observe that the PCE of order p = 4 provides the best approximation of both the mean and standard deviation of $\langle c_p \rangle$ calculated with the full model. In other words, the Total Sensitivity Indices for $\langle c_p \rangle$ calculated with the PCE of order p = 4 are candidates to provide the best indications for a GSA, as one might expect. Finally, it can be noted that the PCE of order p = 3 best approximates the mean and standard deviation of σ_{c_p} calculated with the full model on the basis of the simulations performed.

4.4 RISK ANALYSIS

On the basis of the results reported in Section 4.3 the analysis then considers the computation of the complete *CDFs* associated with $\langle c_p \rangle$ and σ_{c_p}. This is done in a MC framework upon relying on the calibrated surrogate models because the computational cost associated with the original full model is unaffordable. The number of MC simulations performed is equal to 10^4, which leads to convergence of the first two moments of $\langle c_p \rangle$ and σ_{c_p}, as suggested by the results of Section 4.3.

Figures 4.7 and 4.8 depict the calculated *CDFs* of $\langle c_p \rangle$ and σ_{c_p}, respectively.

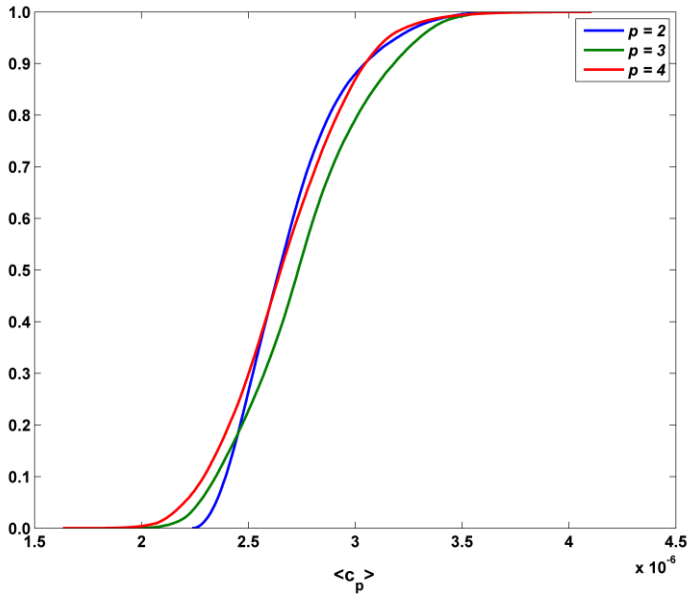

Figure 4.7. CDF of $\langle c_p \rangle$ computed with 10^4 MC simulations with the available surrogate models.

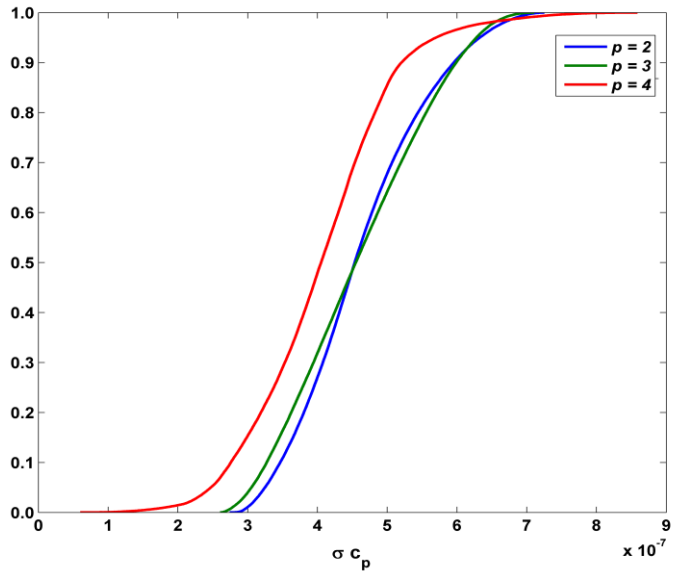

Figure 4.8. CDF of σ_{c_p} computed with 10^4 MC simulations with the available surrogate models.

The computation of the entire distributions of the key-system variables is crucial in several fields of engineering, and especially referring to groundwater contamination problems and human health impacts due to possible radionuclide ingestion.

4.5 FINAL REMARKS

This chapter is devoted to the presentation of an approach to perform a Global Sensitivity Analysis (GSA) of a high-complexity theoretical and numerical model descriptive of the potential release of radionuclides from a near surface radioactive waste repository and the subsequent contaminant migration in a groundwater system. Uncertainty stems from incomplete knowledge of the variogram and transport parameters (i.e., the correlation length of the variogram of log-conductivity, the partition coefficient associated with the migrating radionuclide and the dispersivity at the scale of interest) and from the random nature of the hydraulic conductivity field. The target system responses are the first two (ensemble) moments of the peak concentration at a given control point. GSA has been performed through the Polynomial Chaos Expansion (PCE) technique, leading to the following key results: (a) the analysis of the Sobol indices has revealed that the (sample) mean of the peak concentration is strongly influenced by the uncertainty in the partition coefficient and the longitudinal dispersivity, and the effects of these parameters shadow the impact of the spatial coherence of the log-conductivity field at the scale analyzed and for the selected space of parameter variability; (b) on the other hand, the log-conductivity correlation scale is the most influential factor affecting the uncertainty of the standard deviation of the peak concentration in this example; and (c) the PCE surrogate models allow extending, with negligible computational

cost and acceptable accuracy, the number of MC iterations and attain convergence of the selected target moments.

The results support the relevance of adopting the proposed model reduction technique for complex numerical models. This methodology allows performing in-depth analyses which would be otherwise unfeasible, thus severely limiting the capability to represent the relevant processes involved in a target environmental scenario.

5. Sensitivity-based strategy for model calibration

SOMMARIO

In questo capitolo, gli strumenti sviluppati e presentati nelle precedenti sezioni, vengono utilizzati nel contesto di problemi di tipo inverso quale la calibrazione dei parametri. Una nuova strategia generale basata sull'Analisi di Sensitività Globale e sui criteri di discriminazione dei modelli viene introdotta ed impiegata per (a) calibrare i parametri chiave di alcuni modelli impiegati per l'interpretazione di esperimenti di trasporto di traccianti a scala di laboratorio, (b) classificare tali modelli e (c) stimarne il grado relativo di verosimiglianza attraverso il calcolo della probabilità a posteriori. Per l'applicazione di tale metodologia si fa riferimento all'esperimento di trasporto conservativo condotto in un mezzo poroso uniforme presentato da *Gramling et al.* [2002]. L'Analisi di Sensitività Globale è condotta su tre modelli di trasporto: (a) la classica equazione di advezione-dispersione, (b) una formulazione a doppia porosità con trasferimento di massa fra regioni a diversa mobilità, e (c) l'approccio del *Continuous Time Random Walk*. Per lo sviluppo dell'Analisi di Sensitività Globale si ricorre all'utilizzo della tecnica dell'espansione in Caos Polinomiale applicata alle equazioni governanti dei tre modelli selezionati, schematizzandone i parametri chiave come variabili aleatorie indipendenti. I risultati ottenuti mostrano che l'approccio proposto consente di identificare (a) l'importanza relativa dei parametri da cui dipende la

risposta di ciascun modello, (b) le coordinate spazio-temporali in cui la risposta di ciascun modello risente maggiormente dell'indeterminatezza dei rispettivi parametri. L'Analisi di Sensitività Globale è conseguentemente impiegata per la stima dei parametri dei modelli, condotta secondo il criterio di massima verosimiglianza e sviluppata sulla base di sottoinsiemi di osservazioni corrispondenti alle coordinate spazio-temporali in cui la risposta di ogni modello risulta maggiormente sensibile. Infine, l'impiego di criteri di identificazione dei modelli consente di (a) classificare i modelli di trasporto selezionati rispetto all'esperimento a cui ci si riferisce in questo studio, (b) associare a ciascun modello una probabilità a posteriori per ogni sottoinsieme di osservazioni individuato per la stima dei parametri. La calibrazione basata sull'Analisi di Sensitività Globale è in grado di restituire un'approssimazione sufficientemente accurata dell'intero insieme di dati sperimentali, pur essendo sviluppata a partire da sottoinsiemi di dimensione minima costituiti dalle osservazioni a cui la risposta di ciascun modello è più sensibile. La metodologia proposta è del tutto generale ed estendibile a differenti contesti e casi applicativi. Il lavoro presentato in questo capitolo è incluso in *Ciriello et. al* [2013] attualmente in fase di revisione su *Water Resources Research*.

5.1 INTERPRETATION OF TRANSPORT EXPERIMENTS IN LABORATORY-SCALE POROUS MEDIA

Selection of an appropriate quantitative model and associated parameter calibration are key issues in the interpretation of transport experiments in natural and reconstructed porous media. The assessment of model sensitivity to parameter uncertainty and comparison amongst different models on the basis of model selection criteria are at the core of an appropriate methodology to address this problem. Key sources of uncertainty associated with modeling of processes governing conservative transport in porous media at different scales of observations include hydraulic and transport parameters (e.g., hydraulic conductivity, porosity, and dispersivity) and boundary conditions (e.g., the concentration at the source location or the fluid flow rate). Sensitivity of a model response to these parameters typically varies in space and time. An important step of a parameter estimation procedure is to identify locations in the system where the model is most sensitive to its parameters. This, in turn, constitutes the basis for model-based experiment design and interpretation [e.g., *Fajraoui et al*., 2011 and references therein].

A useful approach for the design, analysis and interpretation of conservative transport experiments in porous media is based on Global Sensitivity Analysis (GSA). The latter provides a convenient and powerful way to identify space-time locations where a model is most sensitive to its unknown parameters. GSA is applied in several fields of engineering [*Saltelli et al*., 2000; *Sudret*, 2008] and it has also be used to illustrate the way design of laboratory-scale experiments and parameter calibration based on the classical Advection-Dispersion Equation (ADE) model can be improved [*Fajraoui et al*., 2011].

However, a detailed study of parameter sensitivity for the design and interpretation of laboratory-scale conservative transport experiments based on a set of alternative process-based models has not been undertaken. Most notably, quantification and comparative analysis of the sensitivity of widely used transport formulations such as (a) a dual-porosity (DP) model with mass transfer between mobile and immobile regions [*Huang et al*., 2003; *Bai et al*., 1995], and (b) the Continuous Time Random Walk (CTRW) [e.g., *Berkowitz et al*., 2006 and references therein] to their parameters has not been reported in the literature.

Here, the focus consists in the conservative transport experiment presented by *Gramling et al*. [2002], performed within a laboratory chamber filled with a uniform reconstructed porous medium. The selected candidate interpretive model are: (a) the classical advection-dispersion equation (ADE), (b) a dual-porosity (DP) scheme with mass transfer between mobile and immobile regions, and (c) the Continuous Time Random Walk (CTRW) formulation. The space-time distribution of solute concentration along the chamber is considered as the system state against which (a) perform a PCE-based GSA, (b) analyze the sensitivity of each model to its parameters, (c) explore the feasibility of estimating key model parameters based on a limited set of data, measured at locations determined by the results of the GSA, (d) apply formal model discrimination criteria to quantify (in a relative sense) the ability of these alternative models to interpret experimental observation, and (e) assess the predictive ability of the selected models.

The employed methodology allows quantification of (a) the relative importance of the parameters associated with each model tested, and (b) the space-time locations where the system state is most sensitive to model parameters. This information is relevant for model-based experiment

design and robust parameter calibration at affordable computational cost. In this application, parameter calibration is performed within a Maximum Likelihood context [e.g., *Carrera and Neuman*, 1986]. Model identification (discrimination) criteria are then employed to (a) rank the alternative models selected and (b) estimate the model relative degree of likelihood through a posterior probability measure for the selected case study [*Ye et al*., 2008; *Bianchi Janetti et al*., 2012, and references therein].

5.2 CASE STUDY EXPERIMENT

Chamber length (cm)	36
Chamber cross section (cm^2)	$5.5 \times 1.8 = 9.9$
Average grain size (cm)	0.13
Porosity	0.36
Flow rate (mL/min)	2.67
Velocity (cm/s)	1.21×10^{-2}
Hydrodynamic dispersion coefficient$^{(*)}$ (cm^2/s)	1.75×10^{-3}
Chamber dispersivity$^{(*)}$ (cm)	0.145
Grain Peclet number	2.24×10^{3}
Reynolds number	0.157
Observation times (s)	532 / 1023 / 1523 / 2023

Table 5.1. Experimental conditions of the conservative transport experiment of *Gramling et al*. [2002]. $^{(*)}$ Values calibrated by *Gramling et al*. [2002] on the basis of the measured concentration profiles.

Gramling et al. [2002] illustrate the results of a conservative transport experiment performed in a laboratory-scale, glass (rectangular) flow chamber filled with millimeter-sized grains of cryolite. A solution of

$CuEDTA^{2-}$ (at 0.01 *M* concentration) was injected continuously into the chamber, displacing a solution of Na_2EDTA^{2-} with initial concentration of 0.02 *M*. The authors report the relative concentration profiles of $CuEDTA^{2-}$ at four different times (τ_1 = 532 s, τ_2 = 1023 s, τ_3 = 1523 s, and τ_4 = 2023 s), from which about 380 measurements of solute concentration can be derived. The main characteristics of the experiment are summarized in Table 5.1.

5.3 DESCRIPTION OF THE SELECTED TRANSPORT MODELS

In the following, the main features of the competing models that we adopt to represent the migration of a conservative solute in a uniform porous medium are summarized. These model are: (i) the classical ADE, (ii) a DP scheme with mass transfer between mobile and immobile phases, and (iii) the CTRW formulation. A one-dimensional transport scenario is considered, following the usual practice adopted in interpretation of flow-through laboratory chamber experiments such as that reported in *Gramling et al.* [2002].

Key flow and transport parameters are represented as independent random variables and analyze how the uncertainty associated with their values propagates to solute concentrations through the three selected transport models. Table 5.2 reports the input random parameters and the corresponding probability distributions adopted in this study. Uncertain parameter values are generally assumed to be distributed normally, with the exception of parameters whose range of variability may entail negative values that have no physical meaning. A lognormal distribution is adopted for these latter parameters. Mean parameter values were selected on the

basis of (a) calibration results obtained by *Gramling et al.* [2002] (with reference to dispersivity, effective velocities and medium porosity), or (b) preliminary calibration against the complete dataset. Values of parameter standard deviation were selected to ensure that relatively wide intervals in the parameter space were explored, while minimizing the possibility of sampling negative values in the case of Normal distributions.

Parameter	**Model**	**Distribution**	**Mean**	**Standard Deviation**
Effective velocity (v)	ADE	Normal	1.21×10^{-4} m/s	1.00×10^{-6} m/s
Flux (q)	DP	Normal	4.356×10^{-5} m/s	5.11×10^{-7} m/s
Longitudinal dispersivity (α_L)	ADE /DP	Lognormal	1.45×10^{-3} m	4.50×10^{-4} m
Mobile porosity (f)	DP	Normal	0.36	3.00×10^{-3}
Mass transfer (K)	DP	Normal	1.00×10^{-5} 1/s	3.00×10^{-6} 1/s
Transport velocity (v_ψ)	CTRW	Normal	1.21×10^{-4} m/s	1.00×10^{-6} m/s
Generalized dispersion coefficient (D_ψ)	CTRW	Normal	1.75×10^{-7} m^2/s	5.44×10^{-8} m^2/s
Exponent of TPL distribution (β)	CTRW	Normal	1.97	9.85×10^{-2}
Characteristic transition time (t_1)	CTRW	Lognormal	6.6 s	3.3 s
Cut-off time (t_2)	CTRW	Lognormal	100 s	50 s

Table 5.2. Model parameters and adopted sampling distributions.

5.3.1 Advection-Dispersion Equation model

The one-dimensional ADE describing solute migration in homogeneous porous media can be written as

$$\frac{\partial c(x,t)}{\partial t} = D\frac{\partial^2 c(x,t)}{\partial x^2} - v\frac{\partial c(x,t)}{\partial x}. \tag{5.1}$$

Here, $c(x,t)$ is solute concentration at location x and time t, $v = q/\phi$ is average flow velocity (q and ϕ respectively being Darcy flux and medium porosity) and D is hydrodynamic dispersion ($D = \alpha_L v$, with α_L the longitudinal dispersivity). The following initial and boundary conditions are considered:

$$c(x,0) = c_0;\ c(0,t) = c_0;\ \text{c'(L, t) = 0}. \tag{5.2}$$

An analytical solution can be found in Laplace space by rewriting (5.1)-(5.2) as

$$D\frac{d^2\tilde{c}(x,u)}{dx^2} - v\frac{d\tilde{c}(x,u)}{dx} - u\tilde{c}(x,u) = 0;\ \tilde{c}(0,u) = \frac{c_0}{u};\ \tilde{c}'(L,u) = 0, \tag{5.3}$$

where $\tilde{c}$ is the Laplace transform of c and u is the Laplace parameter. The solution of (5.3) is

$$\tilde{c}(x,u) = k_1 e^{\lambda_+ x} + k_2 e^{\lambda_- x}, \tag{5.4}$$

where $\lambda^{\pm} = \frac{v}{2D} \pm \sqrt{\frac{v^2}{4D^2} + \frac{u}{D}}$ and k_1, k_2 are constants to be determined. Substituting the transformed boundary conditions in (5.3) into (5.4) leads to $k_1 = -\frac{c_0 UR}{u(1-UR)}$ and $k_2 = \frac{c_0}{u(1-UR)}$, with $R = \frac{e^{\lambda^- L}}{e^{\lambda^+ L}}$, $U = \frac{\lambda^-}{\lambda^+}$. The analytical solution is then inverted numerically by the algorithm of *Stehfest*

[1970]. Effective velocity and dispersivity are here considered as model parameters whose values are affected by uncertainty (Table 5.2).

5.3.2 Dual Porosity model

The DP scheme considers mass transfer between a mobile and an immobile phase which are assumed to constitute the porous domain. This conceptualization of mass-transfer processes is typically employed to represent pore-scale mass fluxes that are not explicitly described by a continuum Darcy-scale model such as the ADE. In this context, the immobile domain represents pore-scale low velocity regions where solute mass can enter and retained, so that its displacement is delayed when compared to the advance of mass within mobile regions [*Huang et al*., 2003; *Bai et al*., 1995]. The corresponding mathematical formulation is provided by the system of partial differential equations

$$f\frac{\partial c(x,t)}{\partial t}+(1-f)\frac{\partial c^{*}(x,t)}{\partial t}=D'\frac{\partial^{2}c(x,t)}{\partial x^{2}}-q\frac{\partial c(x,t)}{\partial x} \tag{5.5a}$$

$$(1-f)\frac{\partial c^{*}(x,t)}{\partial t}=K\left[c(x,t)-c^{*}(x,t)\right] \tag{5.5b}$$

where c and $c*$ are the solute concentrations in the mobile and immobile regions. Here, f is the fraction of mobile pore space in the porous medium, K is the rate of mass transfer between mobile and immobile fluid flow regions, and $D' = \alpha_L q$. Let consider for c the initial and boundary conditions (5.2), while $c*$ is subject to the following initial and boundary conditions:

$$c*(x,0)=c_0*;\ c*(0,t)=c_0*;\ c*'(L,t)=0\ . \tag{5.6}$$

Transforming the equations into Laplace space renders

$$D'\frac{d^2\tilde{c}(x,u)}{dx^2} - q\frac{d\tilde{c}(x,u)}{dx} - \xi\,\tilde{c}(x,u) = 0,\quad \tilde{c}^*(x,u) = \frac{K\,\tilde{c}(x,u)}{(1-f)u+K} \tag{5.7}$$

$$\tilde{c}(0,u) = c_0/u;\quad \tilde{c}^*(0,u) = c_0^*/u;\quad \tilde{c}'(L,u) = \tilde{c}^{*}{}'(L,u) = 0, \tag{5.8}$$

where $\tilde{c}$ and $\tilde{c}^*$, respectively, being the transformed variables of c and c^*, and $\xi = u\left(\frac{f(1-f)u+K}{(1-f)u+K}\right)$. The solution of (5.7) is given by (5.4), where $\lambda^{\pm} = \frac{q}{2D'} \pm \sqrt{\frac{q^2}{4D'^2} + \frac{\xi}{D'}}$. Here, the selected model parameters with uncertain values are (Table 5.2) Darcy velocity, q, the mobile porosity of the medium, f, the mass transfer rate, K, and the longitudinal dispersivity, α_L.

5.3.3 Continuous Time Random Walk model

The CTRW framework is based on a conceptual picture of solute particles undergoing multiple spatial transitions according to a distribution of lengths, and characterized by a distribution of travel times. For a conservative solute, the nature of the domain heterogeneity and the flow regime determine the functional form of the transition time distribution and the associated parameter values. The CTRW approach has been shown to be particularly effective in quantifying non-Fickian (or anomalous) transport behavior, characterized by early arrival and long time tailing of solute in measured breakthrough curves, over a wide range of length scales, types of porous and fractured media, and associated degrees of spatial heterogeneity. The governing transport equation can be formulated as [*Berkowitz et al*., 2006]

$$\frac{\partial c(x,t)}{\partial t} = -\int_0^t M(t-t')\left[v_\psi \frac{\partial c(x,t')}{\partial x} - D_\psi \frac{\partial^2 c(x,t')}{\partial x^2} \right] dt' \tag{5.9}$$

or more conveniently in Laplace space as

$$u\tilde{c}(x,u) - c_0(x) = -\tilde{M}(u)\left[v_\psi \frac{\partial}{\partial x}\tilde{c}(x,u) - D_\psi \frac{\partial^2}{\partial x^2}\tilde{c}(x,u) \right] \tag{5.10}$$

where the memory function $\tilde{M}(u)$, which accounts for the unknown heterogeneities below the level of measurement resolution, is given by

$$\tilde{M}(u) = t_1 u\tilde{\psi}(u)/\left[1-\tilde{\psi}(u)\right]. \tag{5.11}$$

In (5.10)-(5.11), t_1 is a characteristic transition time, $c_0(x)$ is the initial condition, and v_ψ and D_ψ are the transport velocity and generalized dispersion coefficient, respectively, based on the first and second moments of the transition length probability density function divided by the characteristic time. The transport velocity, v_ψ, is distinct from the average fluid velocity, v, and they need not be equal (v_ψ is averaged across the tracer particles, while v is averaged across all water particles). This is in contrast to the ADE and DP models, for which these velocities are identical. Similarly, the dispersion coefficient D_ψ has a different physical interpretation than in the ADE and DP models [see *Berkowitz et al*., 2006, for a detailed discussion].

The transition time distribution, $\psi(t)$, determines the probability rate for a transition time t between sites in the medium, and thus controls the overall nature of the transport. A truncated power law (TPL) formulation of $\psi(t)$ has been shown to describe transport in a diverse set of physical scenarios [*Dentz et al*., 2004; *Berkowitz et al*., 2006]. It contains a "cut off" time t_2 of the power law that allows evolution from non-Fickian

(anomalous) behavior to Fickian behavior at long times. The TPL can be written as

$$\psi(t) = \frac{n}{t_1}\frac{\exp(-t/t_2)}{\left[1+(t/t_1)\right]^{1+\beta}};\ 0<\beta<2;\ n=\left[\left(\frac{t_1}{t_2}\right)^{\beta}\exp\left(\frac{t_1}{t_2}\right)\Gamma\left(-\beta,\frac{t_1}{t_2}\right)\right]^{-1} \quad (5.12)$$

Here, n is a normalization factor, β is a parameter characterizing the nature of the dispersive transport, the cut-off time $t_2 >> t_1$, and $\Gamma(a, s)$ is the incomplete gamma function. The TPL behaves as a power law for $t_1 << t << t_2$, and decreases exponentially for $t >> t_2$. The overall transport is Fickian for $\beta > 2$, while decreasing β leads to increasingly dispersive transport. Further discussion on the choice of these parameters and their effect on concentration tailing as a function of flow velocity is given in *Berkowitz and Scher* [2009]. Referring to (5.10) and (5.11), appropriate choice of $\psi(t)$ allows recovery of the ADE and double porosity models as special, limit cases of these equations (e.g., for a purely exponential $\psi(t)$, $\tilde{M}(u) = 1$, and the ADE is obtained).

Equation (5.10) together with appropriate boundary conditions is solved using the CTRW Matlab Toolbox [*Cortis and Berkowitz*, 2005;]. Selected model parameters with uncertain values are (Table 5.2) transport velocity, v_ψ, the generalized dispersion coefficient, D_ψ, the exponent β and the cut-off times t_1 and t_2.

5.4 MAXIMUM LIKELIHOOD PARAMETER ESTIMATION AND MODEL QUALITY CRITERIA

Let N be the number of available observations of the model response Y collected in the vector $\mathbf{Y}^* = \left[Y_1^*,...Y_N^*\right]$. The covariance matrix of

measurement errors, $\mathbf{B}_Y$, is here considered to be diagonal with non-zero terms equal to the observation error variance σ_i^2 [*Carrera and Neuman*, 1986]. Denoting by $\hat{\mathbf{Y}} = \left[\hat{Y}_1 \,, ... \hat{Y}_N\right]$ the vector of model predictions at locations where measurements are available, the ML estimate $\hat{\mathbf{X}}$ of the vector of the M uncertain model parameters can be obtained by minimizing with respect to $\mathbf{X}$ the negative log likelihood criterion:

$$NLL = \sum_{i=1}^{N} \frac{J_i}{\sigma_i^2} + \ln\left|\mathbf{B}_Y\right| + N\ln(2\pi), \tag{5.13}$$

where $J_i = \left(Y_i^* - \hat{Y}_i\right)^2$. The criterion (5.13) includes the weighted least square criterion [*Carrera and Neuman*, 1986; *Bianchi Janetti et al*., 2012 and references therein]. Here, minimization of (5.13) is achieved using the iterative Levenberg-Marquardt algorithm as embedded in the code PEST [*Doherty*, 2002].

Alternative competing models which can be used to interpret available system states can be ranked by various criteria [e.g., *Neuman*, 2003; *Ye et al*., 2004, 2008; *Neuman et al*., 2011; *Bianchi Janetti et al*., 2012 and references therein], including:

$$AIC = NLL + 2M\,, \tag{5.14}$$

$$AIC_c = NLL + 2M + \frac{2M(M+1)}{N-M-1}\,, \tag{5.15}$$

$$KIC = NLL + M\ln\left(\frac{N}{2\pi}\right) - \ln\left|\mathbf{Q}\right|\,, \tag{5.16}$$

where the Akaike information criterion, *AIC*, is due to *Akaike* [1974], AIC_c to *Hurvich and Tsai* [1989] and *KIC* to *Kashyap* [1982]. In (5.16), $\mathbf{Q}$

represents the Cramer-Rao lower-bound approximation for the covariance matrix of the parameter estimates [see *Ye et al.*, 2008 for details]. Such a covariance matrix provides a measure of the quality of parameter estimates and of the information content carried by data about model parameters. Embedding **Q** in the formulation allows *KIC* to indicate that selecting a model with a high number of parameters might not be justified in the presence of a limited and/or poor quality set of data.

These model discrimination criteria can also be employed to assign posterior probability weights to the various tested models, thus quantifying prediction uncertainty. The posterior probability related to model M_k (k = 1, ..., N_M, with N_M the number of available process models) is calculated as [*Ye et al.*, 2008]:

$$p(M_k \mid \mathbf{Y}^*) = \frac{\exp\left(-\frac{1}{2}\Delta IC_k\right) p(M_k)}{\sum_{i=1}^{N_M} \exp\left(-\frac{1}{2}\Delta IC_i\right) p(M_i)}, \tag{5.17}$$

here $\Delta IC_k = IC_k - IC_{min}$, with IC_k being either *AIC* (5.14), AIC_c (5.15) or *KIC* (5.16) and $IC_{min} = \min\{IC_k\}$ its minimum value over the competing models considered; $p(M_k)$ is the prior probability associated with each model. In this application no prior information is available consequently it is convenient to set $p(M_k) = 1/N_M$, so that all models are associated with equal prior probability. The adoption of model identification criteria and posterior model probabilities allows ranking of the candidate models analyzed on the basis of their associated posterior probabilities and discrimination among them in a relative sense. Such a study has not yet been conducted with reference to the interpretation of laboratory-based transport experiments in conjunction with a sensitivity-driven calibration of model parameters.

5.5 SENSITIVITY-BASED MODELING STRATEGY

The presented modeling and interpretation strategy is developed according to the following steps:

1. selection of a transport model;
2. definition of probability distributions for model parameters whose values are uncertain and need to be calibrated against measurements of state variables;
3. computation of the PCE-approximation of the selected model at (space-time) locations of interest: this requires computation of the coefficients $a_j(x,t)$ by means of, e.g., a regression-based approach [*Sudret*, 2008; *Ciriello et al*., 2012];
4. analytical derivation of the Sobol indices: the total and principal sensitivity indices are calculated for each model parameter at all (space-time) locations of interest (note that when these indices differ significantly throughout the system, then the effect of interactions among parameters might not be negligible and additional terms need to be computed);
5. identification for each parameter of (i) the overall influence on the model response through the average of the associated total sensitivity indices, and (ii) the space-time locations where local maxima of such total sensitivity indices occur;
6. identification of the sensitivity-based calibration datasets: in the application, this leads to identifying subsets of the concentration measurements presented in *Gramling et al*. [2002, their Figure 4];
7. ML estimation (5.13) of model parameters upon considering (i) the complete sets of concentration measurements corresponding to the

first, second and third observation times presented in *Gramling et al.* [2002, their Figure 4], and (ii) sensitivity-based data subsets;

8. repetition of steps 1-7 for all tested models;
9. computation of model quality criteria (5.14)-(5.16) and posterior probability weights (5.17) to rank the interpretive capability of the selected models for each calibration set;
10. assessment of the predictive capability of each model by comparison of model results against observations collected at space-time locations which are not employed in the parameter calibration procedure.

5.6 RESULTS AND DISCUSSION

Here the results of the application of the sensitivity-based strategy are presented to the specific case study described in Section 5.2. Implications to model-based experimental design are also reported.

5.6.1 GSA of the selected transport models

Table 2 reports the uncertain parameters considered for the three selected models, together with the corresponding probability distributions adopted. For each model analyzed, the analysis was performed by employing a PCE at different orders (p = 2, 3, 4). For illustration purposes, the results obtained through a PCE of order 2 are reported here. These do not differ significantly from those obtained with higher order PCE (not shown). Note that the quantitative results illustrated are tied to the specific experimental setup considered. While different experimental settings (in terms of, e.g., flow domain and configuration and transport scenario) might lead to different results, the application of the GSA-based methodology is

general and allows discrimination of the relative effects of the different model parameters considered.

Figure 5.1 juxtaposes the concentration profiles, $c(x)$, of the conservative experiment reported by *Gramling et al*. [2002] and the related total sensitivity indices of the parameters associated with the ADE for given observation times. Curves in Figure 5.1 represent the spatial distribution of the total sensitivity indices associated with the ADE parameters and calculated for each observation time on the basis of the PCE technique. These curves allow identification of the locations in the chamber where the ADE is highly or poorly sensitive to its parameters depending on the local values of the total sensitivity indices. Corresponding depictions for the DP and CTRW formulations are presented in Figure 5.2 and Figure 5.3, respectively.

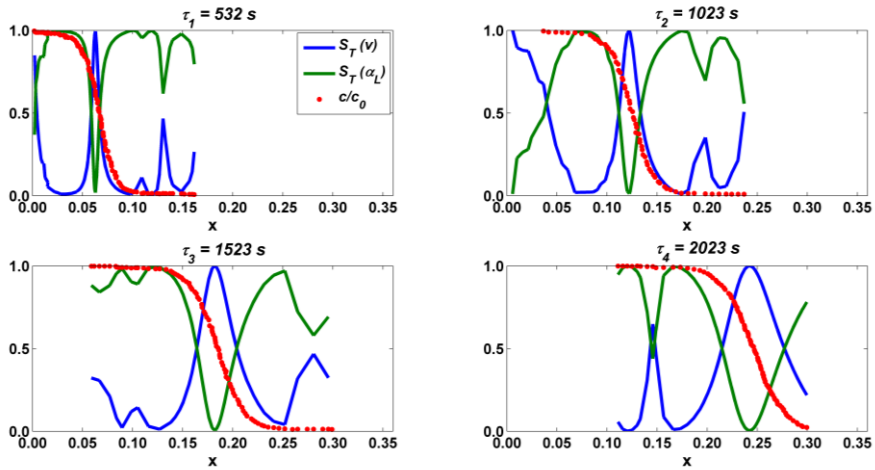

Figure 5.1. Space-time concentration profiles from *Gramling et al.* [2002, Figure 4] and Total Sensitivity Indices ($S_T(\Omega)$, $\Omega = v, \alpha_L$) associated with the parameters of the ADE model.

Figure 5.1 shows that the sensitivity indices of the two parameters appearing in the ADE (i.e., v and α_L) are in general anti-correlated. Locations where the effects of a parameter are dominant are clearly identifiable by a sharp local peak or by persistently high values of the total sensitivity index. It's observable that in general the uncertainty associated with the velocity dominates the transport process in the proximity of the inflection point of the concentration profiles. This location corresponds to solute center of mass and is associated with virtually vanishing sensitivity to dispersivity. In contrast, dispersivity appears to play a dominant role close to the tails of the concentration profile. This result is consistent with the format of the ADE, where dispersivity is linked to the spreading of the concentration distribution around the center of mass, while the displacement of the center of mass is typically governed by advective processes.

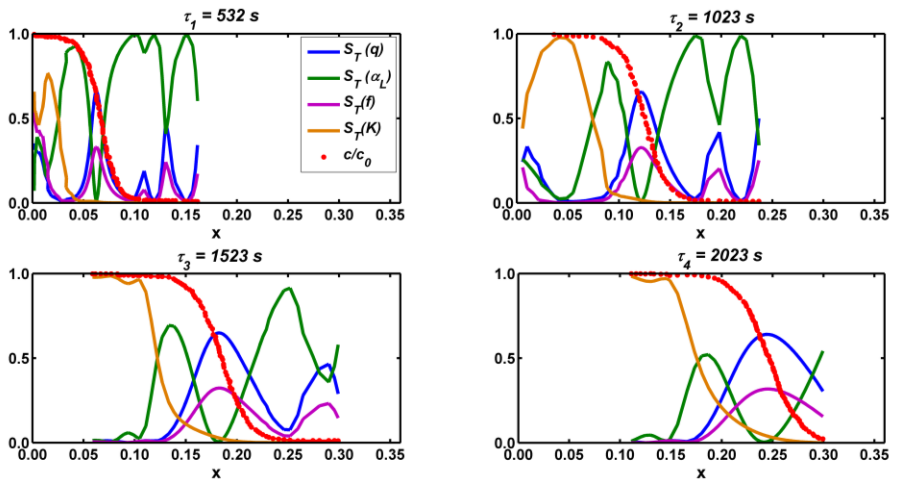

Figure 5.2. Space-time concentration profiles from *Gramling et al.* [2002, Figure 4] and Total Sensitivity Indices ($S_T(\Omega)$, $\Omega = q, \alpha_L, f, K$) associated with the parameters of the DP model.

With reference to the DP formulation, Figure 5.2 reveals that the role of the mass transfer coefficient, *K*, appears to be less significant at the advancing solute front than at locations in the upstream part of the concentration profiles. This observation is consistent with the main effect of this parameter which is associated with delayed diffusion of solute from immobile to mobile regions. The total sensitivities to Darcy velocity and porosity are very similar for the four observation times, the system state appearing to be slightly more sensitive to Darcy flux than to porosity. Dispersivity plays a relevant role in the DP formulation, being the most important parameter for earlier times. The effect of dispersivity on the variance of the system response tends to decrease with time, consistent with the increased impact of advective processes with solute residence time.

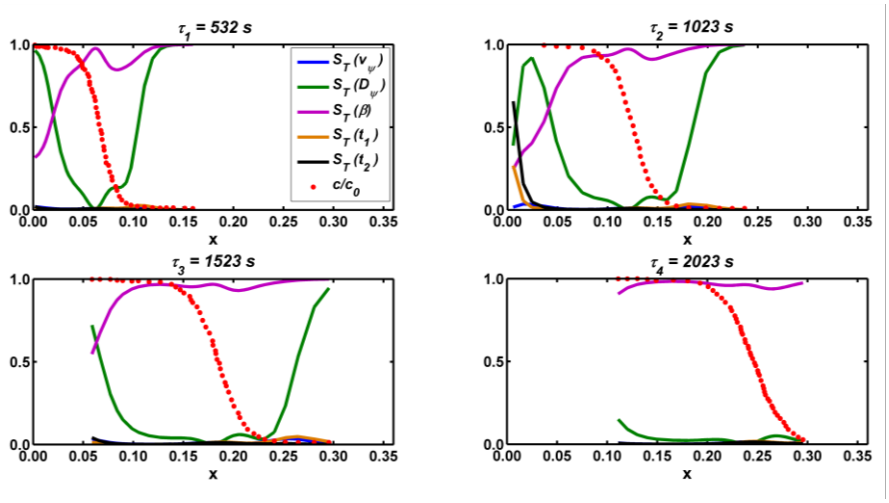

Figure 5.3. Space-time concentration profiles from *Gramling et al.* [2002, Figure 4] and Total Sensitivity Indices ($S_T(\Omega)$, $\Omega = v_\psi, D_\psi, \beta, t_1, t_2$) associated with the parameters of the CTRW model.

Figure 5.3 clearly shows that the parameter β appearing in the CTRW formulation always plays the most prominent role, the importance of D_ψ being significant only for the observations available at earliest times. The transport velocity v_ψ and the two characteristic times t_1 and t_2 display a similar behavior and appear to be only marginally relevant in this case study and for the selected variability interval. This is likely related to the relative uniformity of the reconstructed porous medium where the entire spectrum of transition times can be sampled by solute particles migrating through the system. These findings imply that β and D_ψ are the only relevant parameters for model calibration in the experimental setting considered here, because they encapsulate the key information on the variability of the system response.

Comparison of Figures 5.1 and 5.2 indicates that the main features of the spatial distribution of the sensitivities of the parameters (i.e., dispersivity and velocity/flux) that appear within both the ADE and DP formulations are qualitatively similar. These formulations are sensitive to all parameters, albeit with various degrees and at different locations. On the other hand, it is noted that the CTRW model is essentially sensitive to only two parameters.

To complete the analysis, Table 5.3 reports the mean values of the total sensitivity indices associated with the uncertain parameters, as calculated on the basis of the complete available data set (i.e., considering the four concentration profiles presented in *Gramling et al*. [2002]). This allows ranking the global importance of each parameter and provides valuable information for the parameter calibration step.

Model	Parameter	Mean values of S_T
ADE	Longitudinal dispersivity (α_L)	0.581
ADE	Effective velocity (v)	0.435
DP	Longitudinal dispersivity (α_L)	0.356
DP	Flux (q)	0.346
DP	Mobile porosity (f)	0.178
DP	Mass transfer (K)	0.147
CTRW	Exponent of TPL distribution (β)	0.905
CTRW	Generalized dispersion coefficient (D_ψ)	0.174
CTRW	Characteristic transition time (t_1)	0.012
CTRW	Cut-off time (t_2)	0.012
CTRW	Transport velocity (v_ψ)	0.010

Table 5.3. Mean values of the total sensitivity indices calculated on the complete set of available concentration data.

One can observe that for each selected model, the sum of the mean values of the total sensitivity indices associated with the parameters is generally larger than unity. This is due to contributions of parameter interactions to the variance of the model output. Table 5.3 suggests that this contribution is globally negligible for the three models tested, as the sum of the mean values of the total sensitivity indices associated with the parameters of a given model is close to unity. Further note that Figures 5.1 and 5.2 indicate that the principal and total sensitivity indices virtually coincide at almost all space-time locations for the ADE and DP models. On the other hand, Figure 5.3 indicates the occurrence of a non-negligible mutual influence between β and D_ψ. The effect of the interaction between these two parameters is confined within a small region close to the domain boundaries. Because this effect is modest and restricted to very limited areas, computation of the second-order Sobol indices is not performed.

The PCE technique provides a surrogate model which is formulated in terms of the model parameters. The quality of the approach and results presented here were assessed by comparing concentration profiles obtained by a given model and the corresponding PCE approximation (not shown) for several sets of parameter values randomly sampled within the ranges of variability indicated in Table 5.2. It was found that the concentration profiles calculated with the complete model and its PCE approximation were essentially identical in all cases (not shown).

5.6.2 Parameter calibration and model identification criteria

Calibration of the parameters of the three selected models to available concentration data is performed on the basis of the results and observations presented in the previous section. Different subsets are considered of the available database upon which model calibration is performed. This allows assessing the influence of the selection of measurement (space-time) location on the quality of the parameter calibration results and application of model discrimination criteria analysis.

Table 5.4 lists the different data subsets adopted, including the number of data points associated with each of these. As an example, Figure 5.4 depicts the location of the measurement points selected for subset 4 in Table 5.4. The first three available concentration profiles are considered separately in their entirety (sets 1, 2, 3 in Table 4) to investigate time-dependence of the parameters. GSA methodology is then applied by selecting sets of observation points which are most sensitive to the parameters. In particular this is done by selecting such sets within different concentration profiles (sets 4 and 5 in Table 5.4) and considering different sample sizes (sets 5 and 6 in Table 5.4). This procedure enables (i)

investigation of the possibility of optimizing the use of information content associated with observations for calibration purposes, and (ii) adoption of the remaining observations to validate model predictions.

Subset	Description	Number of observations
1	All observations from concentration profile at τ_1	110
2	All observations from concentration profile at τ_2	73
3	All observations from concentration profile at τ_3	92
4	Most sensitive observations from concentration profile at τ_1	20
5	Most sensitive observations from concentration profiles at τ_2 and τ_3	20
6	Most sensitive observations from concentration profiles at τ_2 and τ_3	40

Table 5.4. Calibration sets for the three selected models.

Table 5.5 reports the values of the model parameters obtained upon performing calibration on the basis of the different data subsets presented in Table 5.4. For each estimated parameter Table 5.5 also reports the ratio, *R*, of the difference between the lower and upper limit identifying the 95% estimate confidence limits and the estimated value. As expected, this ratio is smallest for the model with the smallest number of parameters. In particular, it is noted that the quality of the estimate of parameters t_1 and t_2 of the CTRW model is relatively poor, consistent with the observation that the model is not sensitive to these two parameters as revealed by the GSA (Figure 5.3).

From examination of Table 5.5, it's observable that in the ADE model the (calibrated) value of the velocity, *v*, does not depend on the particular choice of subset. A similar observation can be made with reference to the

flux, q, in the DP model which exhibits variations of only a few percent amongst different subsets. On the contrary, calibration of dispersivity, α_L, for both the ADE and DP models appears to be impacted by the choice of the data subset, with calibration values decreasing slightly over time (subsets 1, 2, 3). Calibrated porosity, f, in the DP model virtually coincides with the average value of its distribution in all calibration subsets. The mass transfer coefficient, K, exhibits a calibrated value associated with subsets relative to early observation times (subsets 1, 4) which is significantly higher than that resulting from calibrating the model against data taken at later times.

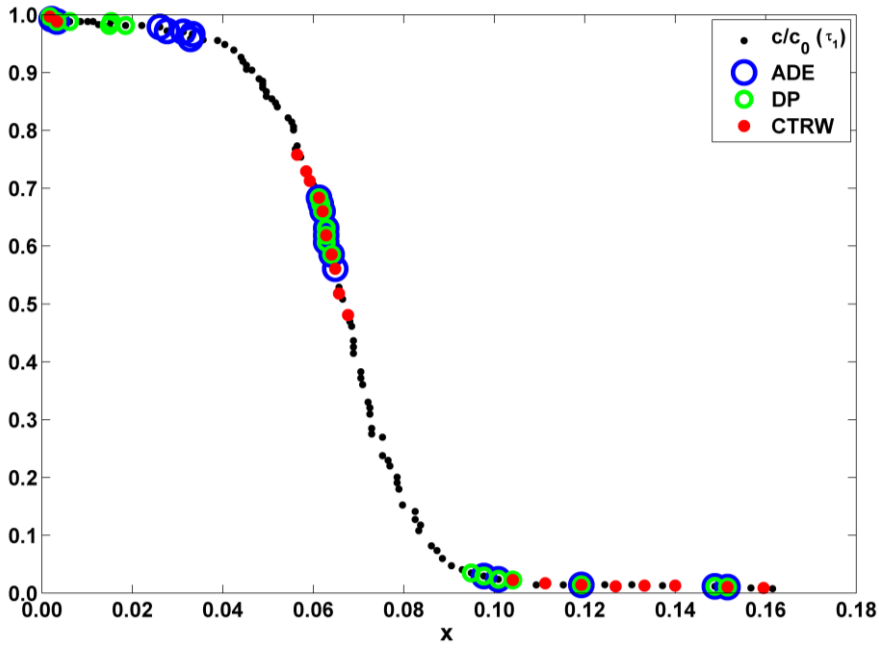

Figure 5.4. Concentration profile at time τ_1 from *Gramling et al.* [2002] and sensitivity-based observation subset 4 (Table 5.4) selected for the ADE, DP and CTRW models.

With reference to the CTRW model, the cut-off time, t_2, is remarkably stable for all subsets considered, regardless of the lack of model sensitivity to this parameter. A similar observation can be made for the characteristic transition time, t_1, with the only exception of the scenario corresponding to the adoption of the first concentration profile as a calibration subset (subset 1). The generalized dispersion coefficient, D_ψ, is associated with calibrated values which virtually coincide with the average of the selected distribution with the only exception of the early observation times (subsets 1, 4). The calibration values of the exponent of the TPL distribution, β, and transport velocity, v_ψ, show opposing trends over time. Note that large calibrated values of v_ψ are found for early observation times, while the reverse is true for β (subsets 1, 2, 3).

From Table 5.5 it is shown that the confidence intervals related to the estimates of v for the ADE model tend to overlap for all data subsets with the exception of the case associated with early observation times (subsets 1 and 4) where the calibrated velocity is associated with relatively large confidence intervals. Dispersivity values are also statistically indistinguishable for the calibrations based on the GSA results and for subsets 2 and 3. This indicates that selection of a smaller set of data points does not affect notably the values of the estimated parameters in this example. Confidence intervals associated with the DP model appear to be still relatively small for the first two data subsets where a large amount of data is adopted and tailing behavior associated with delayed diffusion is visible in the experimental concentration curves. All subsets selected render statistically equivalent results for the calibration of q, f, and K. Dispersivity calibration results observed for the ADE also hold for the DP.

With reference to the CTRW model, it is noted that all confidence intervals associated with the estimated parameters tend to significantly

overlap. Parameter β, which is also the most influential to the system behavior, is the one which is best estimated for this experimental setting. As the cut-off times t_1 and t_2 are not influential for the case study, model calibration is also performed by setting t_1 and t_2 at the mean values of their distributions and estimating the remaining three parameters. In this case, the estimated values of v_ψ, D_ψ and β virtually coincide with those listed in Table 5.5. As expected, the width of the resulting confidence intervals decreases significantly, with values of R which are generally one order of magnitude lower than those presented in Table 5.5 (not shown).

Model	Parameter	Subset 1		Subset 2		Subset 3	
		C	R	C	R	C	R
ADE	v	1.22E-04	7.03E-03	1.21E-04	6.91E-03	1.20E-04	5.76E-03
ADE	α_L	1.53E-03	1.13E-01	1.25E-03	2.01E-01	1.04E-03	2.71E-01
DP	q	4.51E-05	5.09E-01	4.39E-05	4.55E-01	4.35E-05	6.17E+00
DP	α_L	1.18E-03	1.76E-01	1.04E-03	3.43E-01	8.93E-04	7.90E-01
DP	f	3.60E-01	5.09E-01	3.60E-01	4.60E-01	3.60E-01	6.17E+00
DP	K	5.17E-05	7.69E-01	1.42E-05	1.24E+00	5.57E-06	5.52E+00
CTRW	v_ψ	1.39E-04	2.62E+01	1.33E-04	4.47E+00	1.30E-04	2.37E+00
CTRW	D_ψ	2.20E-07	6.52E+00	1.72E-07	2.79E+01	1.73E-07	8.43E+00
CTRW	B	1.87E+00	1.20E+01	1.89E+00	3.47E+00	1.91E+00	1.46E-01
CTRW	t_1	6.00E+00	2.41E+02	6.60E+00	4.53E+02	6.50E+00	1.20E+02
CTRW	t_2	1.00E+02	8.86E+02	1.00E+02	3.43E+02	1.01E+02	1.23E+02

Model	Parameter	Subset 4		Subset 5		Subset 6	
		C	R	C	R	C	R
ADE	v	1.24E-04	1.67E-02	1.21E-04	6.81E-03	1.21E-04	6.07E-03
ADE	α_L	2.29E-03	4.65E-01	2.65E-03	2.65E-01	2.45E-03	2.45E-01
DP	q	4.48E-05	2.95E+00	4.36E-05	4.21E+00	4.12E-05	2.48E+00
DP	α_L	1.80E-03	3.58E-01	2.71E-03	3.45E-01	2.38E-03	2.92E-01
DP	f	3.53E-01	2.95E+00	3.60E-01	4.20E+00	3.40E-01	2.48E+00
DP	K	4.29E-05	2.97E+00	3.65E-06	9.73E+00	2.08E-06	6.46E+00
CTRW	v_ψ	1.11E-04	4.76E+01	1.21E-04	1.32E+01	1.21E-04	5.96E+00
CTRW	D_ψ	1.67E-07	2.48E+01	1.75E-07	1.67E+01	1.75E-07	1.09E+01
CTRW	β	2.09E+00	3.17E+01	1.97E+00	3.54E+00	1.97E+00	1.81E+00
CTRW	t_1	6.60E+00	9.76E+02	6.60E+00	3.26E+02	6.60E+00	2.27E+02
CTRW	t_2	1.00E+02	6.79E+02	1.00E+02	7.12E+02	1.00E+02	3.67E+02

Table 5.5. Calibrated values, *C*, of model parameters and ratio, *R*, of the difference between the lower and upper limits identifying the 95% estimate confidence limits and *C*.

Comparison amongst the competing models for each calibration set is then possible on the basis of the model identification criteria (5.14)-(5.16) and posterior probabilities (5.17). Table 5.6 presents the value of *NLL* (5.13) together with model identification criteria results (i.e., *AIC* (5.14), AIC_c (5.15), *KIC* (5.16)) for the selected competing transport models and each calibration subset. The posterior probability calculated on the basis of the *AIC* (5.14) criterion is also included for completeness. Evaluating posterior probability according to the other discrimination criteria considered does not produce significantly different results.

Note first that the posterior model weights indicate that one model always has a markedly high degree of likelihood at the expense of the remaining two, depending on the set of observations considered. For example, considering the second and the third concentration profiles

(subsets 2, 3), respectively, clearly renders the DP and CTRW as the best interpretive models. In contrast, extracting only the most sensitive observations from these two profiles (subsets 5, 6) results in the ADE being clearly preferable to the other transport models. The DP emerges as the best modeling choice for the early-time observations (subsets 1, 4).

Subset	ADE				
	NLL (19)	AIC (20)	AIC_c (21)	KIC (22)	Posterior prob. (23)
1	-708.010	-704.010	-703.897	-651.400	0.000
2	-452.809	-448.809	-448.635	-397.710	0.050
3	-541.258	-537.258	-537.121	-485.623	0.000
4	-138.268	-134.268	-133.518	-90.339	0.021
5	-158.358	-154.358	-153.608	-107.734	0.995
6	-292.599	-288.599	-288.266	-240.207	0.999
Subset	DP				
	NLL (19)	AIC (20)	AIC_c (21)	KIC (22)	Posterior prob. (23)
1	-756.196	-748.196	-747.811	-660.817	1.000
2	-462.715	-454.715	-454.118	-369.526	0.950
3	-546.255	-538.255	-537.789	-459.326	0.000
4	-149.936	-141.936	-139.079	-70.802	0.979
5	-151.796	-143.796	-140.938	-70.937	0.005
6	-282.237	-274.237	-273.060	-195.469	0.001
Subset	CTRW				
	NLL (19)	AIC (20)	AIC_c (21)	KIC (22)	Posterior prob. (23)
1	-460.696	-456.696	-456.583	-425.746	0.000
2	-413.792	-409.792	-409.618	-371.524	0.000
3	-568.758	-564.758	-564.622	-517.224	1.000
4	-117.316	-113.316	-112.566	-94.097	0.000
5	-93.840	-89.840	-89.090	-65.580	0.000
6	-186.613	-182.613	-182.28	-151.501	0.000

Table 5.6. Results from model calibration and identification criteria (**6a.** ADE; **6b.** DP; **6c.** CTRW).

It is interesting to observe that the identification criteria *AIC* (5.14) and AIC_c (5.15) render almost identical values, and very close to *NLL* (5.13), for all of the scenarios tested. This implies that the contribution of

NLL dominates over the influence of the number of parameters associated with the selected models in the calculation of these model selection criteria. Note that the lowest value of a given model identification criterion indicates the most favored model (according to the criterion itself) at the expense of the remaining models. The identification criterion *KIC* (5.16) is generally in line with the results of the remaining criteria, with the exception of subset 4, for which CTRW is favored over DP. Note that *KIC* values differ from *NLL* (5.13) as *KIC* also contains the expected information content through the parameter covariance matrix.

The predictive capability of the selected models is then explored by comparison of calibrated model outputs against concentrations values and profiles which were not employed during the calibration step. For the purpose of illustration, the calibration values of parameters resulting from subsets 2 and 5 are considered in the following.

Figure 5.5 (first row) depicts the comparison between the four measured concentration profiles and the modeling results obtained through the ADE when the parameters are calibrated on the basis of the most sensitive observations taken at the second and third concentration profiles (i.e., subset 5). The insert in each figure is a scatterplot of the model results versus measurements. Figure 5.5 (second row) presents corresponding results based on the ADE when parameter calibration is performed on the basis of the complete set of observations available for the second observation time (subset 2). Figures 5.6 and 5.7 illustrate corresponding results for the DP and CTRW models, respectively. The picture is complemented by Table 5.7, which reports the mean square error (MSE) between data and model predictions calculated for each observation time and model.

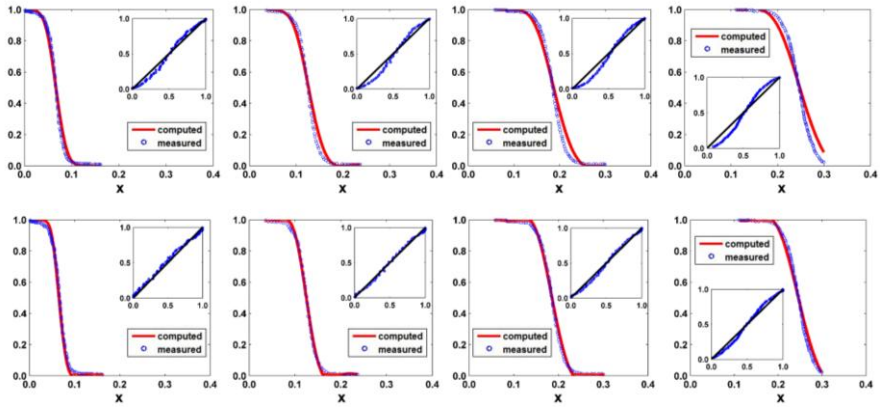

Figure 5.5. Comparison among the four concentration profiles of *Gramling et al.* [2002] and modeling results obtained through the ADE model with parameters calibrated on the basis of (top) the most sensitive observations taken at τ_2 and τ_3, i.e., subset 5 in Table 5.4, or (bottom) the complete set of observations available for τ_2, i.e., subset 2 in Table 5.4.

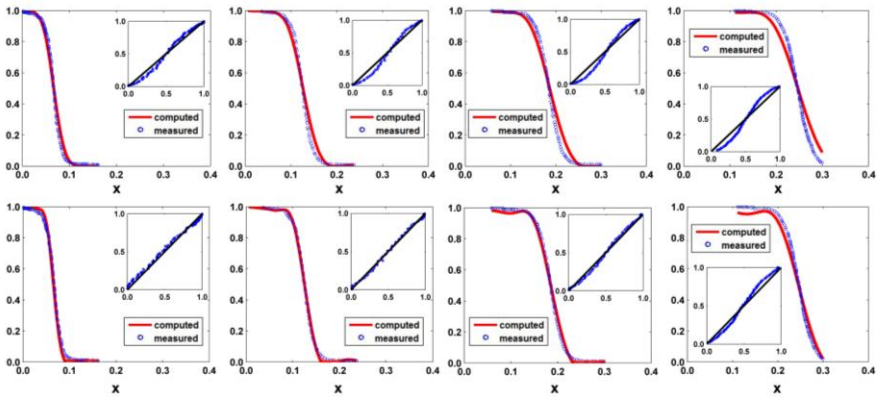

Figure 5.6. Comparison among the four concentration profiles of Gramling et al. [2002] and modeling results obtained through the DP model with parameters calibrated on the basis of (top) the most sensitive observations taken at τ_2 and τ_3, i.e., subset 5 in Table 5.4, or (bottom) the complete set of observations available for τ_2, i.e., subset 2 in Table 5.4.

Analysis of the results reported in the first rows of Figures 5.5, 5.6, and 5.7 reveals that the sensitivity-based calibration of each model returns an acceptable approximation (accurate in the case of the CTRW model) of

all four profiles even though only 20 observations are used out of a total of 380 data points available. It is remarkable to note that the best predictive power, assessed through Figures 5.5-5.7 and Table 5.7, is associated with the CTRW model even as the posterior probability weight associated with the ADE is clearly dominant in this case (Table 5.6).

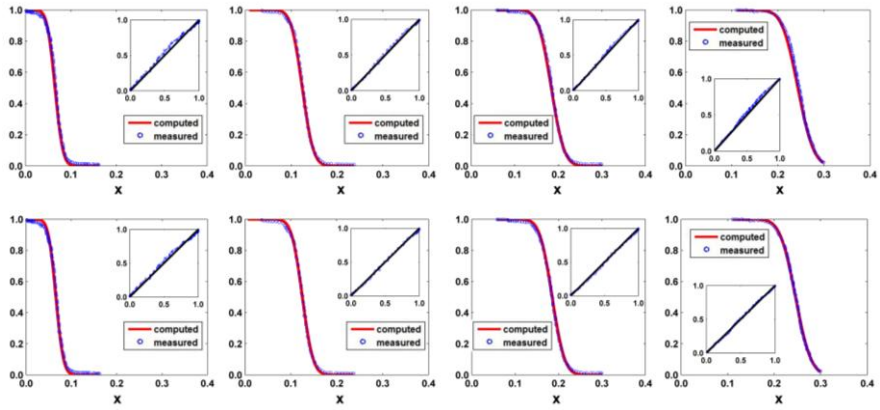

Figure 5.7. Comparison among the four concentration profiles of *Gramling et al.* [2002] and modeling results obtained through the CTRW model with parameters calibrated on the basis of (top) the most sensitive observations taken at τ_2 and τ_3, i.e., subset 5 in Table 5.4, or (bottom) the complete set of observations available for τ_2, i.e., subset 2 in Table 5.4.

With reference to the analysis performed on the basis of the calibration performed on subset 2 (second rows in Figures 5.5, 5.6, and 5.7), the DP model stands out as the best alternative in fitting the observations (Table 5.6) but is not equally adequate to predict the remaining concentration profiles, especially for late time. This appears to be linked to the observed tendency of the mass transfer coefficient to be associated with larger values at early times. The CTRW model, which includes the ADE and the DP model as particular cases, appears to return the best prediction capability also in this case.

Subset		*2*	*5*
ADE: MSE	τ_1	8.87E-04	1.66E-03
	τ_2	4.74E-04	2.60E-03
	τ_3	7.63E-04	3.12E-03
	τ_4	1.61E-03	5.01E-03
DP: MSE	τ_1	9.77E-04	1.81E-03
	τ_2	4.14E-04	2.79E-03
	τ_3	8.82E-04	3.34E-03
	τ_4	2.46E-03	5.38E-03
CTRW: MSE	τ_1	6.30E-04	9.39E-04
	τ_2	2.02E-04	4.19E-04
	τ_3	1.57E-04	2.87E-04
	τ_4	9.34E-05	9.04E-04

Table 5.7. Model validation in terms of mean square error (MSE) for each of the four concentration profiles (corresponding to observation times τ_i, i = 1, 2, 3, 4) and observation subsets 2 and 5 (Table 5.4).

5.6.3 Implications for experiment design

The sensitivity-based methodology presented here has direct implications for the analysis of the interpretive capability of models for a given case study. GSA allows identification of (i) the parameters that may play an important role in model interpretation, thus providing an answer to the question related to which parameters can be estimated; (ii) convenient space-time locations where measurements should be collected to be used during the model calibration step, thus providing an indication about where one should concentrate measuring efforts; and (iii) reduced sets of observations with relevant information content for parameter calibration, thus providing an indication about the amount of data that needs to be collected.

The first key point above highlighted has been shown to be relevant in this case study for, e.g., the CTRW model because GSA reveals a markedly

different degree of influence of the (uncertain) parameters on the model output. Note that the parameters which are less relevant for this model are associated with the worse calibration results, in terms of relative width of confidence intervals (see Table 5.5), suggesting the possibility of excluding these parameters from the analysis of the model interpretive capability for the selected case study. Excluding t_1 and t_2 from model calibration results in a significant improvement in the reduction of the confidence intervals associated with the remaining parameters. This supports the relevant role of the GSA based approach in the parameter identification process.

The second and the third key points evidenced are particularly relevant in light of the need to optimize the number of measurements. This becomes particularly relevant when the analysis is performed in a multi-model context, as done in this work. When a set of multiple models is employed, it becomes relevant to explore the possibility of optimizing the set of measurement points to properly calibrate the parameters associated with each model, given that each model can display large sensitivity to parameters within different space-time intervals. This kind of analysis is exemplified in Figure 5.4, where one can observe that regions with high sensitivity to parameters overlap for the different models, thus guiding in optimizing the experimental effort in terms of number of measurements to be collected.

5.7 FINAL REMARKS

Application of a complete methodology for sensitivity-based parameter calibration applied to transport models in porous media has been illustrated. The potential of the methodology for model-driven experimental design is demonstrated through an application to a

conservative transport experiment [*Gramling et al.*, 2002]. The methodology is articulated according to the following steps: (i) selection of one or more competing interpretive models for the transport problem considered; (ii) identification of space-time locations which are most influenced by the uncertainty in model input parameters via a complete GSA performed through the PCE method; (iii) calibration of model parameter within a Maximum Likelihood context, considering subsets of measurements associated with the space-time locations which are most sensitive to model parameters; (iv) ranking of selected models by means of model quality criteria and estimating the relative degree of likelihood of each model by means of a weight, or posterior probability; and (v) model validation with the available observations which are not employed in the calibration step.

As shown this GSA-based approach allows identification of (i) the relative importance of model-dependent parameters, and (ii) the observations carrying the largest information content for parameter calibration and model identification purposes. The investigation on the interpretive capability of three selected conservative transport models (i.e., ADE, DP model and CTRW) through the methodological framework illustrated leads to the following key results and conclusions:

1. Results from the ADE model are most sensitive to velocity at locations close to the solute center of mass, while sensitivity to dispersivity is largest close to the tails of the concentration distribution. The role of the mass transfer coefficient in the DP model is less significant at the advancing solute front than at the upstream tail of the concentration profiles. Dispersivity is the most important parameter in the DP model for earlier times, its effect decreasing with time. While both the ADE and DP models are sensitive to all parameters, albeit with various

degrees and at different locations, for the transport experiment considered, the CTRW model is sensitive chiefly to β, characterizing the nature of the dispersive transport; the role of D_{ψ} is of some importance only for the observations available at earliest times.

2. Posterior model weights indicate that one model always has a markedly high degree of likelihood, at the expense of the remaining two models, depending on the set of observations considered. Model ranking is highly dependent on the subset of observations considered. The DP model renders the best approximation for the early-time observation subsets, while the ADE is preferable when the GSA-based observation sets are considered. The CTRW model is not excessively penalized in the ranking based on the adopted identification criteria despite its larger number of parameters.
3. The best predictive power, assessed through the validation results presented in Figures 5.4-5.6 and Table 5.7, is always associated with the CTRW model, even in the cases where the posterior probability weight associated with either the ADE or the DP model is clearly dominant. The GSA-based calibration of each model returns an acceptable approximation (remarkably accurate in the case of the CTRW model) of all available concentration profiles even as calibration is performed using minimum sets of observations corresponding to the most sensitive (space-time) locations.

Conclusions

The focus of the present work consists in developing a comprehensive solution for the characterization of the uncertainty associated with model responses in environmental and civil engineering scenarios. With this purpose, a numerical tool based on the Polynomial Chaos Expansion theory has been developed and tested. Several novel applications to flow and transport problems in porous media have been proposed at the laboratory and field scale. Each application showed the potential of the methodology towards expanding the ranges of research in this field at an acceptable computational cost. Others applicative contexts are being explored, such as risk-based or performance-based design (coastal groundwater management, shallow geothermics, water distribution networks), with the dual aim of optimizing the use of natural and water resources and preserving them in the long term.

References

Abramowitz M, Stegun IA (1970) Handbook of mathematical functions. Dover Publications, New York.

Akaike H (1974) A new look at statistical model identification. *IEEET Automatic. Control AC,* 19:716-723.

Al-Attar HH (2011) Evaluation of oil foam as a displacing phase to improve oil recovery: A laboratory study. *Journal of Petroleum Science and Engineering*, 79(3-4):101–112.

Archer GEB, Saltelli A, Sobol IM (1997) Sensitivity measures, ANOVA like techniques and the use of bootstrap. *Journal of Statistical Computation and Simulation*, 58:99-120.

Bai M, Bouhroum A, Civan F, Roegiers JC (1995) Improved model for solute transport in heterogeneous porous media. *Journal of Petroleum Science and Engineering*, 14:66-78.

Ballio F, Guadagnini A (2004) Convergence assessment of numerical Monte Carlo simulations in groundwater hydrology. *Water Resources Research*, 40, W04603.

Bedford T, Cooke R (2001) Probabilistic Risk Analysis: Foundations and Methods. UK: Cambridge University Press.

Berkowitz B, Cortis A, Dentz M, Scher H (2006) Modeling non-Fickian transport in geological formations as a continuous time random walk. *Reviews of Geophysics*, 44, RG2003.

Berkowitz B, Scher H (2009) Exploring the nature of non-Fickian transport in laboratory experiments. *Advances in Water Resources*, 32:750–755.

Bianchi Janetti E, Dror I, Riva M, Guadagnini A, Berkowitz B (2012) Estimation of Single-Metal and Competitive Sorption Isotherms through Maximum Likelihood and Model Quality Criteria. *Soil Science Society of America Journal*, 76:1229-1245.

Blatman G, Sudret B (2010) An adaptive algorithm to build up sparse polynomial chaos expansion for stochastic finite element analysis. *Probabilistic Engineering Mechanics*, 25:183–197.

Butler J (1988) Pumping tests in nonuniform aquifers - The radially symmetric case. *Journal of Hydrology*, 101:15-30.

Cadini F, De Sanctis J, Cherubini A, Zio E, Riva M, Guadagnini A (2012) An integrated simulation framework for the performance assessment of radioactive waste repositories. *Annals of Nuclear Energy* 39:1-8.

Cameron RH, Martin WT (1947) The orthogonal development of non-linear functionals in series of Fourier-Hermite functionals. *Annals of Mathematics*, 48(2):385–392.

Carnevale C, Finzi G, Guariso G, Pisoni E, Volta M (2012) Surrogate models to compute optimal air quality planning policies at a regional scale. *Environmental Modelling & Software*, 34:44-50.

Carrera J, Neuman SP (1986) Estimation of aquifer parameters under transient and steady state conditions: 1. Maximum Likelihood Method Incorporating Prior Information. *Water Resources Research*, 22(2): 199-210.

Castaings W, Borgonovo E, Morris MD, Tarantola S (2012) Sampling strategies in density-based sensitivity analysis. *Environmental Modelling & Software*, 38:13-26.

Chabra RP, Comiti J, Machač I (2001) Flow of non-Newtonian fluids in fixed and fluidised beds. *Chemical Engineering Science*, 56:1-27.

Chen Z, Liu C (1991) Self-similar solutions for displacement of non-Newtonian fluids through porous media. *Transport in Porous Media*, 6(1):13–33.

Cheng H, Sandu A (2009) Uncertainty quantification and apportionment in air quality models using polynomial chaos method. *Environmental Modelling & Software*, 24:917:925.

Ciriello V, Di Federico V (2012) Similarity solutions for flow of non-Newtonian fluids in porous media revisited under parameter uncertainty. *Advances in Water Resources*, 43:38-51.

Ciriello V, Di Federico V, Riva M, Cadini F, De Sanctis J, Zio E, Guadagnini A (2012) Polynomial Chaos Expansion for Global Sensitivity Analysis applied to a model of radionuclide migration in a randomly heterogeneous aquifer. *Stochastic Environmental Research and Risk Assessment*, DOI: 10.1007/s00477-012-0616-7.

Ciriello V, Di Federico V (2013) Analysis of a benchmark solution for non-Newtonian radial displacement in porous media. *International Journal of Non-Linear Mechancis*, 52:46-57.

Ciriello V, Guadagnini A, Di Federico V, Edery Y, Berkowitz B (2013) Comparative analysis of formulations for conservative transport in porous media through sensitivity-based parameter calibration. *Water Resources Research* (Under Review)

Comba S, Dalmazzo D, Santagata E, Sethi R (2011) Rheological characterization of xanthan suspensions of nanoscale iron for injection in porous media. *Journal of Hazardous Materials*, 185:598–605.

Cortis A, Berkowitz B (2005) Computing "anomalous" contaminant transport in porous media: the CTRW Matlab toolbox. *Ground Water*, 43(6), 947-950.

Cristopher RH, Middleman S (1965) Power-law flow through a packed tube. *Industrial & Engineering Chemistry Fundamentals*, 4(4):422-426.

CTRW Matlab Toolbox,
http://www.weizmann.ac.il/ESER/People/Brian/CTRW

Dagan G (1989) Flow and transport in porous formations. Springer-Verlag, Heidelberg.

de Barros FPJ, Bolster D, Sanchez-Vila X, Nowak W (2011) A divide and conquer approach to cope with uncertainty, human health risk, and decision making in contaminant hydrology. *Water Resources Research*, 47 W05508.

Dentz M, Cortis A, Scher H, Berkowitz B (2004) Time behavior of solute transport in heterogeneous media: transition from anomalous to normal transport. *Advances in Water Resources*, 27:155-173.

Di Federico V, Ciriello V (2012) Generalized solution for 1-D non-Newtonian flow in a porous domain due to an instantaneous mass injection. *Transport in Porous Media*, 93(1):63-77.

Di Federico V, Pinelli M, Ugarelli R (2010) Estimates of effective permeability for non-Newtonian fluid flow in randomly heterogeneous porous media. *Stochastic Environmental Research and Risk Assessment*, 24(7):1067-1076.

Doherty J (2002) PEST: Model independent parameter estimation, user manual. 4th ed. Watermark Numer. Computing, Corinda, Queensland.

ENEA (1997) Internal Report. Chapman, N. A.

ENEA (2000) Inventario nazionale dei rifiuti radioattivi - Task Force per il sito nazionale di deposito dei materiali radioattivi. 3rd Ed (in Italian).

EC (2003) Common Implementation Strategy for the Water Framework Directive (2000/60/EC). Guidance Document No. 11. Planning Processes. Working Group 2.9. Office for the Official Publications of the European Communities, Luxembourg.

Fajraoui N, Ramasomanana F, Younes A, Mara TA, Ackerer P, Guadagnini A (2011) Use of global sensitivity analysis and polynomial chaos expansion for interpretation of nonreactive transport experiments in laboratory-scale porous media. *Water Resources Research*, 47, W02521.

Fajraoui N, Mara TA, Younes A, Bouhlila R (2012) Reactive transport parameter estimation and global sensitivity analysis using sparse polynomial chaos expansion. *Water, Air & Soil Pollution*, 223(7):4183-4197.

Fiori A, Berglund S, Cvetkovic V, Dagan G (2002) A first-order analysis of solute flux statistics in aquifers: the combined effect of pore-scale dispersion, sampling, and linear sorption kinetics. *Water Resources Research*, 38(8).

Fokker PA, Verga F (2011) Application of harmonic pulse testing to water–oil displacement. *Journal of Petroleum Science and Engineering*, 79:125–134.

Ghanem R (1998) Probabilistic characterization of transport in heterogeneous media. *Computers Methods in Applied Mechanics and Engineering*, 158:199-220.

Ghanem RG, Spanos PD (1991) Stochastic finite elements-a spectral approach. Springer, Berlin.

Gómez-Hernández JJ, Journel AG (1993) Joint sequential simulation of multi-Gaussian field. Geostatitics Troia '92, 1:85-94. Ed Soares.

Gradshteyn IS, Ryzhik IM (2000) Table of Integrals, Series and Products. Academic Press, New York.

Gramling CM, Harvey CF, Meigs LC (2002), Reactive transport in porous media: a comparison of model prediction with laboratory visualization. *Environmental Science & Technology*, 36:2508-2514.

Guadagnini A, Neuman SP (2001) Recursive conditional moment equations for advective transport in randomly heterogeneous velocity fields. *Transport in Porous Media*, 42:37-67.

Huang H, Hassan AE, Hu BX (2003) Monte Carlo study of conservative transport in heterogeneous dual-porosity media. *Journal of Hydrology*, 275: 229-241.

Huang S, Sankaran M, Ramesh R (2007) Collocation-based stochastic finite element analysis for random field problems. *Probabilistic Engineering Mechanics*, 22:194-205.

Hung YT, Butler E, Kuo CY, Yeh RYL (2010) Chemicals and allied products. *Water Environment Research*, 82(10):1448-1467.

Hurvich CM, Tsai CL (1989) Regression and time series model selection in small sample. *Biometrika*, 76(2):297-307.

Kashyap RL (1982) Optimal choice of AR and MA parts in autoregressive moving average models. *IEEET Pattern Anal.*, 4(2):99-104.

Kim MC, Cho CK (2011) Linear analysis on the stability of miscible dispersion of shear-thinning fluids in porous media. *Journal of Non-Newtonian Fluid Mechanics*, 166:1211–1220.

Lewis G (2011) Viscoelastic properties of injectable bone cements for orthopaedic applications: State-of-the-art review. *Journal of Biomedical Materials Research Part B: Applied Biomaterials*, 98B(1):171-191.

Li D, Chen Y, Lu W, Zhou C (2011) Stochastic response surface method for reliability analysis of rock scope involving correlated non-normal variables. *Computer and Geotechnics*, 38:58-68.

Li Yan Y, Deng Q, He F, Zhang X-Q, Liu YP (2011) Remediation of DNAPL-contaminated aquifers using density modification method with colloidal liquid aphrons. *Colloids and Surfaces A: Physicochemical and Engineering Aspects*, 385:219-228.

Marseguerra M, Patelli E, Zio E (2001) Groundwater contaminant transport in presence of colloids I. A stochastic nonlinear model and parameter identification. *Annals of Nuclear Energy*, 28:777-803.

Marseguerra M, Patelli E, Zio E (2001) Groundwater contaminant transport in presence of colloids II. Sensitivity and uncertainty analysis on literature case studies. *Annals of Nuclear Energy*, 28:1799-1807.

Marseguerra M, Zio E (2001) Genetic algorithms for estimating effective parameters in a lumped reactor model for reactivity predictions. *Nuclear Science and Engineering*, 139:96-104.

Marseguerra M, Zio E, Patelli E, Giacobbo F, Ventura G, Mingrone G (2003) Monte Carlo simulation of contaminant release from a radioactive waste deposit. *Mathematics and Computers in Simulation*, 62:421-430.

McDonald MG, Harbaugh AW (1988) A Modular Three-Dimensional Finite-Difference Groundwater Flow Model. Man. 83-875, U.S. Geol. Surv. Reston, VA.

Morales-Casique E, Neuman SP, Guadagnini A (2006) Nonlocal and localized analyses of nonreactive solute transport in bounded randomly heterogeneous porous media: Computational analysis. *Advances in Water Resources*, 29:1399-1418.

Nair RN, Krishnamoorthy TM (1999) Probabilistic safety assessment model for near surface radioactive waste disposal facilities. *Environmental Modelling & Software* 14:447–460.

Nataf A (1962) Détermination des distributions dont les marges sont données. C R *Acad Sci*, 225:42-3.

Neuman SP (1990) Universal scaling of hydraulic conductivities and dispersivities in geologic media. *Water Resources Research*, 26(8): 1749-1758.

Neuman SP (2003) Maximum likelihood Bayesian averaging of alternative conceptual-mathematical models. *Stochastic Environmental Research and Risk Assessment*, 17(5), 291-305.

Neuman SP, Blattstein A, Riva M, Tartakovsky DM, Guadagnini A, Ptak T (2007) Type curve interpretation of late-time pumping test data in randomly heterogeneous aquifers. *Water Resources Research*, 43, W10421.

Neuman SP, Di Federico V (2003) Multifaceted nature of hydrogeologic scaling and its interpretation. *Reviews of Geophysics*, 41(3):1014.

Neuman SP, Xue L, Ye M, Lu D (2011) Bayesian analysis of data-worth considering model and parameter uncertainty, *Advances in Water Resources*, doi: 10.1016/j.advwatres.2011.02.007.

Nield DA, Bejan A (2006) Convection in Porous Media. 3rd ed., Springer, New York.

Oladyshkin S, de Barros FPJ, Nowak W (2012) Global sensitivity analysis: a flexible and efficient framework with an example from stochastic hydrogeology. *Advances in Water Resources*, 37:10-22.

Pascal H (1983) Nonsteady flow of non-Newtonian fluids through porous media. *International Journal of Engineering Science*, 21(3):199.

Pascal H (1984a) Rheological behaviour effect of non-Newtonian fluids on dynamic of moving interface in porous media. *International Journal of Engineering Science*, 22(3):227-241.

Pascal H (1984b) Dynamic of moving interface in porous media for power law fluids with yield stress. *International Journal of Engineering Science*, 22(5):577-591.

Pascal H (1986) Rheological effects of non-Newtonian behaviour of displacing fluids on stability of a moving interface in radial oil

displacement mechanism in porous media. *International Journal of Engineering Science*, 24(9):1465-1476.

Pascal H (1988) Stability of non-Newtonian fluid interfaces in a porous medium and its applications in an oil displacement mechanism. *Journal of Colloid and Interface Science*, 123(1):14-23.

Pascal H (1990) Some self-similar two-phase flows of non-Newtonian fluids through a porous media. *Studies in Applied Mathematics*,82:305-318.

Pascal H (1991) On propagation of pressure disturbances in a non-Newtonian fluid flowing through a porous medium. *International Journal of Non-Linear Mechanics*, 26(5):475-485.

Pascal H (1992) Similarity solutions to some two-phase flows through porous media. *International Journal of Non-Linear Mechanics*, 27(4):565-563.

Pascal H, Pascal F (1985) Flow of non-Newtonian fluid through porous media. *International Journal of Engineering Science*, 23(5):571-585.

Pascal H, Pascal F (1988) Displacement of non-Newtonian fluid interfaces in a porous medium: compressible fluid. *Journal of Non-Newtonian Fluid Mechanics*, 28:227-238.

Pedersen KS, Ronningsen HP (2000) Effect of Precipitated Wax on Viscosity - A Model for Predicting Non-Newtonian Viscosity of Crude Oils. *Energy&Fuels*, 14(1):43-51.

Phoon KK, Huang SP, Quek ST (2002) Implementation of Karhunen–Loeve expansion for simulation using a wavelet-Galerkin scheme. *Probabilistic Engineering Mechanics*, 17:293:303.

Porta G, Riva M, Guadagnini A (2012) Upscaling solute transport in porous media in the presence of an irreversible bimolecular reaction. *Advances in Water Resources*, 35:151-162.

Refsgaard JC, van der Sluijs JP, Lajer Højberg A, Vanrolleghem PA (2007) Uncertainty in the environmental modelling process e A framework and guidance. *Environmental Modelling & Software*, 22:1543-1556.

Rubin Y (2003) Applied Stochastic Hydrogeology. Oxford Univ. Press, New York.

Rubin Y, Sun A, Maxwell R, Bellin A (1999) The concept of block-effective macrodispersivity and a unified approach for grid-scale- and plume-scale-dependent transport. *Journal of Fluid Mechanics*, 395: 161-180.

Ruyer-Quil C, Chakraborty S, Dandapat BS (2012) Wavy regime of a power-law film flow. *Journal of Fluid Mechanics*, 692:220-256.

Saltelli A, Tarantola S, Campolongo F (2000) Sensitivity analysis as an Ingredient of Modeling. *Statistical Science*, 15(4):377-395.

Shi L, Zhang D, Lin L, Yang J (2010) A multiscale probabilistic collocation method for subsurface flow in heterogeneous media. *Water Resources Research*, 46, W11562.

Sobol IM (1993) Sensitivity estimates for nonlinear mathematical models. *Math Modeling Comput* 1:407-414.

Sobol IM (2001) Global sensitivity indices for nonlinear mathematical models and their Monte Carlo estimates. *Mathematics and Computers in Simulation*, 55:271-280.

Soize C, Ghanem R (2004) Physical systems with random uncertainties: Chaos representations with arbitrary probability measures. *Journal of Scientific Computing*, 26(2):395-410.

Spanos PD, Ghanem R (1989) Stochastic finite element expansion for random media. *Journal of Engineering Mechanics* ASCE, 115(5):1035-1053.

Stehfest H (1970) Numerical inversion of Laplace transforms. *Commun. A.C.M. 13*(1), 47-49.

Sudret B (2008) Global sensitivity analysis using polynomial chaos expansions. *Reliability Engineering & System Safety*, 93:964-979.

Tartakovsky DM (2007) Probabilistic risk analysis in subsurface hydrology. *Geophysics Research Letters*, 34.

Tartakovsky DM (2012) Assessment and management of risk in subsurface hydrology: A review and perspective. *Advances in Water Resources*, 51:247-260.

Tsakiroglou CD (2004) Correlation of the two-phase flow coefficients of porous media with the rheology of shear-thinning fluids. *Journal of Non-Newtonian Fluid Mechanics*, 117(1):1-23.

US National Research Council (1997) Review of Recommendations for Probabilistic Seismic Hazard Analysis: Guidance on Uncertainty and Use of Experts, Natl. Academy Press, Washington, DC.

Volkova E, Iooss B, Van Dorpe F (2008) Global sensitivity analysis for a numerical model of radionuclide migration from the RRC "Kurchatov Institute" radwaste disposal site. *Stochastic Environmental Research and Risk Assessment*, 22:17-31.

Webster M, Tatang MA, McRae GJ (1996) Application of the probabilistic collocation method for an uncertainty analysis of a simple ocean model. *Technical report, MIT* joint program on the science and policy of global change reports series no. 4, Massachusetts Institute of Technology.

Wiener N (1938) The homogeneous chaos. *Am J Math* 60:897-936.

Winter CL (2010) Normalized Mahalanobis distance for comparing process-based stochastic models. *Stochastic Environmental Research and Risk Assessment*, 24:917–923.

Winter CL, Tartakovsky DM (2002) Groundwater flow in heterogeneous composite aquifers. *Water Resources Research*, 38(8):1148.

Winter CL, Tartakovsky DM (2008) A reduced complexity model for probabilistic risk assessment of groundwater contamination. *Water Resources Research*, 44, W06501.

Wu YS, Pruess K, Witherspoon PA (1991) Displacement of a Newtonian fluid by a non-Newtonian fluid in a porous medium. *Transport in Porous Media*, 6(2):115-142.

Wu YS, Pruess K (1996) Flow of non-Newtonian fluids in porous media. *Advances in Porous Media*, 3:87-184.

Wu YS, Pruess K (1998) A numerical method for simulating non-Newtonian fluid flow and displacement in porous media. *Advances in Water Resources*, 21:351-362.

Xiu D, Karniadakis GE (2002) The Wiener-Askey polynomial chaos for stochastic differential equations. *Journal of Scientific Computing*, 24(2):619-644.

Ye M, Meyer PD, Neuman SP (2008) On model selection criteria in multimodel analysis. *Water Resources Research*, 44, W03428.

Ye M, Neuman SP, Meyer PD (2004) Maximum likelihood Bayesian averaging of spatial variability models in unsaturated fractured tuff. *Water Resources Research*, 40(5), W05113.

Zhang D (2002) Stochastic methods for flow in porous media: copying with uncertainties. Academic Press, San Diego.

Zhang D, Neuman SP (1996) Effect of local dispersion on solute transport in randomly heterogeneous media. *Water Resources Research*, 32(9):2715–2723.

Zhang D, Shi L, Chang H, Yang J (2010) A comparative study of numerical approaches to risk assessment of contaminant transport. *Stochastic Environmental Research and Risk Assessment*, 24:971-984.

Zhou Q, Birkholzer JT, Tsang CF, Rutqvist J (2008) A method for quick assessment of CO2 storage capacity in closed and semi-closed saline formations. *International Journal of Greenhouse Gas Control*, 2:626–639.

Zhu ZH, Wu Q, Gao C, Du X (2002) Numerical simulation of two-dimensional transient water driven non-Newtonian fluid flow in porous media. *Communications in Numerical Methods in Engineering*, 18:229–240.

Zuloaga P (2006) New Developments in LLW Management in Spain. ENRESA. <http://www.euronuclear.org/events/topseal/presentations/PP-Session-IIIZuloaga.pdf>.

Ringraziamenti

Ringrazio sentitamente il mio supervisore, Prof. Vittorio Di Federico, per l'impegno ed i preziosi scambi quotidiani che mi ha dedicato e per la stima e la fiducia che mi hanno permesso di crescere e di creare un mio percorso autonomo di responsabilità e passione nei confronti della ricerca.

Alla stessa maniera ringrazio il Prof. Alberto Guadagnini che, anche a distanza, è stato capace di seguirmi costantemente con impegno ed interesse, attraverso confronti stimolanti che hanno saputo indirizzare ed incentivare le mie propensioni.

Il lavoro svolto assieme mi ha reso assolutamente soddisfatta del mio percorso di Dottorato, sia in termini di risultati che di conoscenze acquisite che hanno combaciato con interessi ed aspirazioni.

Un ringraziamento va quindi a tutte le persone con cui ho lavorato e sviluppato i temi di ricerca raccolti in questa tesi, a partire dalla Prof.ssa Monica Riva e dal gruppo del Dipartimento di Energia del Politecnico di Milano composto dal Prof. Enrico Zio, dall'Ing. Francesco Cadini e dal Dott. Jacopo De Sanctis. Ringrazio il Prof. Brian Berkowitz ed il collega Ph.D. Yaniv Edery del Weizmann Institute of Science di Israele e il Prof. Xavier Sanchez-Vila della Technical University of Catalonia di Barcellona, che mi ha ospitata nel corso del periodo di ricerca che ho svolto all'estero.

Ringrazio il Prof. Alberto Lamberti per i consigli e l'incoraggiamento ad intraprendere questo percorso e l'Ing. Renata Archetti per la disponibilità dimostrata quotidianamente sia a livello professionale che personale.

Un pensiero va poi a tutti i colleghi di Dottorato, non soltanto di Bologna, con i quali ho condiviso questa avventura.

Infine, il ringraziamento più importante a quelle persone che non ho bisogno di nominare e che sono in grado di aggiungere un valore decisivo ad ogni cosa, anche a quelle per cui nutro già una forte passione quale è la ricerca.